1.3.2.4 Figures and tables

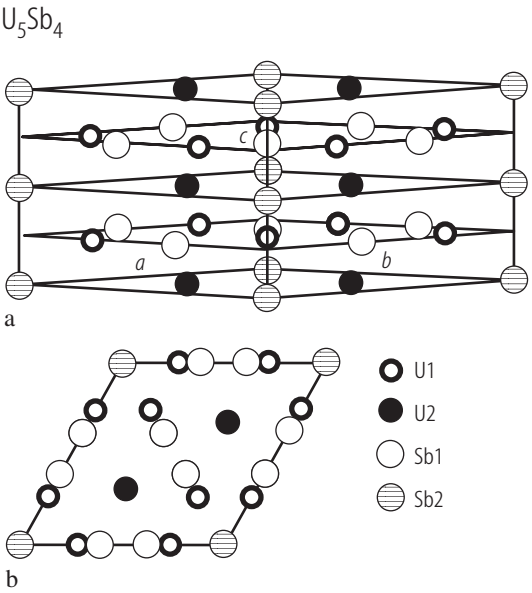

Fig. 1. U_5Sb_4, sc. Crystal structure of the Ti_5Ga_4-type (space group $P6_3mcm$) [94PRBD]. **(a)** Schematic view. **(b)** Projection down the hexagonal *c*-axis. Note two different positions for uranium atoms: U1 ($z = \pm 1/4$) and U2 ($z = 0$, $1/2$). The U2 atoms form chains along the *c*-axis with very short U-U distance of 310 pm.

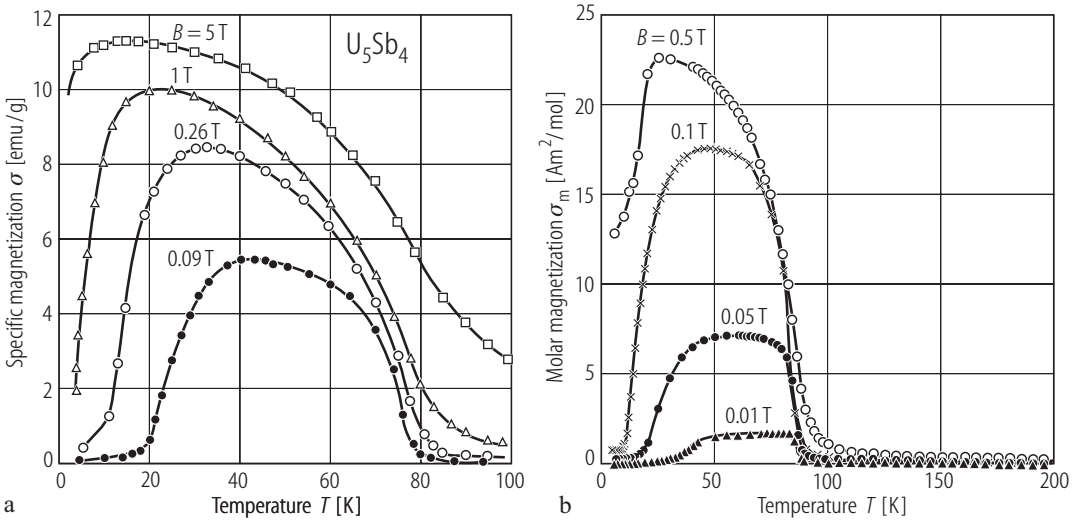

Fig. 2. U_5Sb_4. Magnetization, σ, vs. temperature, T, measured in various magnetic fields upon cooling in zero field: **(a)** a sample with randomly oriented grains [92T]; **(b)** a single-crystalline sample [94PRBD]. The broad maxima in $\sigma(T)$ observed in both studies are characteristic of strongly anisotropic ferromagnets with pronounced narrow-wall domain effects. The Curie temperature is $T_C = 86$ K.

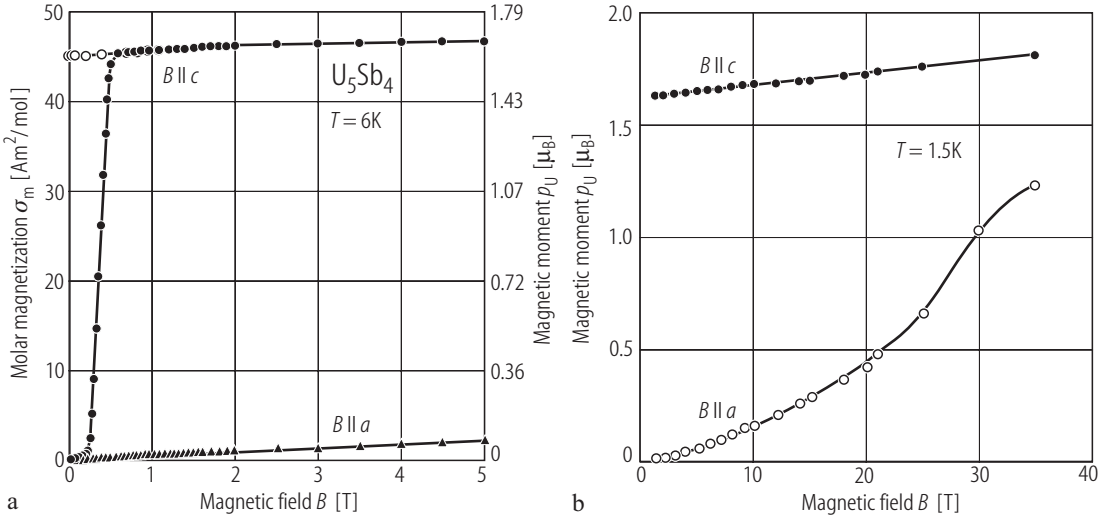

Fig. 3. U_5Sb_4, sc. Magnetization, σ, (magnetic moment p_U) vs. magnetic field, B, measured along the c-axis and a-axis [94PRBD]. **(a)** T = 6 K and $B \leq$ 5 T; **(b)** T = 1.5 K and $B \leq$ 35 T. The compound is a strongly anisotropic ferromagnet with the easy magnetization direction along the c-axis. Note a pronounced remanence and an almost rectangular hysteresis loop. The uranium saturation magnetic moment p_s is about 1.7 μ_B. In panel **(b)** note a metamagnetic-like transition at 25 T occurring in $\sigma(B)$ taken along the hard magnetization a-axis. Compare $\sigma(B)$ in [92T], where the magnetization measured up to 5 T on polycrystalline sample is smaller by a factor of two, supporting a uniaxial magnetic structure.

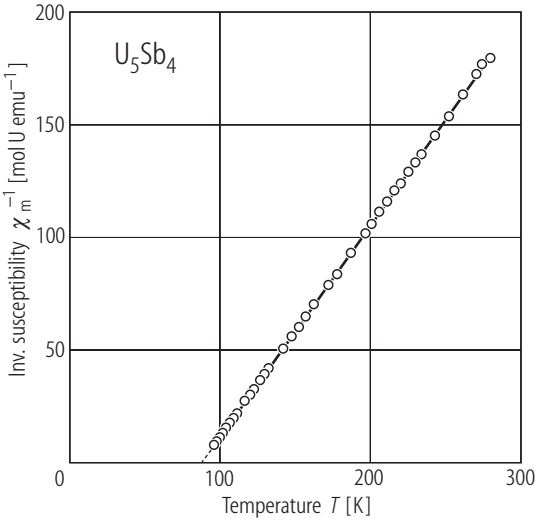

Fig. 4. U_5Sb_4. Inverse molar magnetic susceptibility, χ_m^{-1}, vs. temperature, T [92T]. The solid line is a Curie-Weiss fit with the parameters: p_{eff} = 2.98 μ_B and Θ_p = 86 K. The same parameters were determined in [94PRBD] (see Table F).

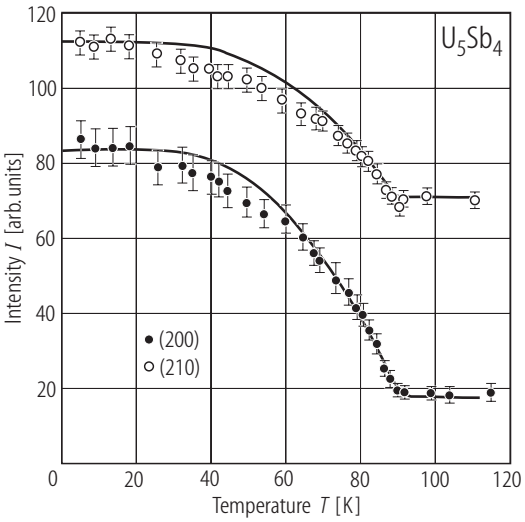

Fig. 5. U_5Sb_4, sc. Total (200) and (210) nuclear and magnetic integrated neutron diffraction intensity, I, vs. temperature, T [94PRBD]. A Brillouin-like temperature variation of both Bragg reflections below T_C = 86 K is observed. At 6 K, the two inequivalent U atoms (see Fig. 1) carry the same magnetic moment of 1.7(1) μ_B oriented along the c-axis.

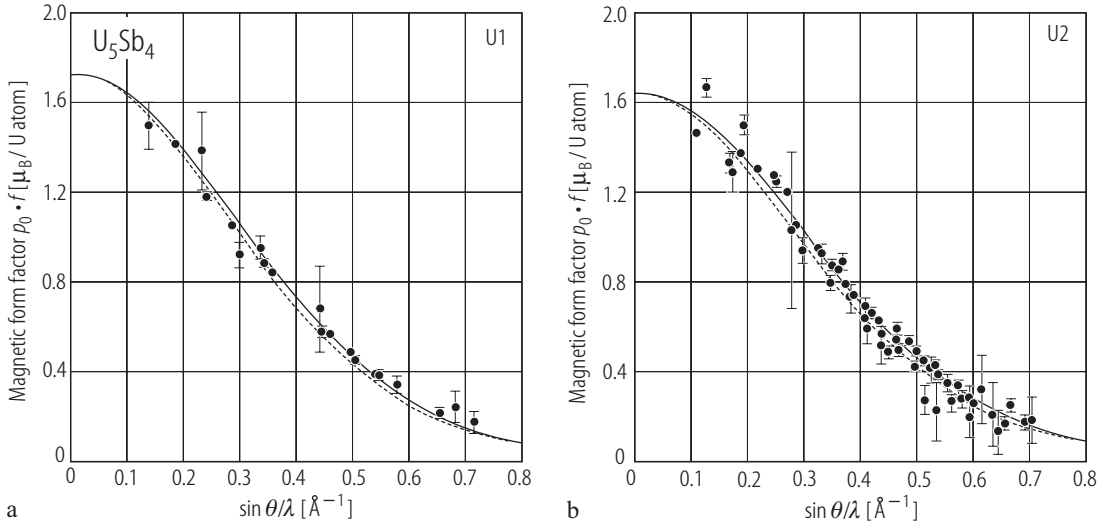

Fig. 6. U_5Sb_4, sc. Magnetic form factor, measured by polarized neutron scattering [94PRBD]. **(a)** U1 atom; **(b)** U2 atom (see Fig. 1). The experimental data were taken at T = 6 K in a magnetic field of 5 T applied along the *c*-axis. The solid lines represent the U^{3+} free ion form factor. The dashed lines are best fits of the experimental results in the dipole approximation. Note that the form factors for both U atoms are close to the prediction for free U^{3+} ion. Some discrepancies, especially at low values of $\sin\theta/\lambda$ presumably result from small negative polarization of 6d electronic states.

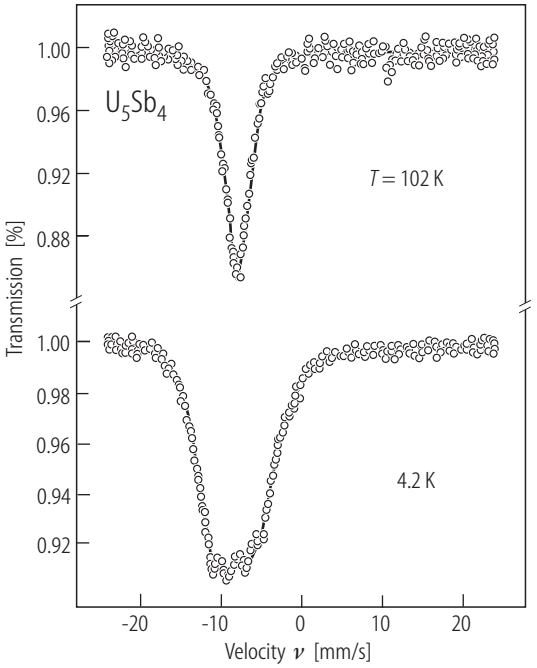

Fig. 7. U_5Sb_4. ^{121}Sb Mössbauer spectra taken at T = 102 and 4.2 K [94PRBD]. The compound orders ferromagnetically at T_C = 86 K. In the paramagnetic state a single absorption line is broadened by quadrupolar interaction, whereas a magnetic splitting of the pattern occurs at low temperature. The lines of the 4.2 K spectrum are poorly resolved because of large natural linewidth of the ^{121}Sb resonance and relatively small hyperfine fields B_{hf} transferred to two distinct Sb atoms. The hyperfine parameters at 4.2 K: δ_{IS} = –7.86(4) mm/s, B_{hf} = 14.7(2) T, e^2qQ = –2.4(6) mm/s, Γ = 2.44(12) mm/s for Sb1 and δ_{IS} = –8.98(16) mm/s, B_{hf} = 14.0(6) T, e^2qQ = –6.5(18) mm/s for Sb2.

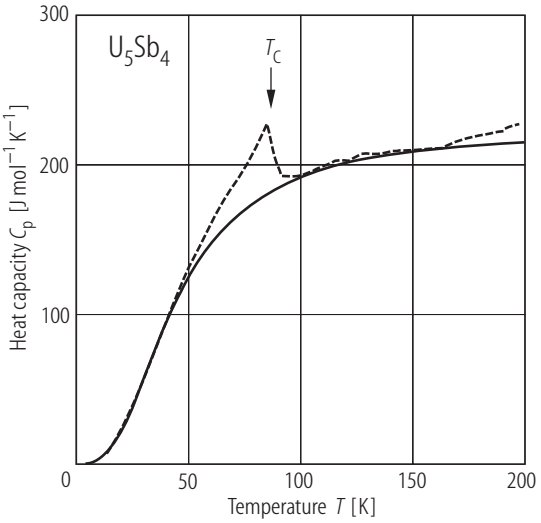

Fig. 8. U_5Sb_4, sc. Heat capacity, C_p, vs. temperature, T, in the range 4.2…200 K [94PRBD]. A sharp λ-shaped peak manifests the ferromagnetic phase transition at T_C = 86 K. The solid line is a fit to the Debye phonon function with Θ_D = 186 K. The magnetic entropy of ordering is 0.5Rln2 per U atom. The electronic specific heat coefficient estimated from the data below 14 K is γ = 37(5) mJ/(mol U)· K^2.

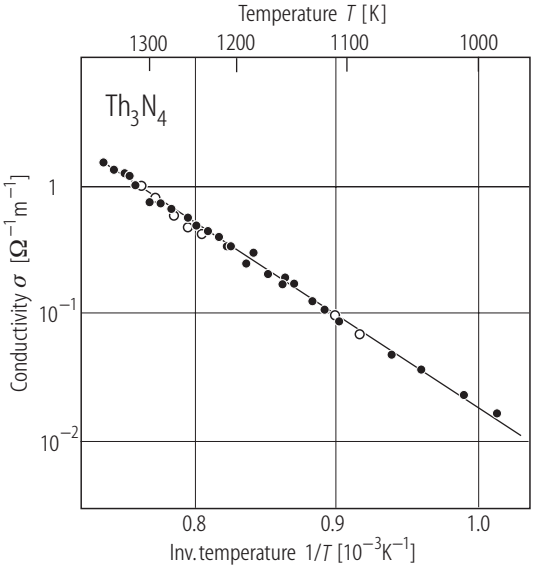

Fig. 10. Th_3N_4. Electrical conductivity, σ, vs. (inverse) temperature, $1/T$, in the range 1000…1353 K [81KTMN]. Open circles: cooling; full circles: heating. The solid straight-line indicates a semiconducting behaviour with an activation energy of 1.40 eV.

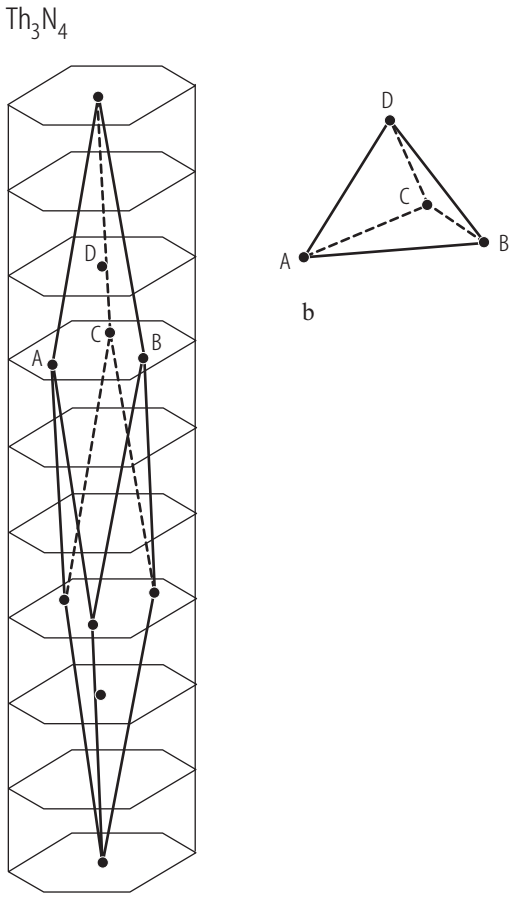

Fig. 9. Th_3N_4. **(a)** Rhombohedral crystal structure of the Al_4C_3-type [66BZ]. Only positions of Th atoms are shown. **(b)** Fragment of the crystal structure [66BZ]. The Th-Th interatomic distances between A, B and C positions are all equal to 385 pm while those between these sites and D position are equal to 375 pm. See also [87UKM].

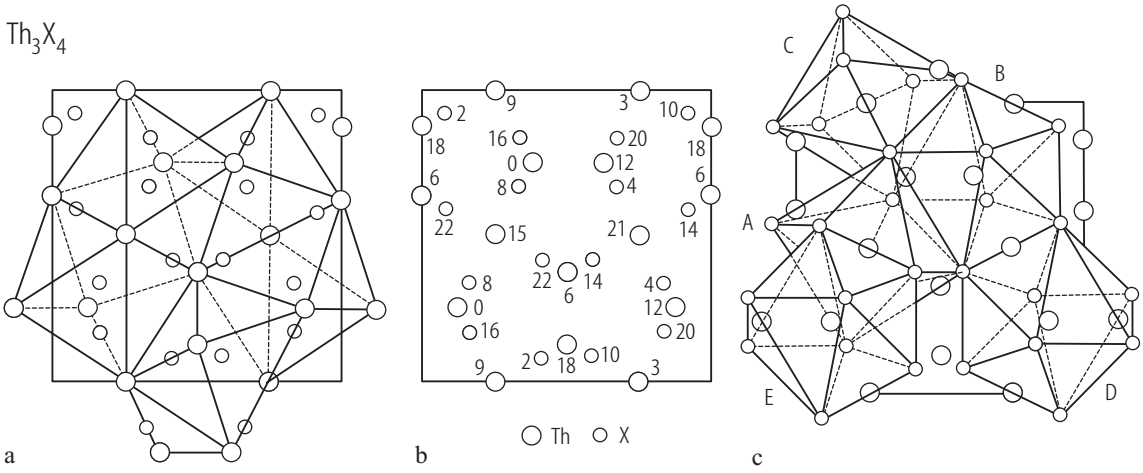

Fig. 11. Th_3X_4, X = P, As, Sb, Bi. Crystal structure projected on the *xy*-plane [63K]. **(a)** Arrangement of distorted [XTh_6] octahedrons. **(b)** Positions of atoms. The numbers denote the *z*-coordinates in 1/24 part of the unit cell side. **(c)** Arrangement of [ThX8] octaverticons.

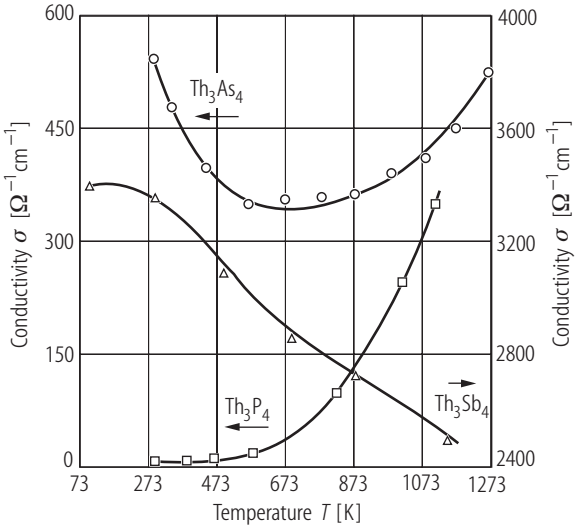

Fig. 12. Th_3X_4, X = P, As, Sb. Electrical conductivity, σ, vs. temperature, *T*, from 80 to ≈1300 K [65PW]. Squares: Th_3P_4; circles: Th_3As_4; triangles: Th_3Sb_4. Note a right-hand side vertical scale for Th_3Sb_4.

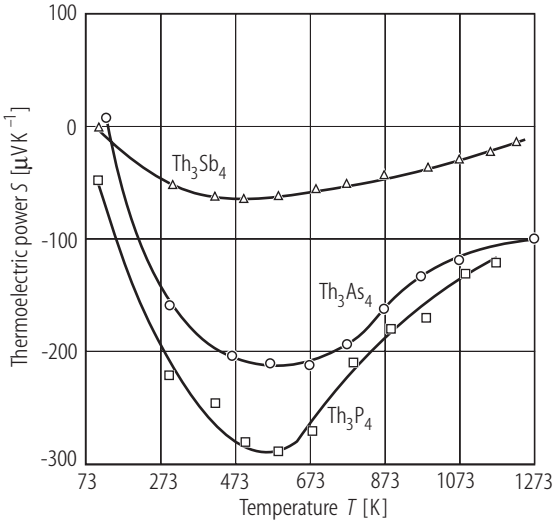

Fig. 13. Th_3X_4, X = P, As, Sb. Thermoelectric power, *S*, vs. temperature, *T*, in the range 80…1300 K [65PW]. Squares: Th_3P_4; circles: Th_3As_4; triangles: Th_3Sb_4.

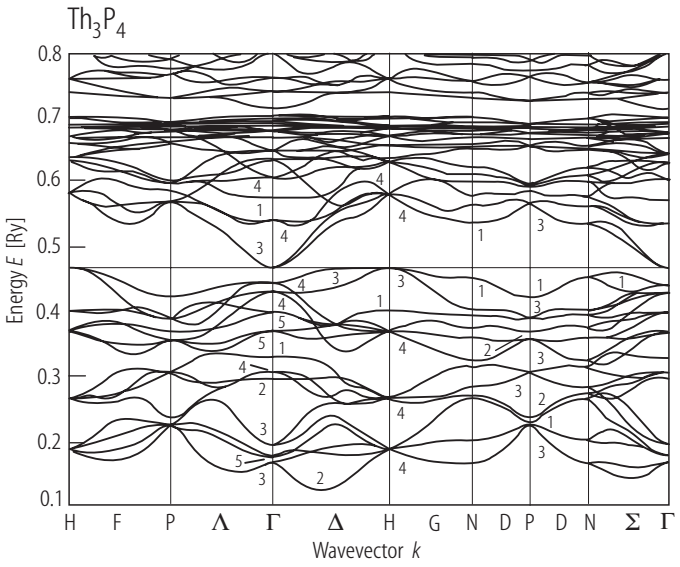

Fig. 14. Th_3P_4. Energy band structure calculated by the self-consistent APW method with the local density approximation [90TKK]. For details on the method used and comprehensive description of the results refer to the original paper. See also Fig. 15.

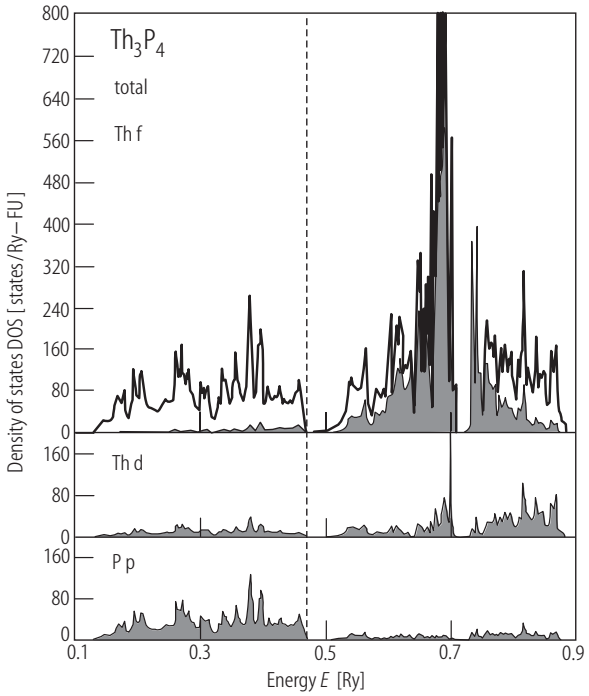

Fig. 15. Th_3P_4. Total and partial DOS calculated by the self-consistent APW method with the local density approximation [90TKK]. The compound is a narrow band semiconductor. The valence band is derived from the P 3p states and the conduction band comes from the Th 6d states. The calculated energy gap of 0.007 eV is however much smaller than the experimental value of 0.29 eV (see Fig. 25), probably because of inadequate treatment of the exchange-correlation potential in LDA. For further details see the original paper.

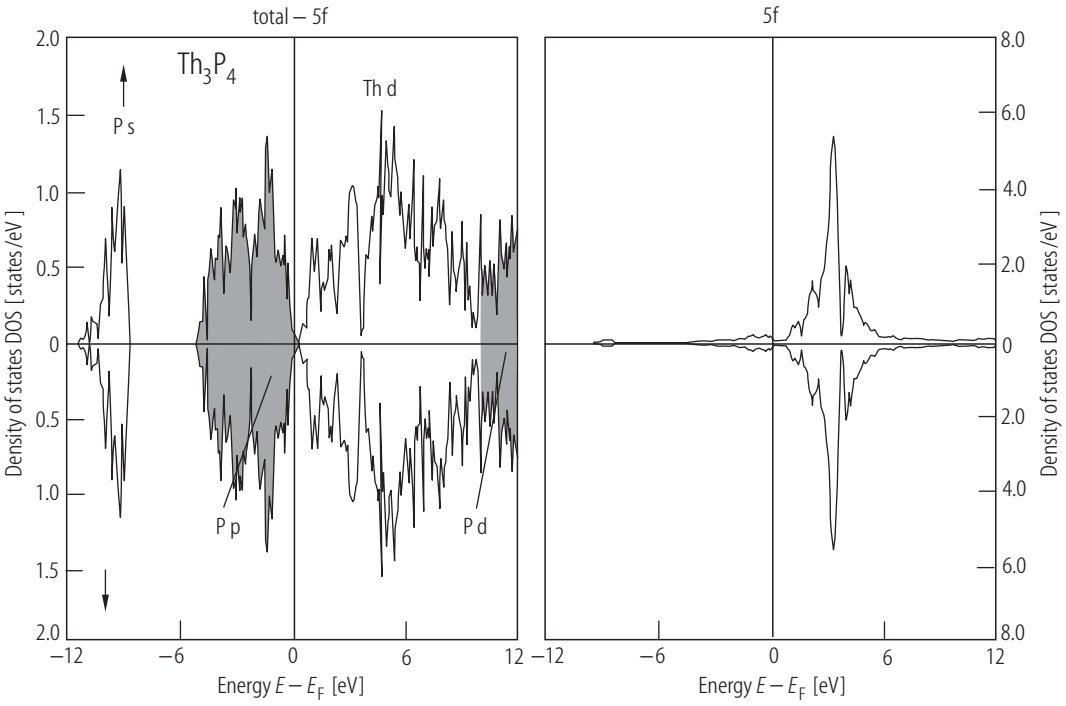

Fig. 16. Th_3P_4. Partial DOS calculated by LDFT using ASW method [98KSK]. Right panel: the spin resolved 5f DOS; left panel: total DOS minus 5f contribution. The shaded states give main contribution to DOS. The spin-up and spin-down DOS are identical, as expected for a nonmagnetic state. There is a pseudogap at E_F, between the P 3p valence band and the Th 6d conduction band. The lack of a real gap of the order of 0.4 eV, as found experimentally (see Fig. 19**)**, is the clear failure of the LDFT approach.

For Fig. 17 see next page

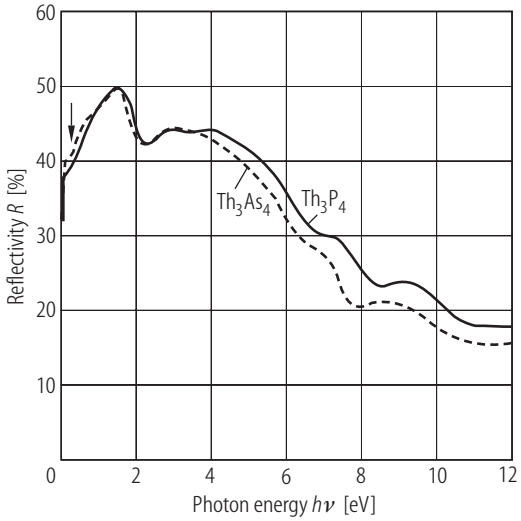

Fig. 18. Th_3X_4, X = P, As, sc. Near normal incidence reflectivity, R, vs. photon energy, $h\nu$, from 0.03 to 12 eV taken at room temperature on polished samples [83SKHH]. Solid curve: Th_3P_4; dashed curve: Th_3As_4. The inflection near 0.3 eV (see the arrow) indicates that both compounds are small gap semiconductors. The steep drop in $R(h\nu)$ below 0.1 eV is due to the presence of a longitudinal optical phonon.

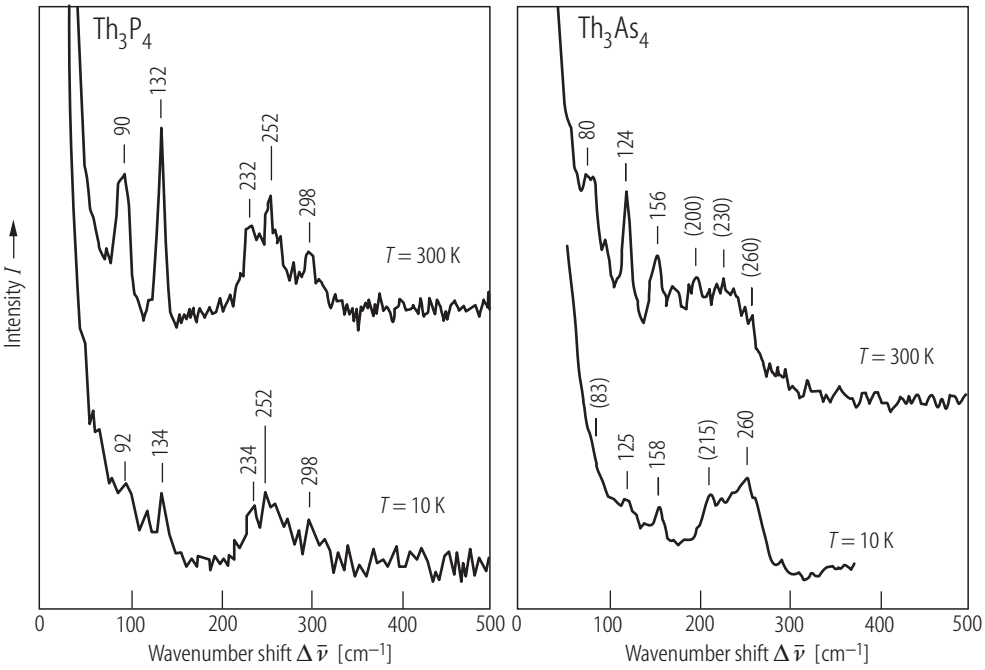

Fig. 17. Th_3X_4, X = P, As, sc. Raman spectra taken at T = 10 and 300 K [83MSKH]. The energies (wavenumbers in cm^{-1}) of characteristic features are given above each spectrum. For the Th_3P_4-type structure one expects five infrared active ($5F_2$) and nine Raman active (A_1+3E+$5F_2$) modes. Instead only three broad bands in between 150 and 400 cm^{-1} and two sharp excitations below 150 cm^{-1} are observed. For Th_3P_4 the infrared lines are at 132, 232 and 252 cm^{-1}. The other modes are hidden in the Rayleigh part of the laser line or form hardly released knees in the broad bands. For Th_3As_4 no assignment of the observed features to particular modes was made.

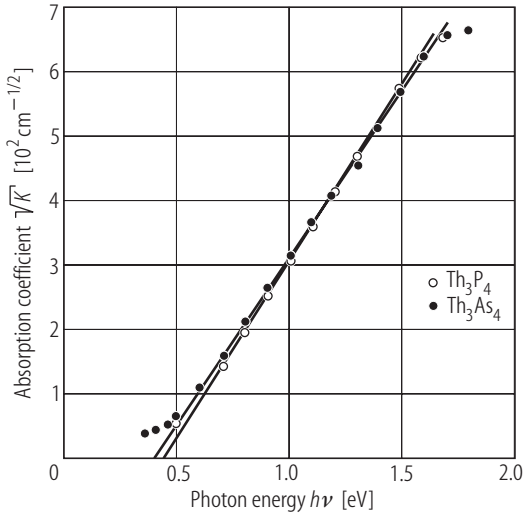

Fig. 19. Th_3X_4, X = P, As, sc. Square root of the absorption coefficient, $\sqrt{K}$, vs. photon energy, $h\nu$, in the range 0.3…1.7 eV [83SKHH]. Open circles: Th_3P_4; full circles: Th_3As_4. K was calculated from the optical conductivity data shown in Fig. 22. The solid lines are the best fits to the expression $K = (h\nu \pm h\nu_q - E_g)^2$, where $h\nu_q$ is a phonon energy and E_g stands for the gap energy. The fits yielded E_g of 0.43(1) and 0.39(1) eV for Th_3P_4 and Th_3As_4, respectively, in fairly good agreement with the values derived in [77HMZ] from the electrical transport data (0.40 and 0.43 eV, respectively).

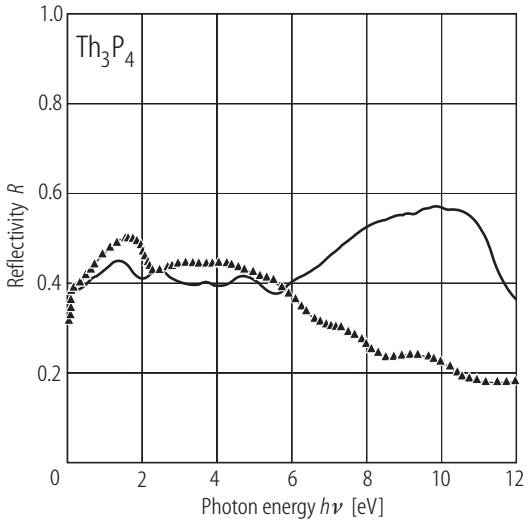

Fig. 20. Th_3P_4. Normal incidence reflectivity, R, vs. photon energy, $h\nu$, up to 12 eV, calculated by LDFT using ASW method [98KSK]. For the sake of comparison the experimental data taken from [83SKHH] (see Fig. 18**)** are shown, represented by the curve with full triangles. As in the case of U_3P_4 (compare Fig. 51**)**, the agreement between the calculated and experimental results is satisfactory only up to about 6 eV.

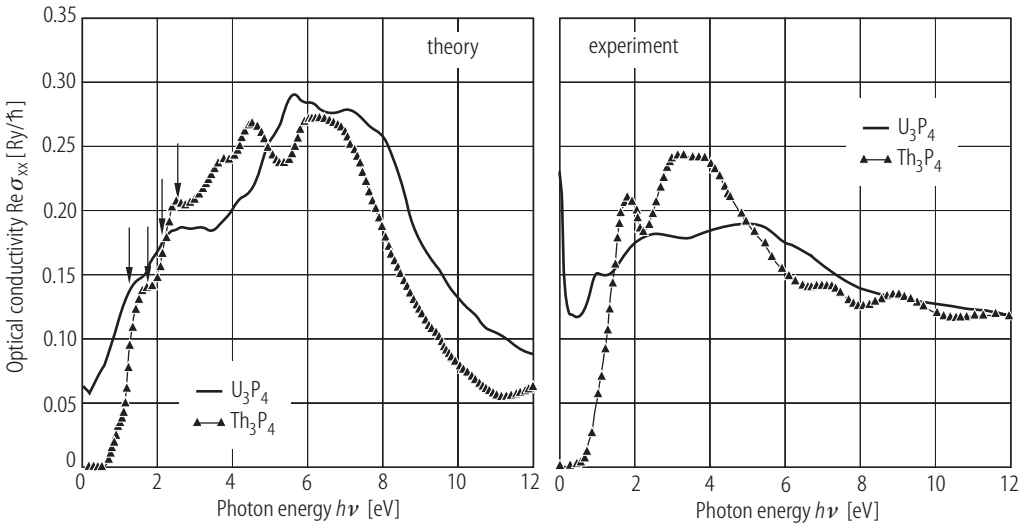

Fig. 21. Th_3P_4, U_3P_4. Real diagonal optical conductivity, Re σ_{xx}, vs. photon energy, $h\nu$, up to 12 eV, calculated by LDFT using ASW method as in Fig. 51 (left panel), compared to the experimental data taken from [83SKHH] (right panel) [98KSK]. The arrows mark some common structure elements in the optical spectra of the two compounds, reflecting their shift in energy, discussed also in [83SKHH] (see Fig. 22**)**. Note that the calculated results roughly reflect the differences between the two spectra, most apparent at low energies where Th_3P_4 exhibits an energy edge. The closing of the gap in U_3P_4 is clearly related to the U 5f states (see Fig. 49**)**. In the energy range 2.5…5 eV the optical conductivity of U_3P_4 is lower than that of Th_3P_4 because of different number and probability of the electronic transitions from the valence P 3p states to the empty U 6d states. At higher energies Re σ_{xx} is larger in U_3P_4 due to larger width of the U 6d band compared to the Th 6d band. Just the shift of the bottom of the 6d band on going from Th to U is responsible for the observed shift to lower energies of the common structural elements in the optical spectra. The presented interpretation is based on the itinerant nature of the 5f electrons, in contrast to the localized description given in [83SKHH] (see Fig. 23**)**.

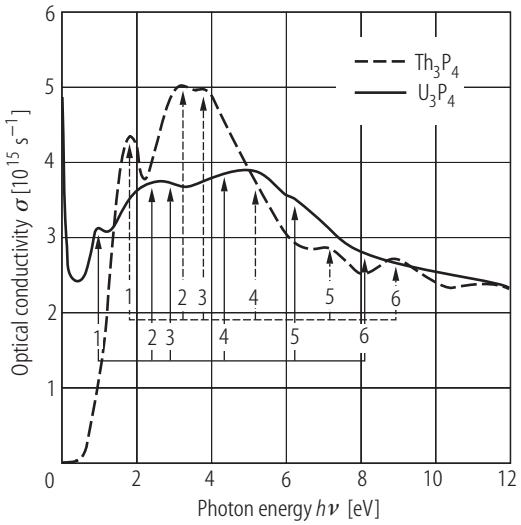

Fig. 22. Th_3P_4, U_3P_4, sc. Optical conductivity, σ, vs. photon energy, $h\nu$, from 0.03 to 12 eV [83SKHH]. Dashed curve: Th_3P_4; solid curve: U_3P_4. The optical conductivity was calculated from the reflectivity data shown in Figs. 18 and 57 using Kramers-Kronig transformation. For Th_3P_4, the onset of strong absorption near 0.5 eV is associated with the energy gap of 0.43 eV (see Fig. 19), and the observed structures are assigned to transitions from the valence p band into the empty 6d7s conduction band (marked by the six dashed arrows). In the S_4 point symmetry the $6d^1$ level splits into a singlet b_2 and a doublet e, both originating from the t_{2g} triplet, and two singlets: a and b_1, which originate from the e_g doublet; the structures 1, 4 and 5 were assigned to excitations from upper part of the valence p band into the levels b_2, a and b_1, respectively, and the structures 2 and 3 were assigned to excitations from the same part of the p band into the doublet e (see also Fig. 60).The structure 6 was assigned to p→d excitations from lower parts of the valence band, which is split in a distorted octahedral crystal field potential at the anion site. Note that the very same set of p→d transitions, but shifted by 0.85 eV to lower energies (the six full vertical arrows), describe fairly well all the structures observed in $\sigma(h\nu)$ of U_3P_4. On this basis it was concluded in [83SKHH] that the p valence band in U_3P_4 is shifted up by 0.85 eV with respect to its position in Th_3P_4, which results in closing the 0.43 eV wide semiconducting gap (see Fig. 19) and leads to the metallic conductivity. The reduction of the p→d transition energies is accompanied by the filling of the 5f-states, which are pushed down by the same amount of energy. The driving force for this band structure change (see the DOS schemes in Fig. 23) is the p-f-mixing. The binding energy of the 5f state was estimated to be ca. 1.2 eV, which points to its well localized character.

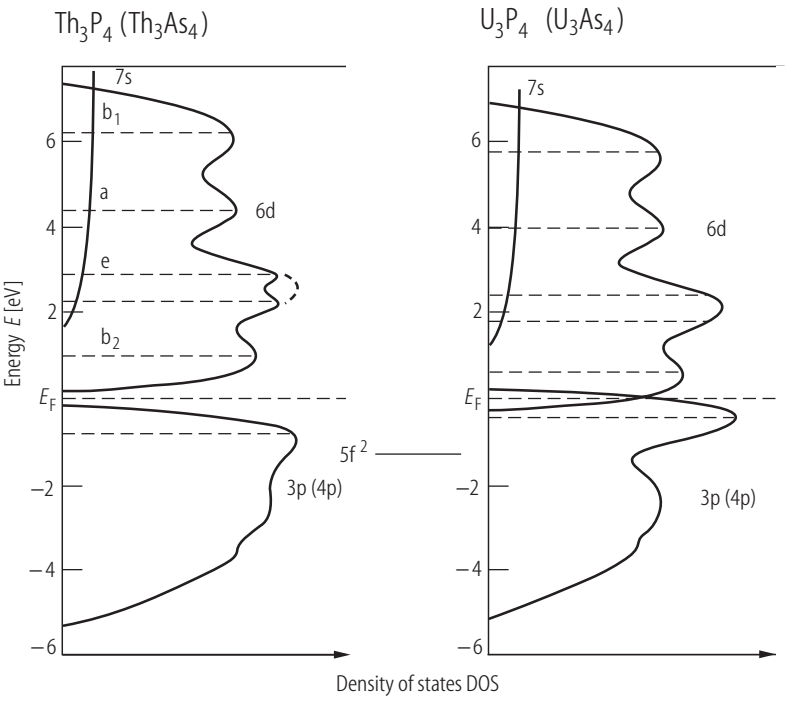

Fig. 23. Th_3X_4, U_3X_4, X = P, As. Energy level schemes as derived from optical spectroscopy [83SKHH]. DOS near E_F is dominated by the U 6d conduction band and X p valence band, both split into several peaks due to crystal field effects. In Th-based compounds there is a gap between these two bands resulting in a semiconducting behaviour (see Fig. 19). In U-based compounds the gap is closed due to p-f mixing [82TYK, 83STNT], which brings about a shift up of the p valence band by 0.85 eV and a shift down of the 5f state by the same energy. The 5f level is about 1 eV below E_F, and thus well localized. See Fig. 21 for the entirely opposite picture of itinerant 5f states e.g in U_3P_4. No f→d transitions have been identified.

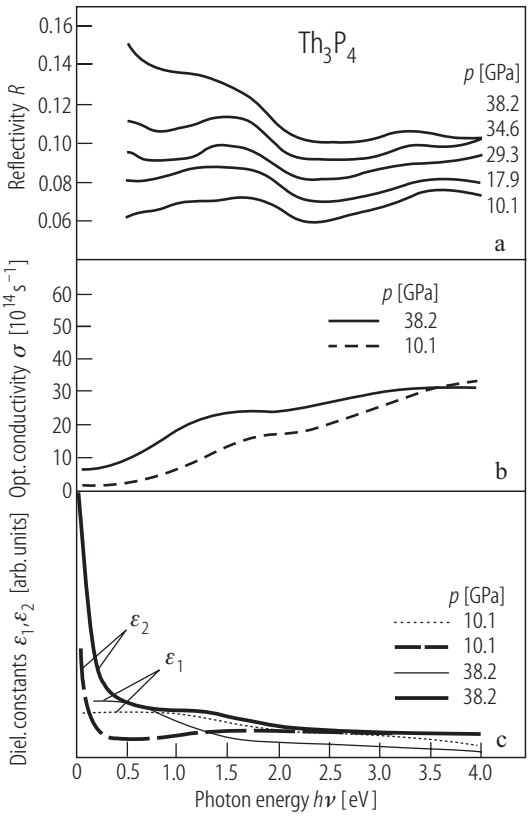

Fig. 24. Th_3P_4, sc. **(a)** Optical reflectivity, R, **(b)** optical conductivity, σ, **(c)** real and imaginary parts of dielectric constant, ε_1 and ε_2, vs. photon energy, $h\nu$, from 0.5 to 4 eV, measured under pressure up to 38 GPa [94B]. In panels **(b)** and **(c)** only the data for selected pressures of 10.1 and 38.2 GPa are shown (dashed and solid curves, respectively). In panel **(c)** the thin and bold lines correspond to $\varepsilon_1(h\nu)$ and $\varepsilon_2(h\nu)$, respectively. At low pressures the reflectivity shows a behaviour characteristic of semiconductors. A pronounced upturn in $R(h\nu)$ towards low energies and a shift of the two steps in $\sigma(h\nu)$ to lower energy, seen at 38.2 GPa, clearly indicate the appearance of metallic character. The observed changes are due to the pressure induced increase in f-electron occupation, which in turn enables sufficient p-f mixing to close the semiconducting gap in Th_3P_4, as is the case of U_3P_4 under ambient conditions.

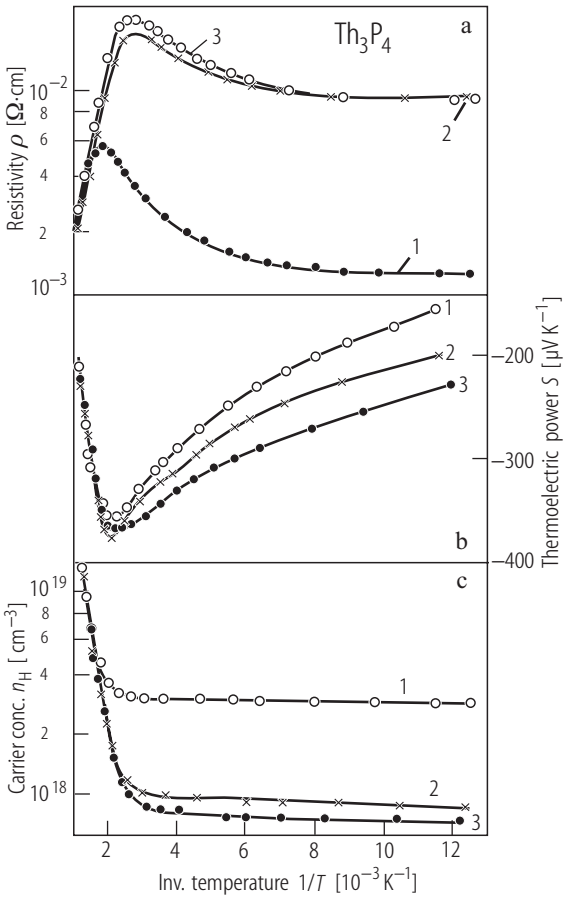

Fig. 26. Th_3P_4. **(a)** Electrical resistivity, ρ, **(b)** thermoelectric power, S, and **(c)** Hall carrier concentration, n_H, vs. inverse temperature, $1/T$, in the range 78…800 K [77HMZ]. Different symbols refer to three different samples measured. The observed properties are typical for heavily doped semiconductors, and similar to those observed for Th_3As_4 (compare Fig. 121). The activation energy changes from sample to sample in the range 0.21…0.38 eV, in dependence on the carrier concentration n_H. The extrapolation method (see the original paper) yields $E_g = 0.40$ eV.

For Fig. 25 see next page

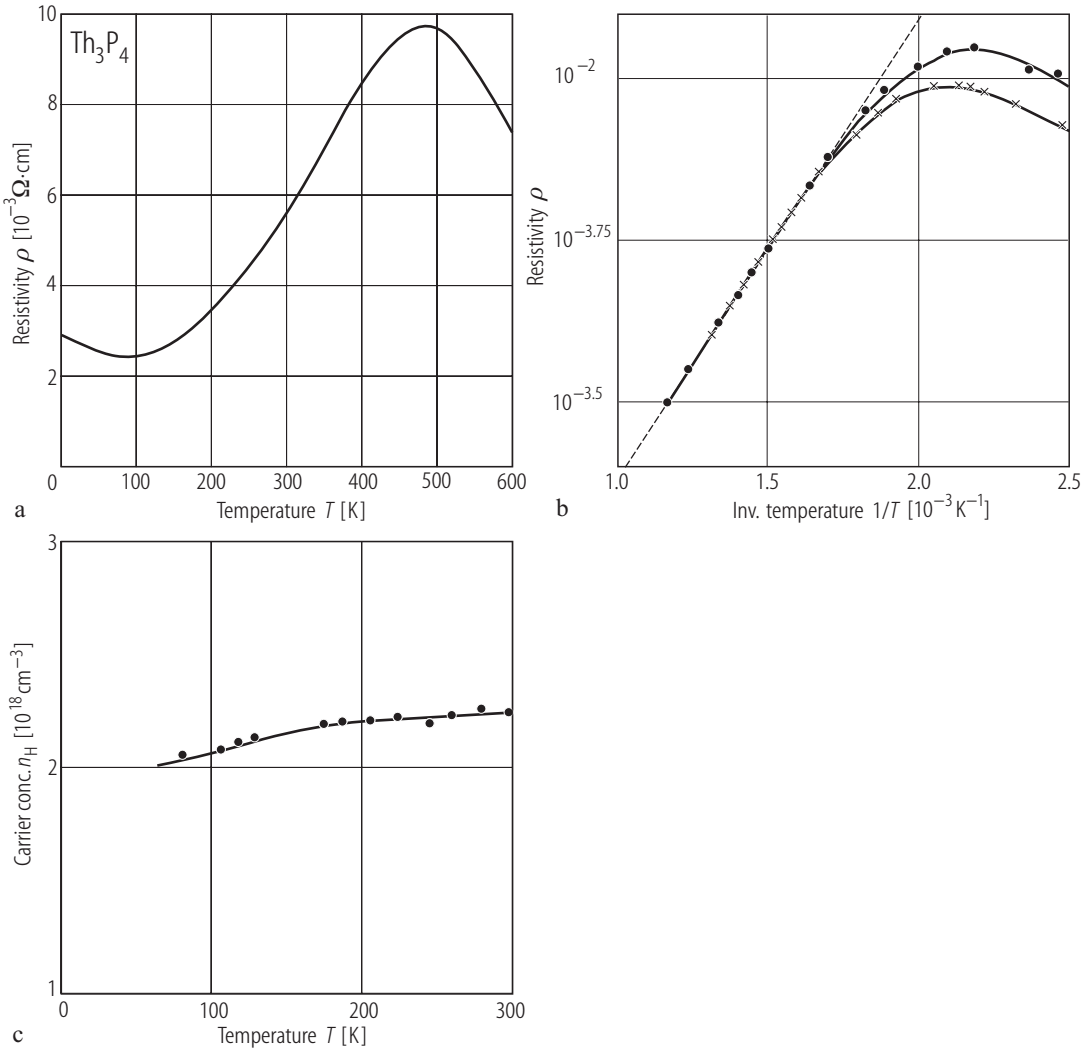

Fig. 25. Th_3P_4. **(a)** Electrical resistivity, ρ, vs. temperature, T, in the range 4.2…600 K [72THM]. **(b)** Resistivity ρ, vs. inverse temperature, $1/T$, in the range 400…860 K [72THM]. **(c)** Carrier concentration, n_H, vs. T, in the range 77…300 K [72THM]. The compound is an n-type semiconductor. Note that n_H, derived from the Hall resistivity, is almost independent of temperature. The Hall mobility at 300 K amounts to 450 $cm^2/(V\ s)$. The effective mass m^*/m_0 changes in the range 170…300 K from 0.15 to 0.55. The full circles and crosses in panel **(b)** correspond to two different samples measured. The dashed line marks an activation behaviour of the resistivity within 590 and 860 K with the energy gap $E_g = 0.29$ eV.

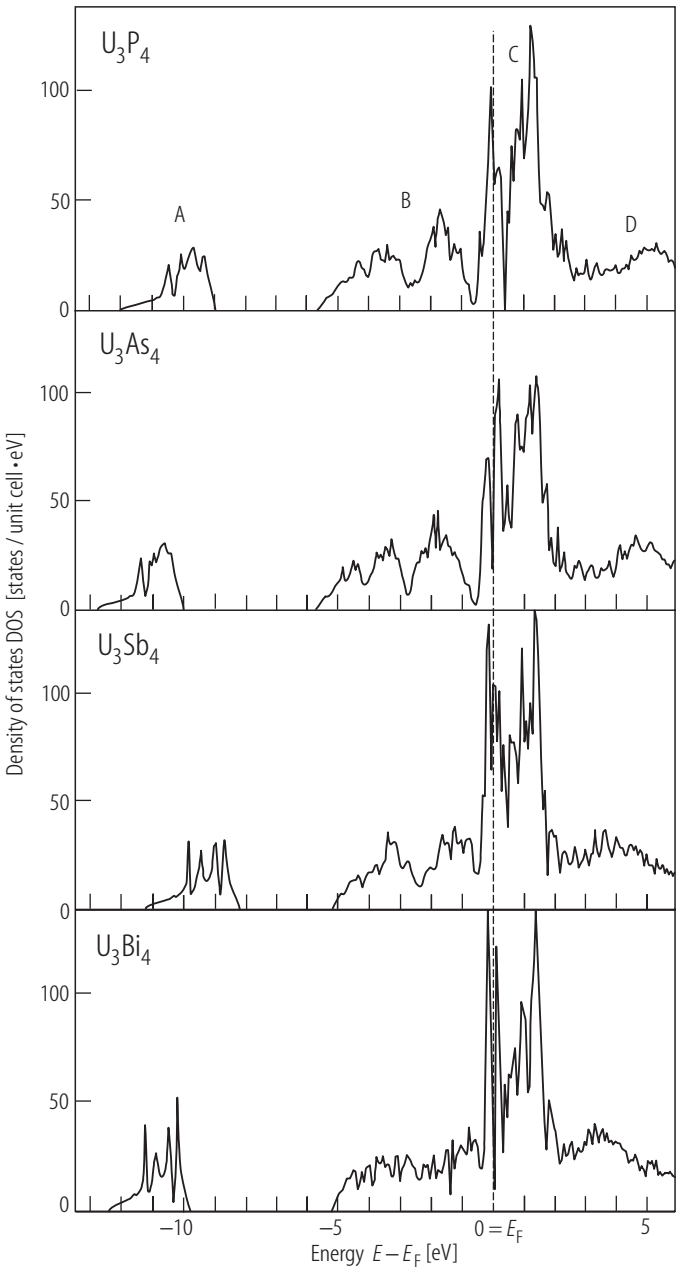

Fig. 27. U_3X_4, X = P, As, Sb, Bi. Total DOS [in states/(unit cell eV)], calculated by fully relativistic, spin-polarized LMTO method using ASA approximation with combined corrections included [99AHYP]. The LSDA calculations were based on the spin-density-functional theory with von Barth – Hedin parametrization of the exchange potential. The band regions labeled by A, B, C and D have mainly s, p-d, f and d-p characters, respectively. On going from X = P to Bi, the center of gravity of the X p band monotonically increases and that of the U 5f band decreases. For all the compounds the spin-orbit splitting at the centers of gravity is equal to 0.87 and 0.89 eV for U 5f and U 6d states, respectively. The spin-orbit splitting at the center of gravity of the X p band strongly increases along the series from 0.08 eV in U_3P_4 up to 0.94 eV in U_3Bi_4. Note that in the phosphide and the arsenide there is a quasigap between the X p band and the U 5f band (see also Fig. 33**)**, which is strongly reduced in U_3Sb_4 and fully disappears in U_3Bi_4, mainly due to increasing width of the p band. The calculated $\gamma_s(0)$ is 39, 28 and 15 mJ/(mol K^2) for U_3P_4, U_3As_4 and U_3Sb_4, respectively. For U_3Bi_4 $\gamma_s(0)$ = 0.

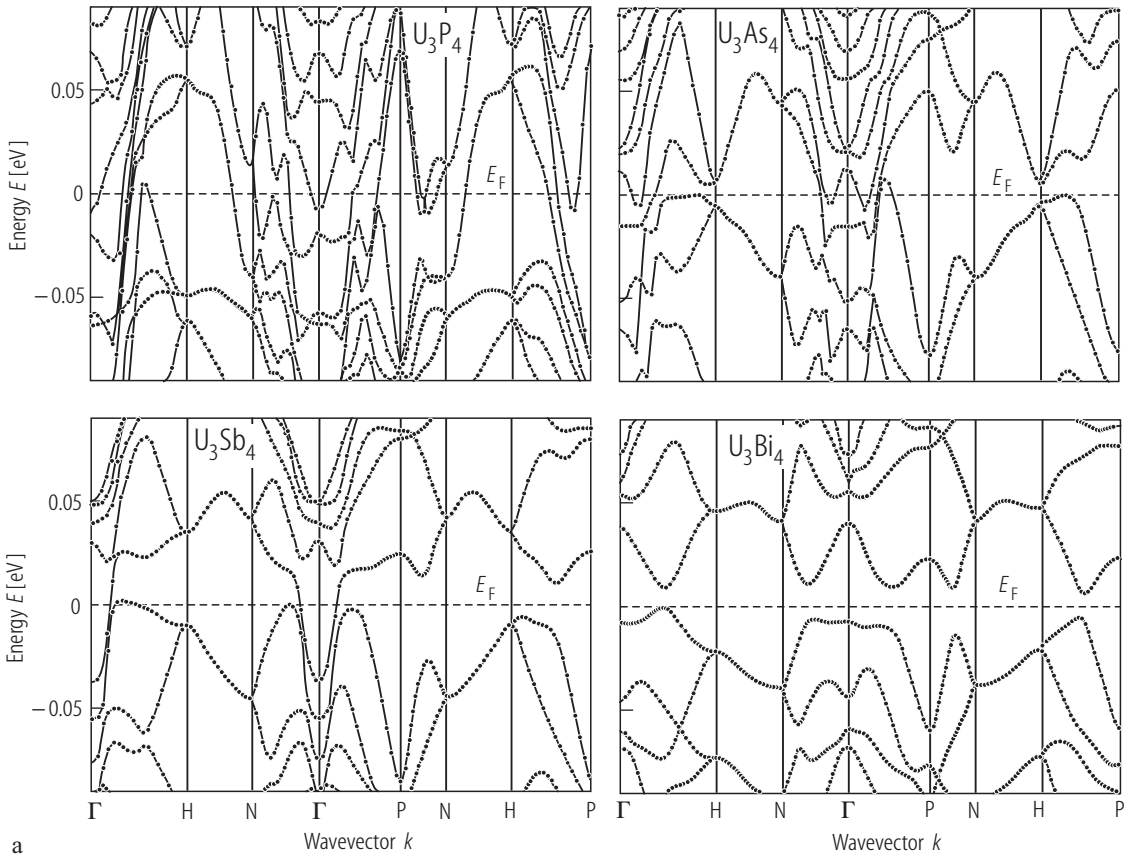

Fig. 28. U_3X_4, X = P, As, Sb, Bi. **(a)** Energy band structure near E_F [99AHYP]. Note a gap at E_F in U_3Bi_4, which has a relativistic nature and disappears after switching off the spin-orbit interaction (see also Fig. 27**)**. **(b)** Total DOS with predominant 5f character, calculated as in Fig. 27 for an energy region in the vicinity of the Fermi level [99AHYP]. Note a reduction of DOS at E_F on going from X = P to Bi. The LSDA approach predicts U_3Bi_4 to be a small gap semiconductor with an indirect gap of 0.001 eV and a direct gap of 0.005 eV (see panel **(a)**). The other three compounds are semimetals with nearly equal number of electrons and holes.

For Fig. 28(b) see next page

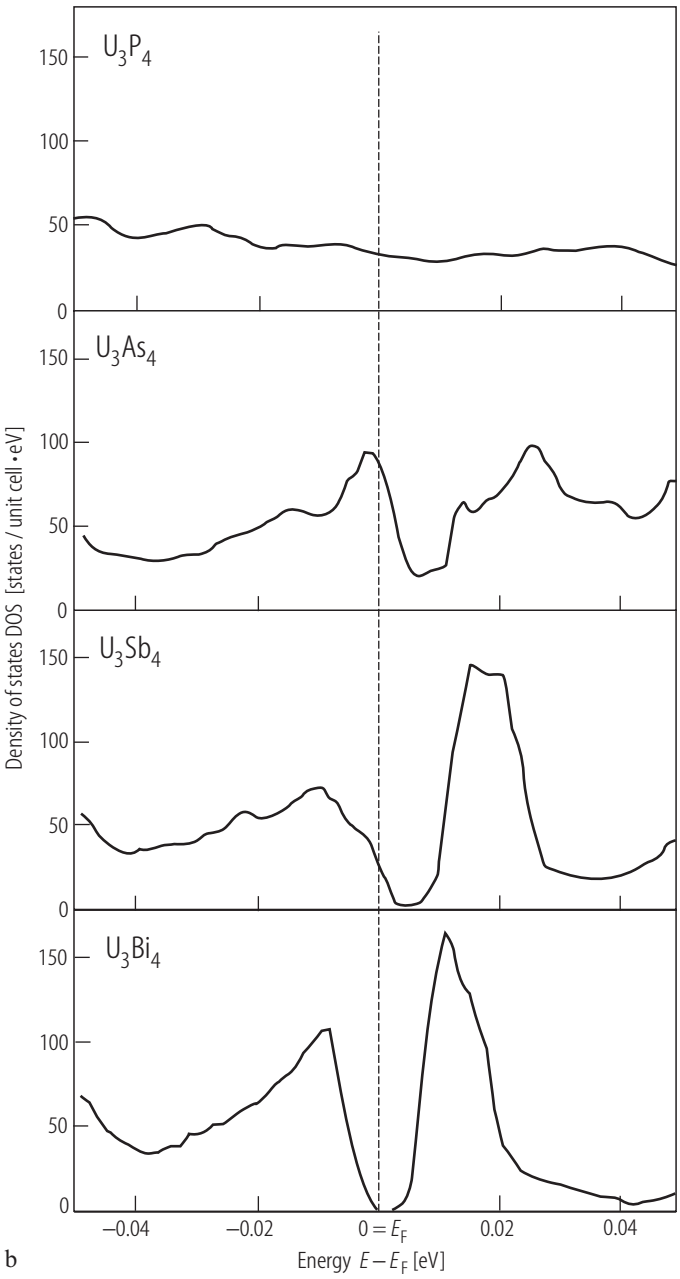
U3P4
U3As4
U3Sb4
U3Bi4
150
100
50
0
Density of states DOS [states / unit cell • eV]
−0.04
−0.02
0 = EF
0.02
0.04
Energy E − EF [eV]

b

Fig. 28(b).

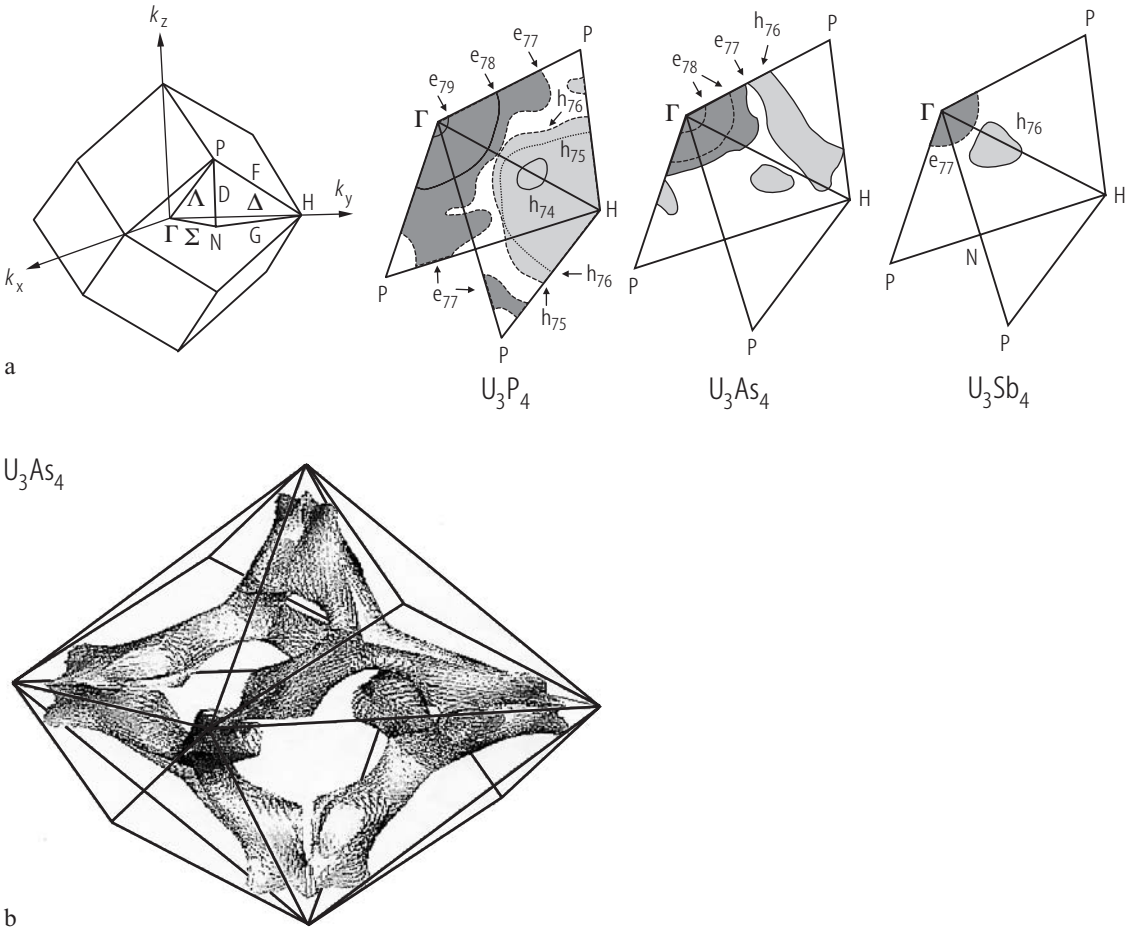

Fig. 29. (a) U_3X_4, X = P, As, Sb. Cross-sections of the Fermi surface calculated as in Fig. 27 [99AHYP]. For U_3P_4 there are a large almost spherical electron sheet e_{78} and a small electron pocket sheet e_{79}, both centered at Γ, two closed hole sheets h_{74} and h_{76} around the point H, eight small spherical hole pockets h_{74} along the Γ–H direction, and a large multiply connected electron sheet e_{77}. The Fermi surface in U_3As_4 consists of two nearly spherical electron sheets, e_{77} and e_{78} and a complicated hole sheet h_{76} (see panel **(b)**). For U_3Sb_4 only two surfaces were obtained: a large almost symmetrical electron sheet e_{77} centered at Γ and a small hole pocket h_{76} along the Γ–H direction. **(b)** U_3As_4. Hole sheet h_{76} of the Fermi surface calculated within LSDA [99AHYP].

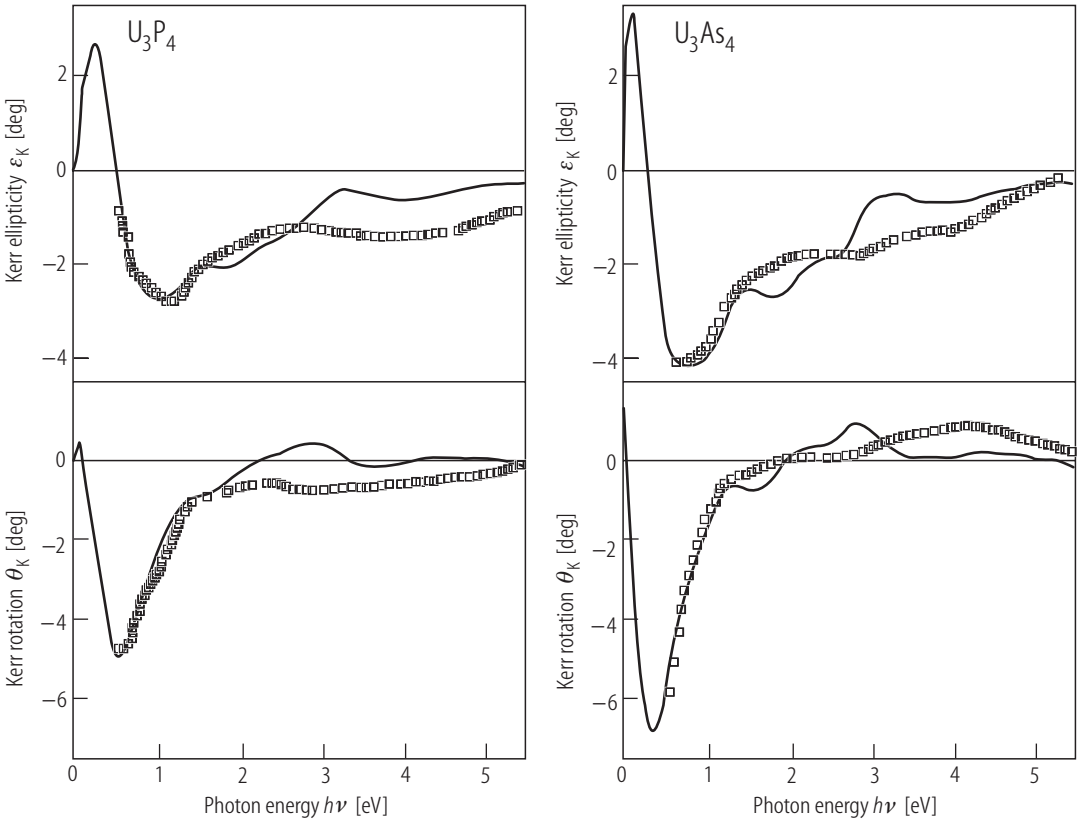

Fig. 30. U_3X_4, X = P, As. Kerr ellipticity, ε_K, and Kerr rotation, θ_K, vs. photon energy, $h\nu$, calculated *ab initio* by the LSDA method (solid lines), compared to the experimental data (squares) taken from [83SKHH] (see Fig. 60**)** [99AHYP]. Note a good agreement between the theoretical and experimental results, especially at low energies. Similar results for U_3P_4 were obtained in [98KSK] (compare Fig. 53**)**.

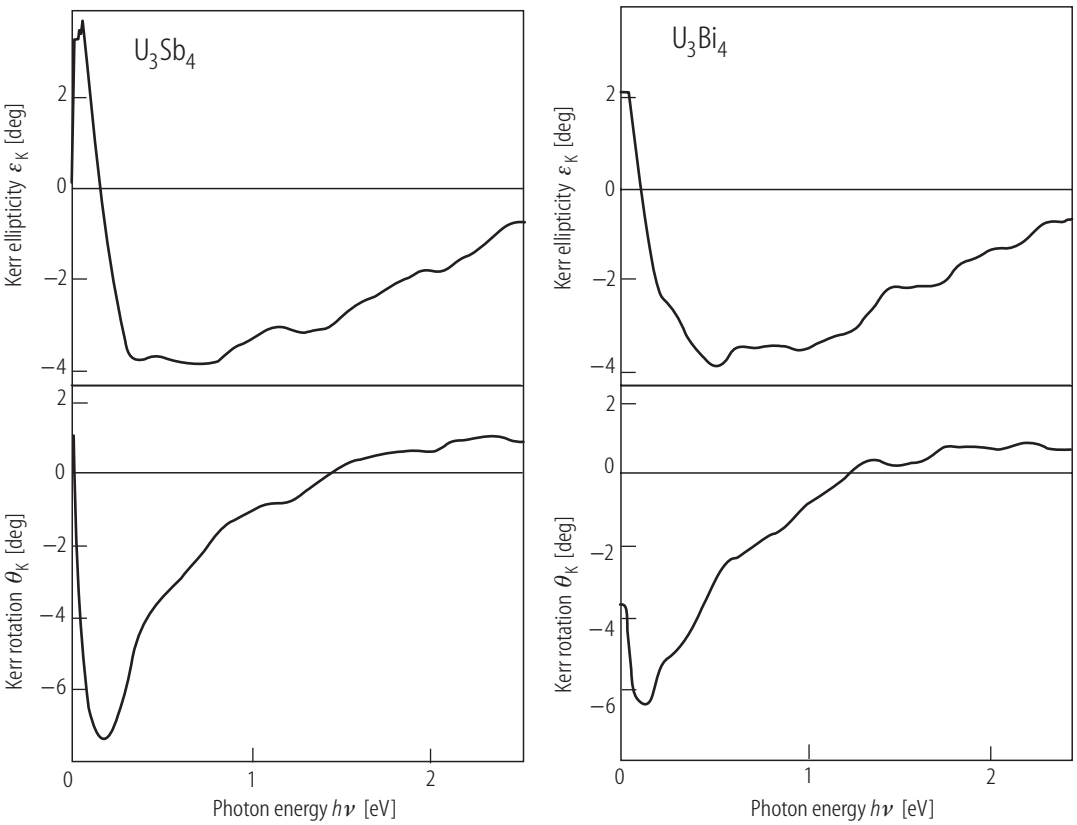

Fig. 31. U_3X_4, X = Sb, Bi. Kerr ellipticity, ε_K, and Kerr rotation, θ_K, vs. photon energy, $h\nu$, calculated *ab initio* by LSDA method [99AHYP]. Note that θ_K predicted for U_3Sb_4 exceeds 7.5 deg, which makes it one of the largest found so far. To date no experimental data are available.

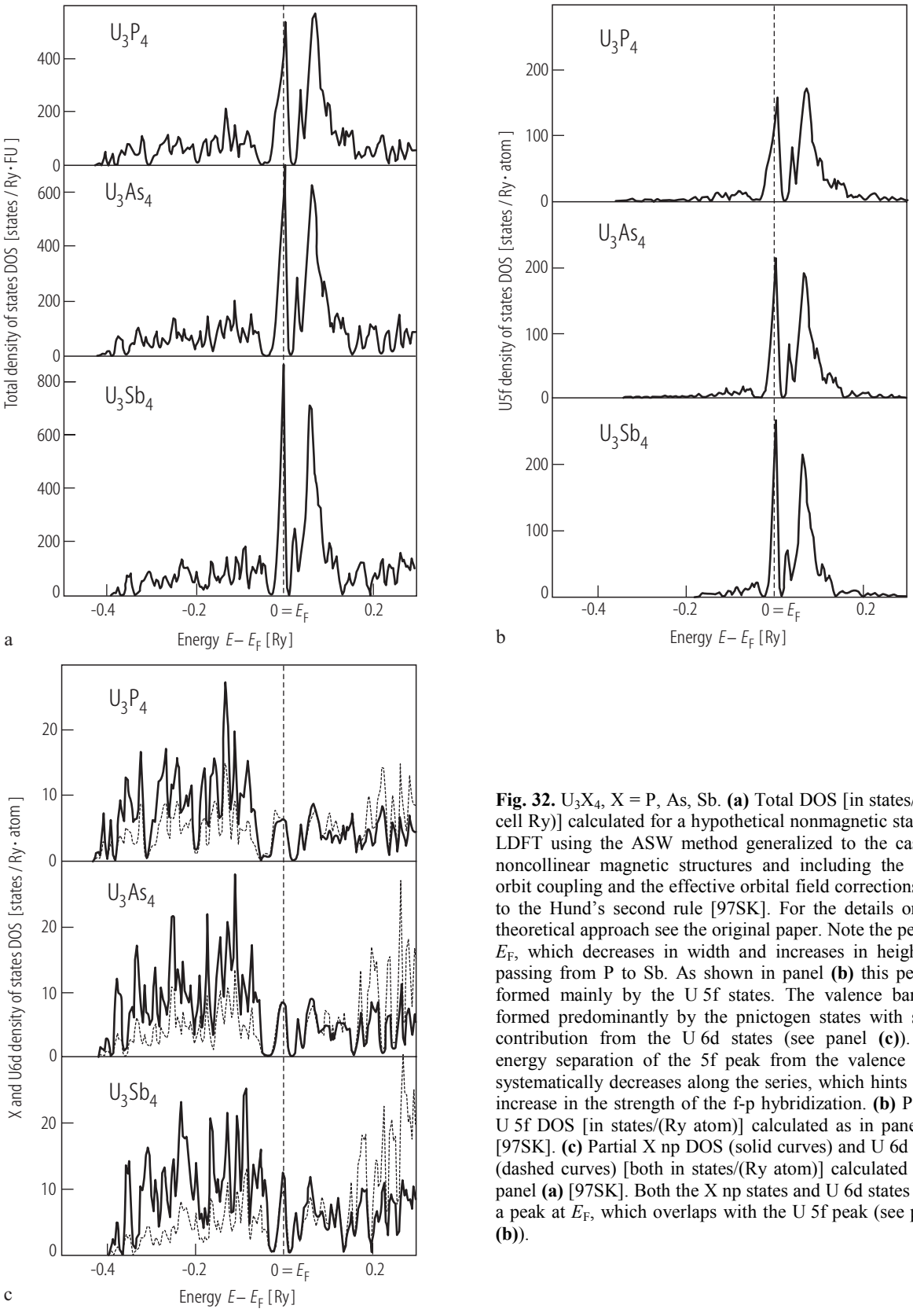

Fig. 32. U_3X_4, X = P, As, Sb. **(a)** Total DOS [in states/(unit cell Ry)] calculated for a hypothetical nonmagnetic state by LDFT using the ASW method generalized to the case of noncollinear magnetic structures and including the spin-orbit coupling and the effective orbital field corrections due to the Hund's second rule [97SK]. For the details on the theoretical approach see the original paper. Note the peak at E_F, which decreases in width and increases in height on passing from P to Sb. As shown in panel **(b)** this peak is formed mainly by the U 5f states. The valence band is formed predominantly by the pnictogen states with some contribution from the U 6d states (see panel **(c)**). The energy separation of the 5f peak from the valence band systematically decreases along the series, which hints to an increase in the strength of the f-p hybridization. **(b)** Partial U 5f DOS [in states/(Ry atom)] calculated as in panel **(a)** [97SK]. **(c)** Partial X np DOS (solid curves) and U 6d DOS (dashed curves) [both in states/(Ry atom)] calculated as in panel **(a)** [97SK]. Both the X np states and U 6d states form a peak at E_F, which overlaps with the U 5f peak (see panel **(b)**).

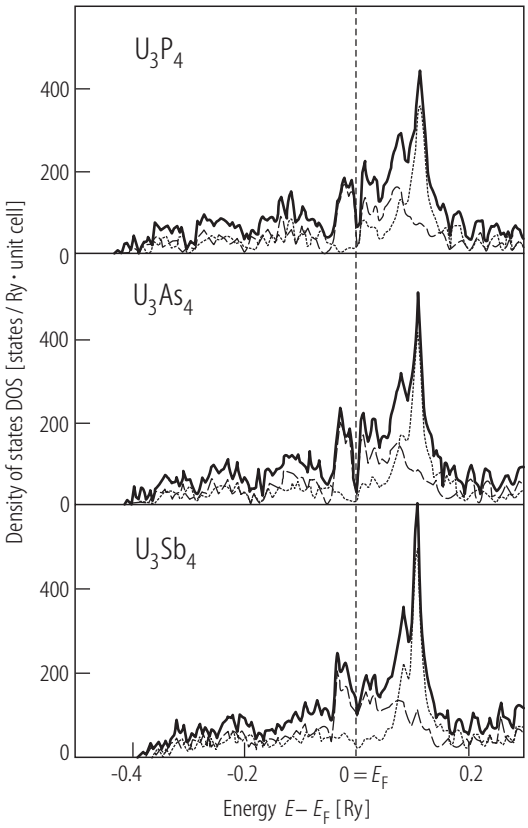

Fig. 33. U_3X_4, X = P, As, Sb. Total DOS (solid curves), partial spin-up DOS (dashed curves) and partial spin-down DOS (dotted curves) [all in states/(unit cell Ry)], calculated for a magnetic state by LDFT using the ASW method generalized to the case of noncollinear magnetic structures and including the spin-orbit coupling and the effective orbital field corrections [97SK]. Note a dip at the Fermi level, which decreases on passing from P to Sb. This minimum in DOS is mainly governed by the hybridization between the U 5f and X p states (see Fig. 48**)**.

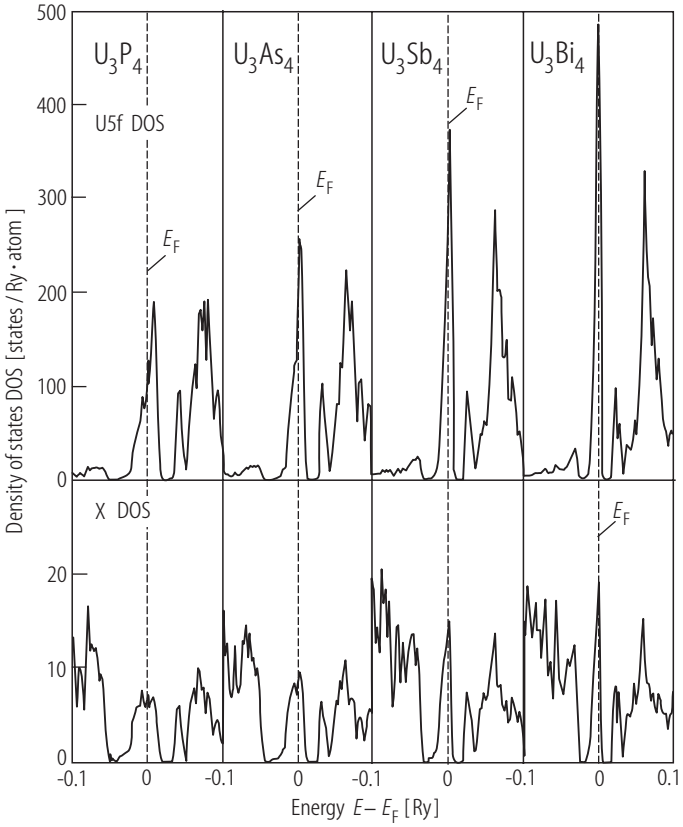

Fig. 34. U_3X_4, X = P, As, Sb, Bi. Partial DOS [in states/(Ry atom)] calculated by LDFT using a modified version of the ASW method (MASW) for a hypothetical nonmagnetic state [00KSK]. For the details on the theoretical approach see the original paper. Here, in contrast to [99AHYP] (see Fig. 27), the effects of the magnetic anisotropy and non-collinearity of the magnetic structure were taken into account. Upper panel: U 5f states; lower panel: X np states. The presence of large DOS at the Fermi level clearly indicates instability towards a magnetic state. On going from P to Bi the U 5f peak at E_F systematically becomes narrower and higher, in line with an increase in the value of the ordered magnetic moment along the series (see Table P).

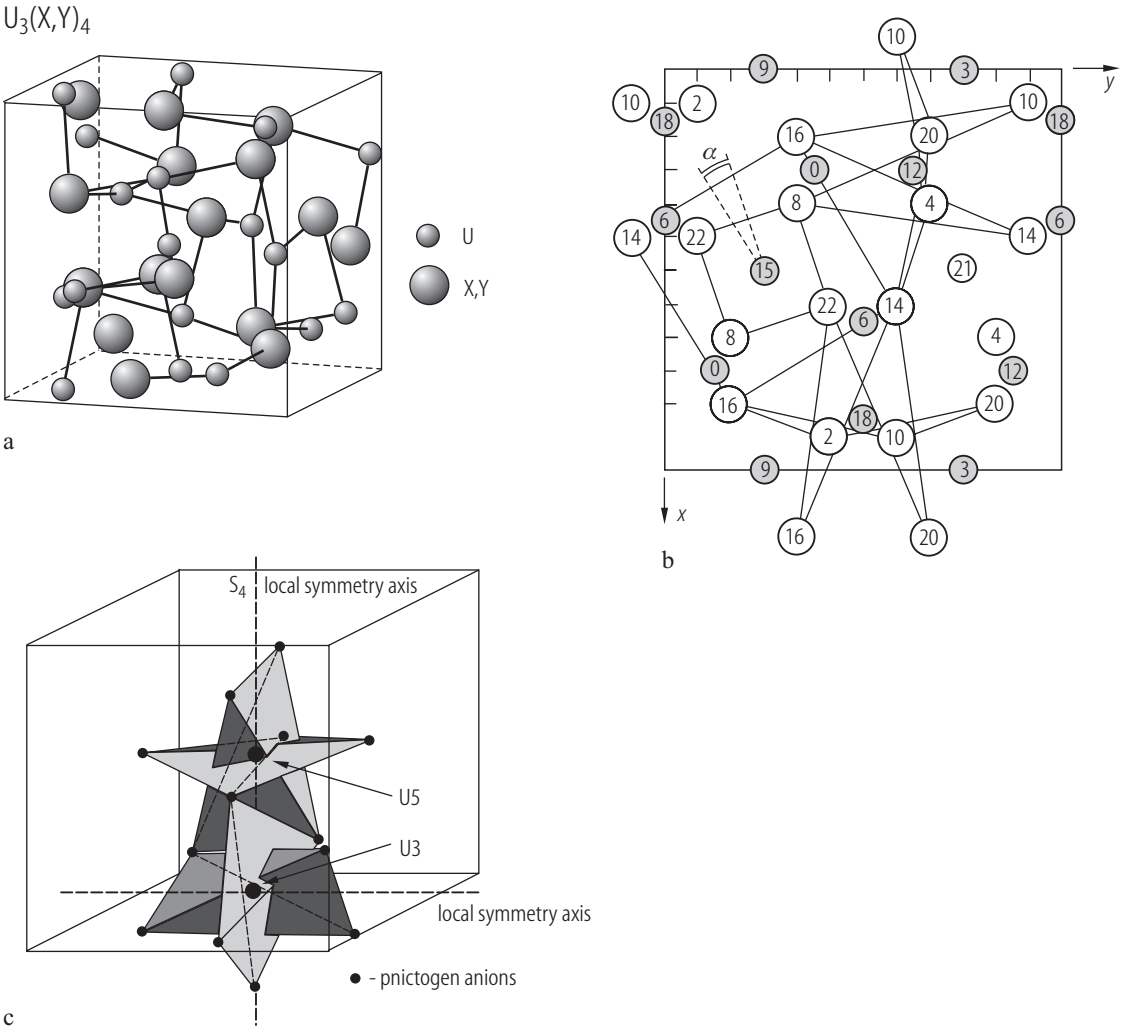

Fig. 35. U_3X_4, U_3Y_4, X = P, As, Sb, Bi, Y = S, Se, Te. Crystal structure of the Th_3P_4-type; space group $I\bar{4}3d$ [57F]. **(a)** Spatial view of the bcc unit cell [01IWMA]. The cell contains 12 U atoms and 16 pnictogen or chalcogen atoms. There exist six equivalent sublattices. **(b)** Projection of the structure on the *xy*-plane [71TMS]. The numbers inside the circles indicate the *z*-cooordinates in 1/24 of a unit. Shown are three octaverticons of X(Y) atoms corresponding to the three U atoms with *z*-positional parameters 12, 15, 18 (smaller shaded circles), where their fourfold axes (S_4 point symmetry) are perpendicular to one another. The solid lines denote two irregular tetrahedra for each octaverticon. The elongated tetrahedron is rotated against the flattened one by an angle of 12º32'. Such an arrangement of octaverticons leads to remarkable anisotropic effects in the magnetically ordered state. The corresponding crystal electric field (CEF) Hamiltonian for local S_4 symmetry is given in Fig. 71a. **(c)** Spatial view of two octaverticons around the uranium atoms U3 and U5 with their local symmetry axes perpendicular to each other, taken from [96GWH].

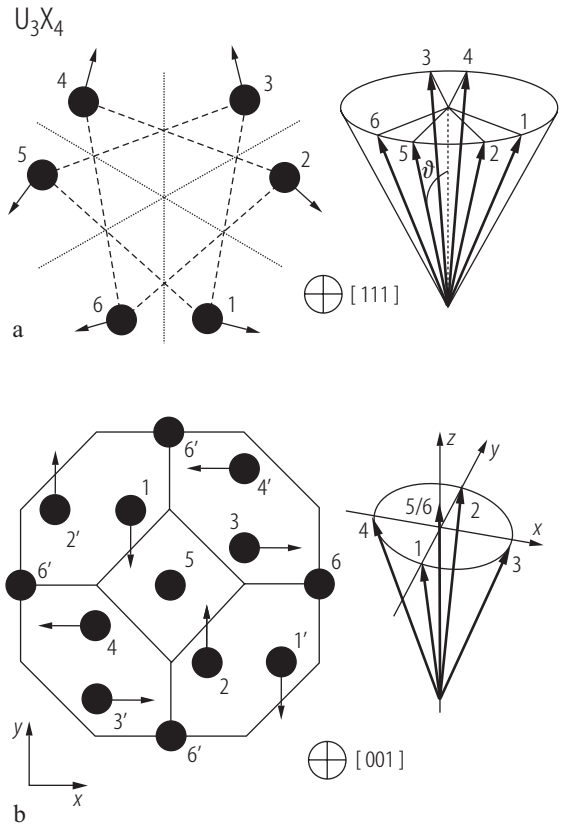

Fig. 36. U_3X_4, X = P, As, Sb, Bi. **(a)** Projection of the atomic positions of the six uranium atoms (labels from 1 to 6; large full circles) and their magnetic moments onto the (111) plane [00KSK]. Nearby, there is shown the cone formed by the magnetic moments of the six equivalent U atoms, where the cone axis was taken along the [111] direction. This axis corresponds to the easy magnetization axis in U_3P_4 and U_3As_4. **(b)** Projection of the atomic positions of the six uranium atoms and their magnetic moments onto the (001) plane [00KSK]. Nearby, the corresponding conical structure of the magnetic moments is depicted. In this case the U atoms are nonequivalent: the atoms 5 and 6 have their moments aligned along the [001] axis but the atoms 1…4 form again a conical structure. This arrangement of moments yields the [001] easy magnetization direction, as found in U_3Sb_4 and U_3Bi_4 [96GWH] (see Fig. 188). Note that the symmetry of the noncollinear magnetic structures shown in panels **(a)** and **(b)** is not lower than the symmetry of the collinear structure. The collinear arrangement of the magnetic moments is ruled out in the Th_3P_4-type structure [00KSK].

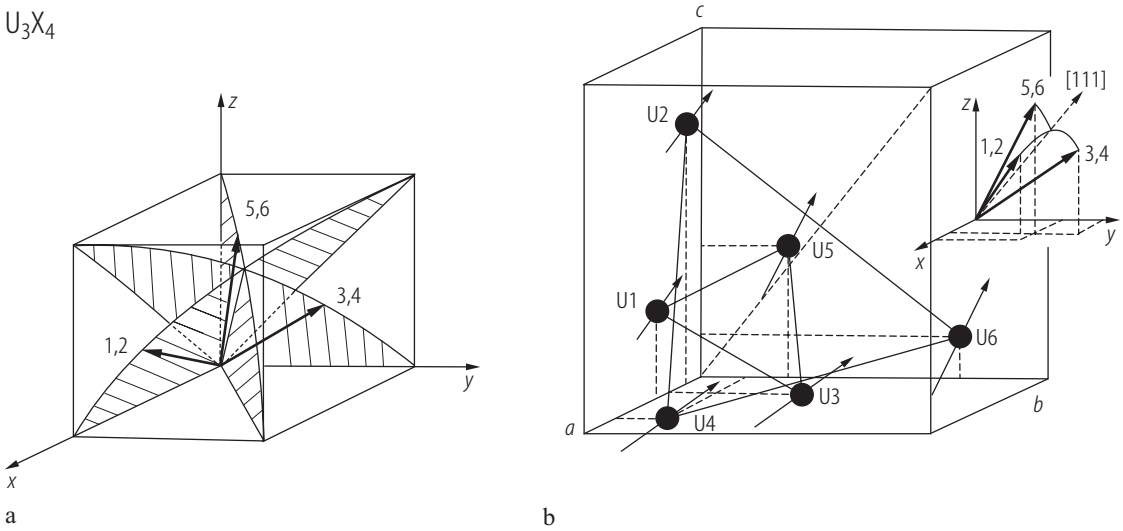

Fig. 37. U_3X_4, X = P, As. **(a)** Non-collinear three-sublattices magnetic structure [81BRTH]. The uranium atoms form three sublattices with their fourfold symmetry axes parallel to one of three main cubic diagonals. The magnetic moments are tilted from the [111] direction towards cubic axes by an angle θ and lying within [110] mirror planes. The value of θ is determined by an interplay of exchange interactions and single ion anisotropy [72PP]. The authors found $\theta = 13(6)^o$ and $25(5)^o$ for the phosphide and the arsenide, respectively, but more recent measurements have shown these values to be much smaller [99WGH]. **(b)** Multiaxial model of the magnetic structure [99WGH]. The location of U(1)…U(6) atoms in the body centered Bravais lattices of the Th_3P_4–type structure is as follows: U1 – (3/8, 0, 1/4), U2 – (1/8, 0, 3/4), U3 – (1/4, 3/8, 0), U4 – (3/4, 1/8, 0), U5 – (0, 1/4, 3/8), U6 – (0, 3/4, 1/8). The magnetic moments $p_i = (uvw)$ in a three-axial arrangement ($v = w$) are confined within the (110) symmetry planes (panel **(a)**). Hence only two parameters u and v are needed to describe the magnetic structure.

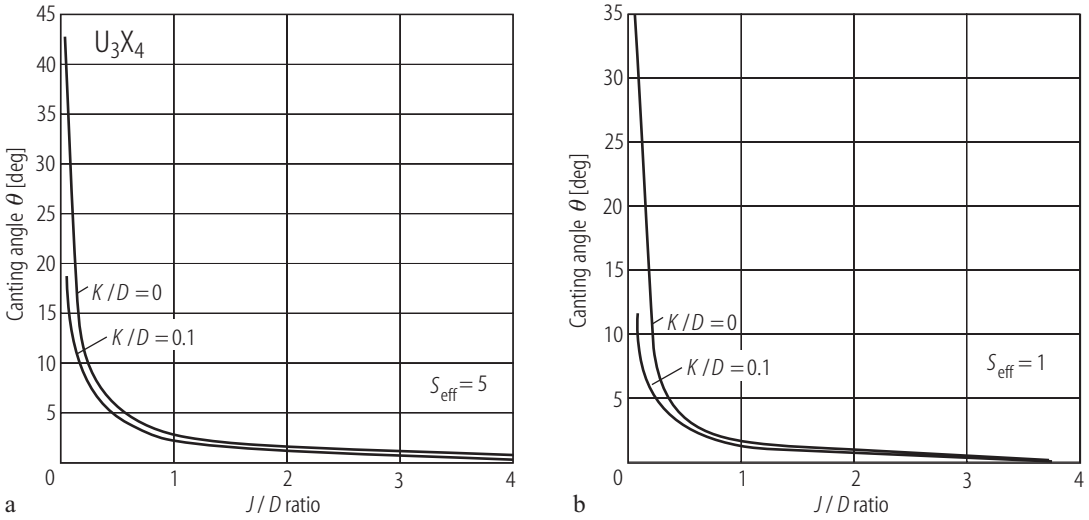

Fig. 38. U_3X_4, X = P. Magnetic moments canting angle, θ, vs. the ratio J/D, of the exchange to crystal field interactions, calculated in MFA for the effective spin **(a)** $S_{eff} = 5$ and **(b)** $S_{eff} = 1$ [76WPP]. The theoretical model contains the isotropic (J) and uniaxial anisotropic (K) exchange interactions as well as three-axial crystal field (D) terms. Note that the magnetic structure becomes asymptotically collinear if the magnitude of J exceeds that of D more than a factor of 4. See [79PKK] for the calculations of the Curie temperature, the magnetization and the paramagnetic susceptibility.

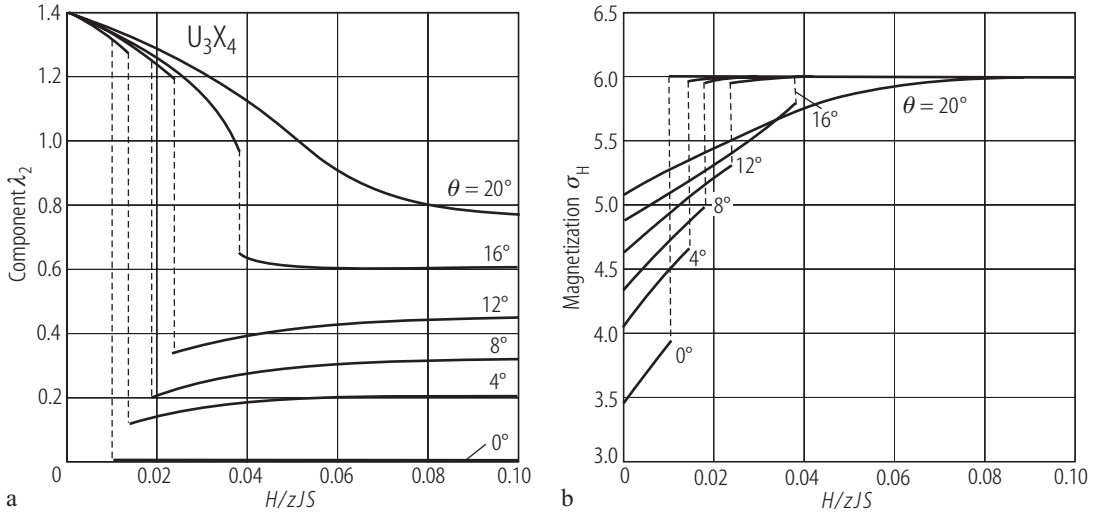

Fig. 39. U_3X_4, X = As. **(a)** Transverse magnetization component of the Landau development, λ_2, and **(b)** the resulting magnetization, σ_H, vs. reduced magnetic field, H/zJS (in usual meaning), calculated within a microscopic spin model for different values of the magnetic moments canting angle, θ [80K2]. Note from panel **(b)** that the discontinuity $\Delta\sigma_H$ decreases with the increase of θ. This feature is in agreement with the experimental data for U_3P_4 and U_3As_4 (see [81BRTH]). For the details on the microscopic model see the original paper. Another theoretical model, which contains a three-axial single-ion anisotropy and exchange interactions within MFA is considered in [76WPP] and [79PKK].

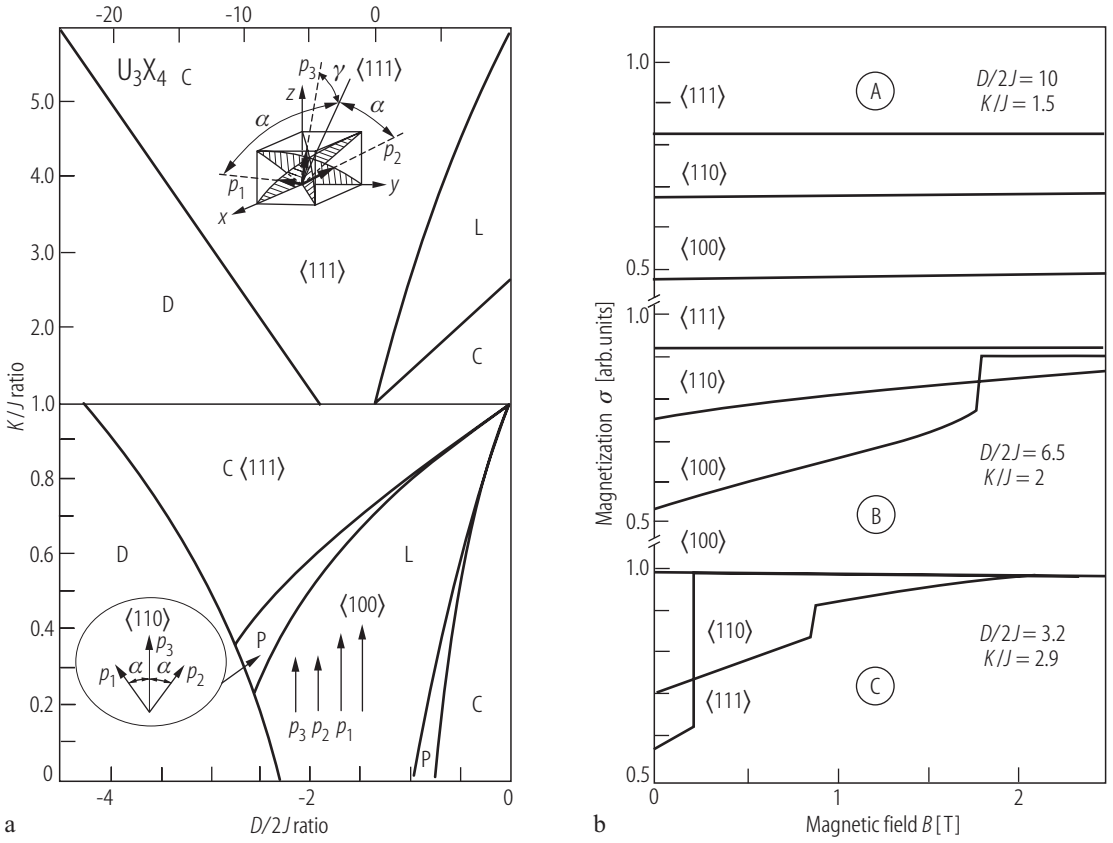

Fig. 40. U_3X_4, X = P, As, Sb. **(a)** Theoretical phase diagram derived within a microscopic phenomenological spin model with crystal field and anisotropic exchange interactions included in the case of T = 0 K and B = 0 T [87HMOP]. $D/2J$ is the crystal field anisotropy and K/J is the exchange anisotropy, where J is the exchange interaction tensor. There are several different spin structures predicted (for detailed explanation see the original paper). The structure C corresponds to the noncollinear three-axial ferromagnetic structure of U_3P_4 and U_3As_4 (see Fig. 37**)**. The structure L corresponds to the collinear two-sublattices ferrimagnetic structure of U_3Sb_4 (compare Fig. 36b). The structure P is also three-axial with the magnetic moments confined to the (110) plane. The region D corresponds to a disordered magnetic structure. **(b)** Magnetization, σ, vs. magnetic field, B, along the [100], [110] and [111] axes calculated within the model from panel **(a)** for three selected values of $D/2J$ and K/J [87HMOP] (see also [88O]). The upper panel corresponds to U_3P_4 (the spin structure C, no magnetization jumps), the middle panel reflects the case of U_3As_4 (the spin structure C, magnetization jump for the [100] axis), the bottom panel describes the behaviour in U_3Sb_4 (the spin structure L, magnetization jumps for the [111] and [110] axes). Note a good agreement between these theoretical results with the experimental data shown in Figs. 64, 80 and 193 for U_3P_4, U_3As_4 and U_3Sb_4, respectively.

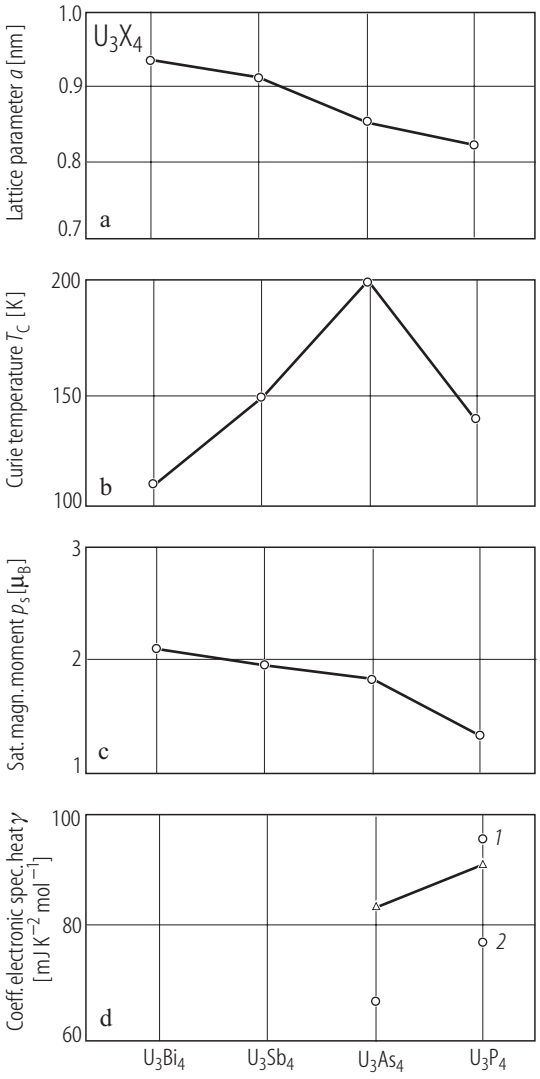

Fig. 41. U_3X_4, X = P, As, Sb, Bi. General properties: **(a)** lattice parameter, a; **(b)** Curie temperature, T_C; **(c)** saturation magnetic moment, p_s; **(d)** linear coefficient of the electronic specific heat, $\gamma(0)$ [01IWMA]. The data in panel **(d)** denoted with open circles are cited from [86ABHM]. Labels 1 and 2 denote the $\gamma(0)$ values extrapolated from the temperatures above and below 2.6 K, respectively (see Fig. 96b). Note that the value of T_C for U_3P_4 breaks the general trend of monotonic change on going from X = P to X = Bi, observed for all four compounds in the values of a and p_s.

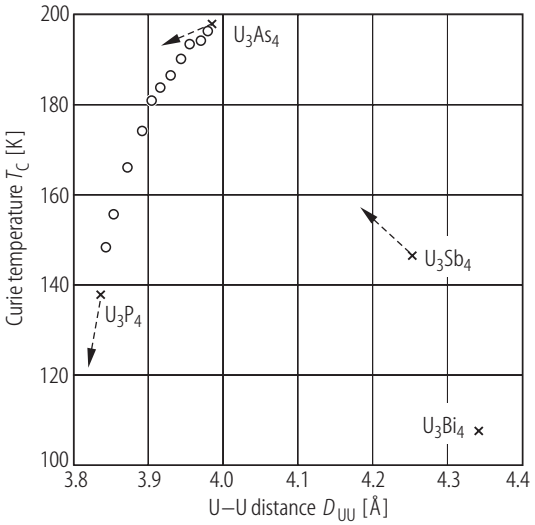

Fig. 42. U_3X_4, X = P, As, Sb, Bi. Curie temperature, T_C, vs. U–U distance, D_{UU} [86HMD]. Crosses: stoichiometric compounds; open circles: U_3P_4–U_3As_4 solid solutions (the data taken from [70TM]). The dashed arrows mark the pressure effect, as derived for U_3P_4 and U_3As_4 from the data obtained for the U_3P_4-rich and the U_3As_4-rich mutual solid solutions, and estimated for U_3Sb_4 from the high pressure resistivity data (see Fig. 196), assuming the same compressibility for this compound as that calculated for U_3P_4 ($dD_{UU}/d(D_{UU}p) = 5.1 \cdot 10^{-3}$ GPa^{-1}).

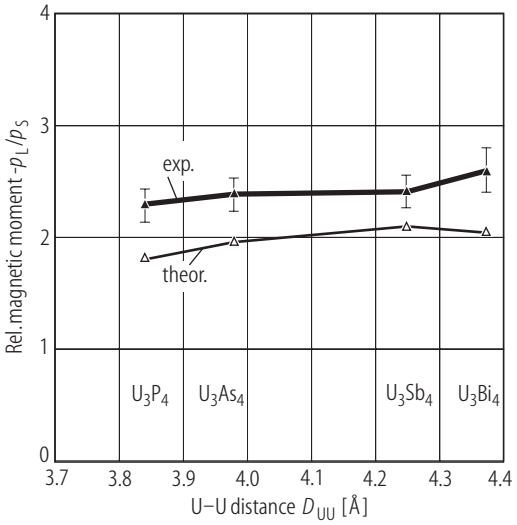

Fig. 43. U_3X_4, X = P, As, Sb, Bi, sc. Ratio of the orbital and spin components of uranium magnetic moment, $-p_L/p_S$, vs. U-U distance, D_{UU} [99WGH]. Full triangles: experimental data from polarized neutron study; open triangles: calculated values taken from [97KSK1] and [97SK]. In the case of U_3Sb_4 and U_3Bi_4 the values averaged on two magnetic sublattices are shown (see Table P). Note that the theoretical values are much smaller than the experimental ones.

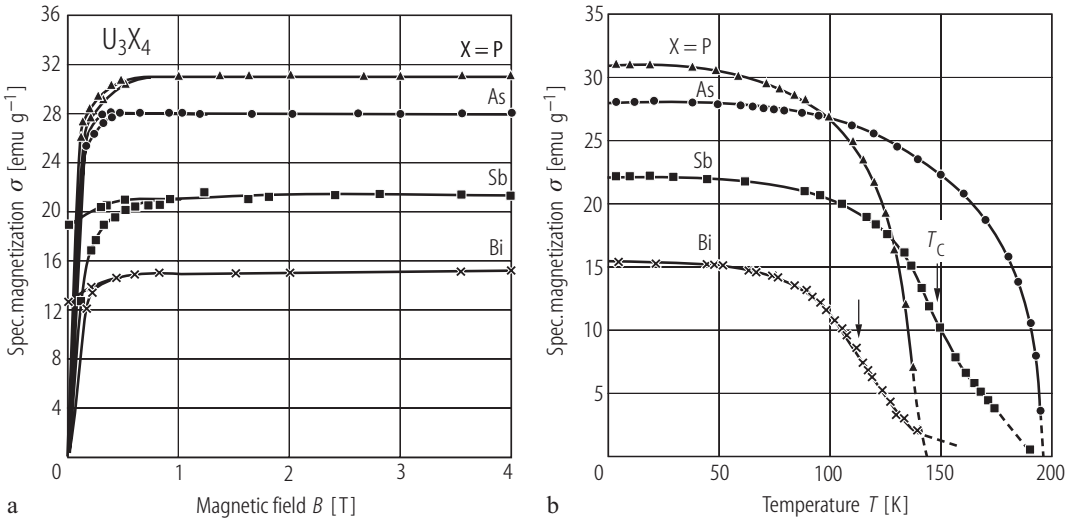

Fig. 44. U_3X_4, X = P, As, Sb, Bi. **(a)** Specific magnetization, σ, vs. magnetic field, B, up to 4 T [71TSB]. In the case of U_3P_4 and U_3As_4 sets of small single crystals were used. The obtained values of the ordered moments per uranium ion p_o = 1.55 and 1.77 μ_B, respectively, are close to those derived in other magnetization and neutron diffraction experiments [81BRTH]. The moments found for powder samples of U_3Sb_4 and U_3Bi_4, p_o = 1.60 and 1.44 μ_B, respectively, are somewhat lower than the average values of 1.82 and 1.88 μ_B, respectively, determined in [96GWH] by neutron diffraction on single crystals. **(b)** Magnetization, σ, vs. temperature, T [71TSB]. The Curie temperatures were found to be close to that displayed in Table H. Note a different behaviour of the magnetization of U_3P_4 and U_3As_4 on the one side and that of U_3Sb_4 and U_3Bi_4, on the other side, which results from the different magnetic structures of these two groups of compounds (see [96GWH]).

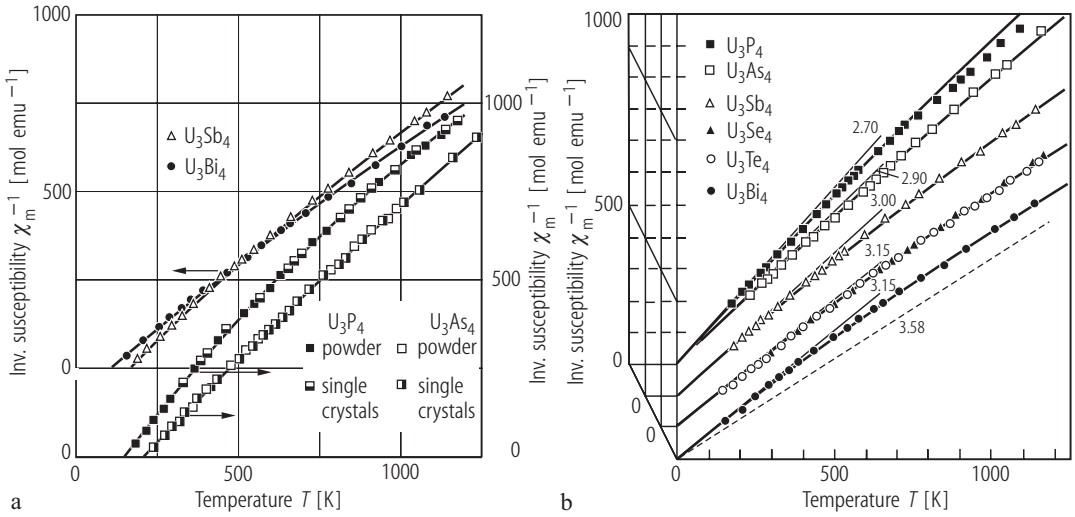

Fig. 45. U_3X_4, X = P, As, Sb, Bi. **(a)** Inverse molar magnetic susceptibility, χ_m^{-1}, vs. temperature, T, up to 1200 K measured on powder and single-crystalline specimens [71TMS]. Note different vertical scale for U_3P_4 and U_3As_4. The compounds order ferromagnetically at T_C = 138, 198, 146 and 108 K, for the phosphide, arsenide, antimonide and bismuthide, respectively. In the range T_C…400 K $\chi_m^{-1}(T)$ for all the phases follows a Curie Weiss law with the parameters given in Table F. The solid lines are fits of the experimental data to the formula $\chi_m^{-1} = [(A/T) + B]^{-1} - \lambda$ with the parameters listed in Table H. **(b)** Inverse molar magnetic susceptibility, χ_m^{-1}, vs. temperature, T, up to 1200 K upon subtraction of the molecular field constant λ (see panel **(a)**) [71TMS]. For completeness the susceptibility data obtained for U_3Se_4 and U_3Te_4 are also presented. The thin solid lines mark the slopes corresponding to the magnetic moments of the ground state (the values in μ_B as indicated). The dashed straight line represents $\chi_m^{-1}(T)$ with the magnetic moment equal to the free U^{4+} ion value.

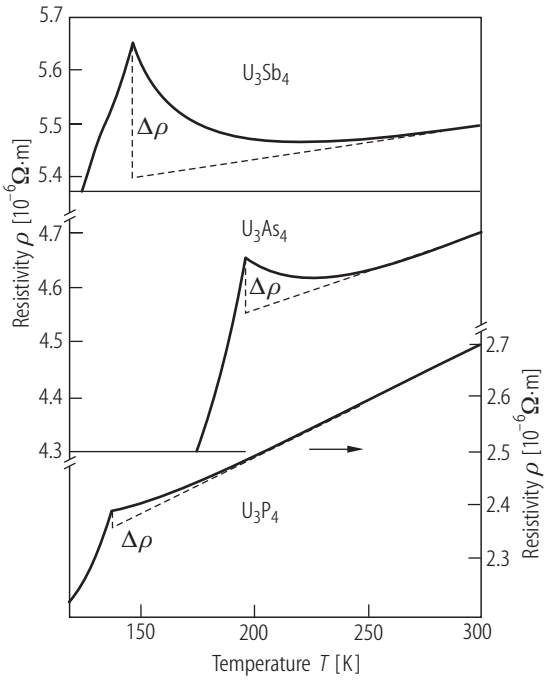

Fig. 46. U_3X_4, X = P, As, Sb, sc. Electrical resistivity, ρ, vs. temperature, T, in the vicinity of T_C and in the paramagnetic region [81HMK]. T_C = 137.2, 196.3 and 147.2 K for U_3P_4, U_3As_4 and U_3Sb_4, respectively. The resistivity behaviour near T_C is characterized for such ferromagnetic semimetals by the ratio $\Delta\rho/\rho(T_C)$, where the value of $\Delta\rho$ is defined by the dashed straight lines. This ratio amounts to 1.10%, 2.03% and 4.54% for U_3P_4, U_3As_4 and U_3Sb_4, respectively, and allows estimating the effective masses in these compounds. Then, the ratio k_F/Λ was estimated to be 0.426, 0.347 and 0.23 Å^{-2} for U_3P_4, U_3As_4 and U_3Sb_4, respectively, where k_F is the Fermi wave vector and Λ is the effective radius of the Brillouin zone (for explanation see also [86HMD]).

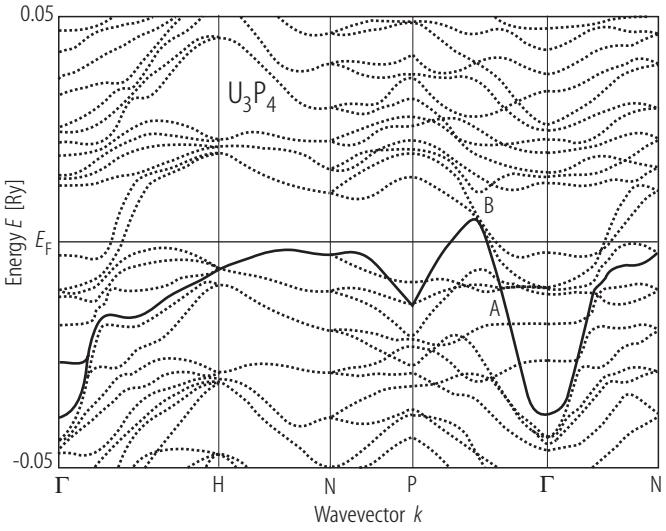

Fig. 47. U_3P_4. Electronic band structure near the Fermi level, calculated as in Fig. 48 [96SK]. Note a small number of states at E_F. The narrow bands above and below E_F have 5f character (compare Fig. 48**)**. Two broad bands (solid line) starting at the Γ point at about 0.04 Ry below E_F, which first cross the 5f bands below E_F (A), then cross the Fermi level and eventually reach 5f bands above E_F (B), are mostly 3p bands of phosphorus. Their hybridization with U 5f states is responsible for the formation of the energy interval with low DOS in the vicinity of the Fermi level.

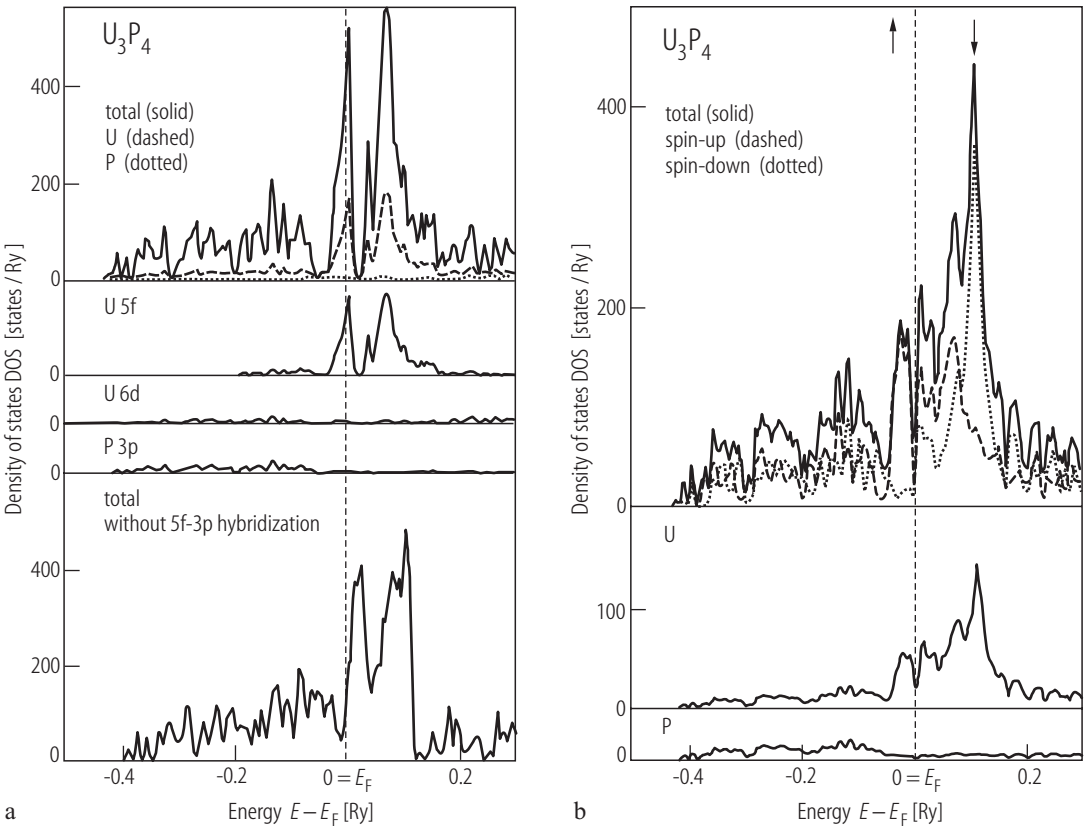

Fig. 48. U_3P_4. Total and partial DOS calculated using LSDF theory and ASW method with incorporated spin-orbit coupling, noncollinear moment arrangement and an effective orbital field responsible for Hund's second rule [96SK]. The total DOS is given per formula unit, the partial DOS is given per atom. **(a)** Hypothetical nonmagnetic state. Two prominent peaks, at E_F and 0.08 Ry above E_F, contain mostly U 5f states split by spin-orbit coupling. As apparent from the lower panel, showing DOS calculated without taking into account the U 5f-P 3p hybridization, the separation of 5f peaks originates from the repulsion of the bands due to the f-p mixing. High DOS at E_F implies a magnetic instability of the system. **(b)** Ferromagnetic ground state. The 5f states show a very strong spin polarization with the spin down states occupying mostly the high energy peak at about 0.11 Ry above E_F, and the spin up states occupying a rather broad band from –0.04 to 0.1 Ry (see the arrows). The broadening of the latter structure is due to the spin-orbit coupling and the effective orbital field. Just at E_F there is a narrow dip in DOS, which results from the f-p mixing (compare panel **(a)**).

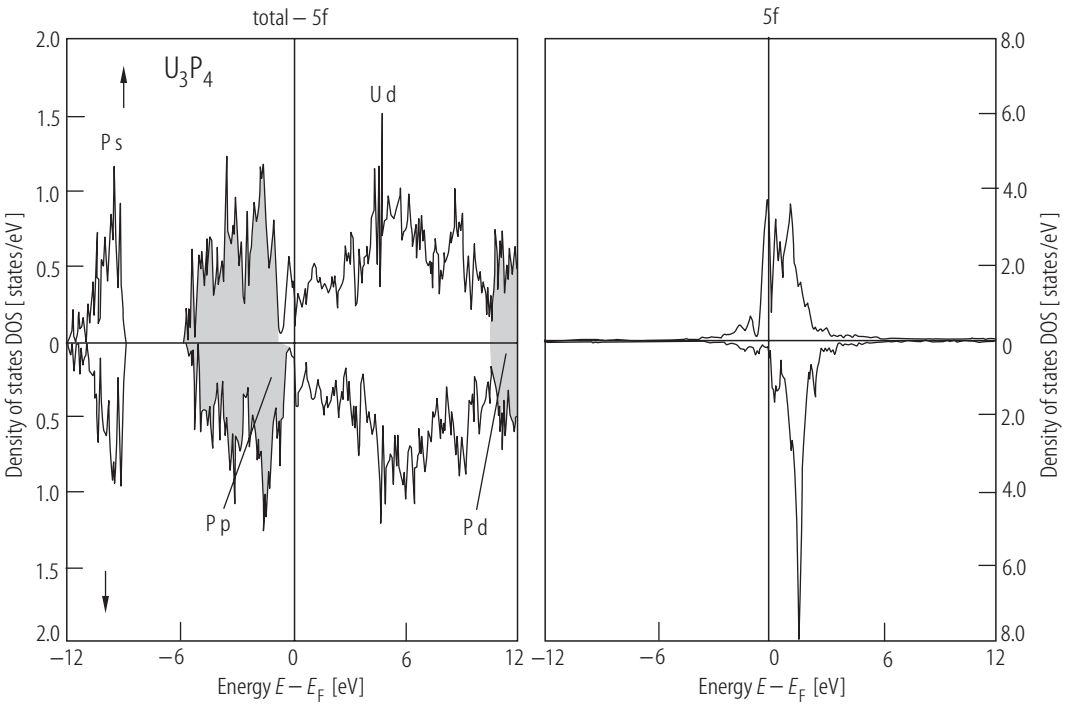

Fig. 49. U_3P_4. Partial DOS calculated by LDFT using ASW method [98KSK]. Right panel: the spin resolved 5f DOS; left panel: total DOS minus 5f contribution. The shaded states give main contribution to DOS. There is no gap between the P 3p and U 6d states because of the presence at E_F spin-polarized U 5f states and because the spin-up U 6d band is shifted to lower energies and approaches the 3d valence band. The 6d spin polarization is induced by a strong spin polarization of the U 5f states. The U 6d DOS differs from the Th 6d DOS (compare Fig. 16**)** due to hybridization between the U 5f and U 6d states. This effect was not taken into account in the discussion of the optical spectra in [83SKHH] (see Fig. 22**)**.

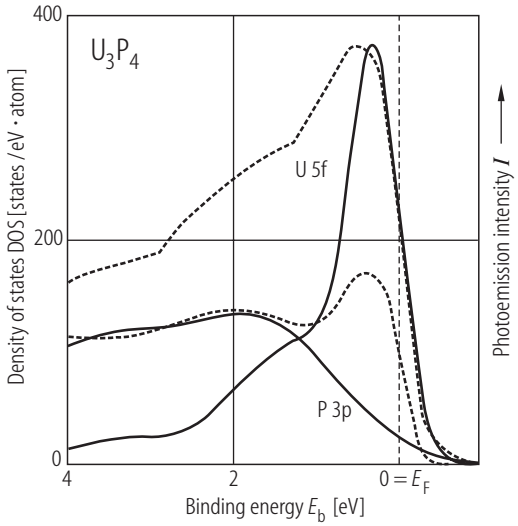

Fig. 50. U_3P_4. DOS calculated using LSDF theory and ASW method with incorporated spin-orbit coupling [96SK]. For comparison there are shown the experimental photoemission spectra taken from [85SYSM] (dashed curves). Lower curve: spectrum measured at photon energy 32 eV; upper curve: spectrum measured at photon energy 70 eV. The peak at about 0.5 eV below E_F is due to the U 5f states. The broad structure around 2 eV originates from the P 3p states (compare Fig. 67**)**. Note a good agreement between the theoretical and experimental results.

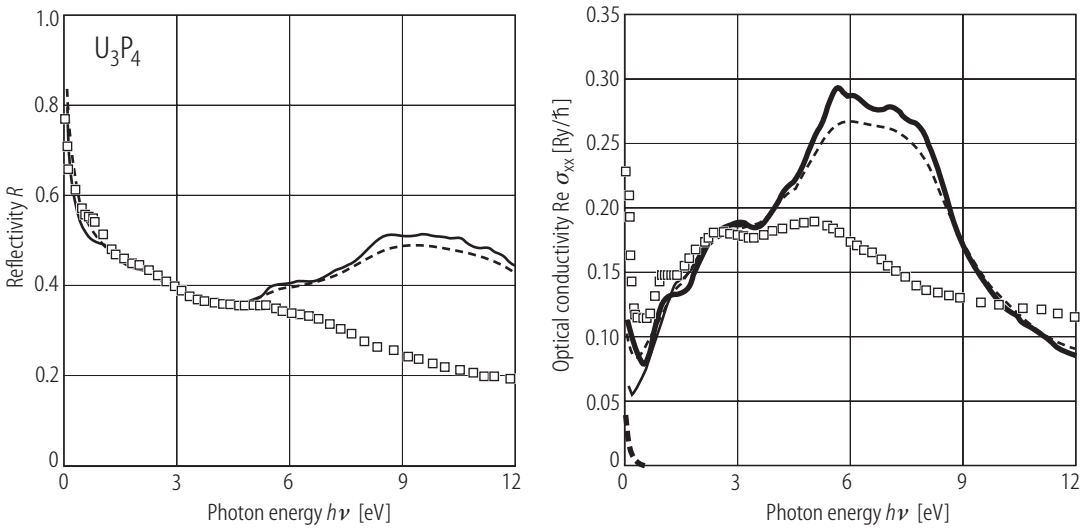

Fig. 51. U_3P_4. Normal incidence reflectivity, R (left panel), and real diagonal optical conductivity, Re σ_{xx} (right panel), vs. photon energy, $h\nu$, up to 12 eV, calculated by LDFT using ASW method generalized to the case of noncollinear magnetic structures and including the spin-orbit coupling and the effective orbital field corrections [98KSK]. Two values for the lifetime broadening parameter were assumed: δ = 0.01 Ry (thin solid lines) and 0.03 Ry (thin dashed lines). For comparison the experimental data taken from [83SKHH] (see Fig. 18**)** are shown by the squares. The bold solid curve is the calculated intraband contribution to Re σ_{xx} and the bold dashed line is the conductivity derived neglecting orbital polarization enhancement OPE. Note a good agreement between the calculated and experimental results for energies below ca. 4 eV being in favor of the itinerant electron model for U 5f electrons (see Fig. 21**)**. The difference seen for higher energies are attributed to the approximations in the theoretical approach and some uncertainties in the experiment due to insufficient quality of the sample surface. The calculated plasma frequency is 0.72 eV and thus the intraband contribution to the optical conductivity is sizable only for energies lower than 0.3 eV. Note that OPE term does not influence the Re σ_{xx} data substantially.

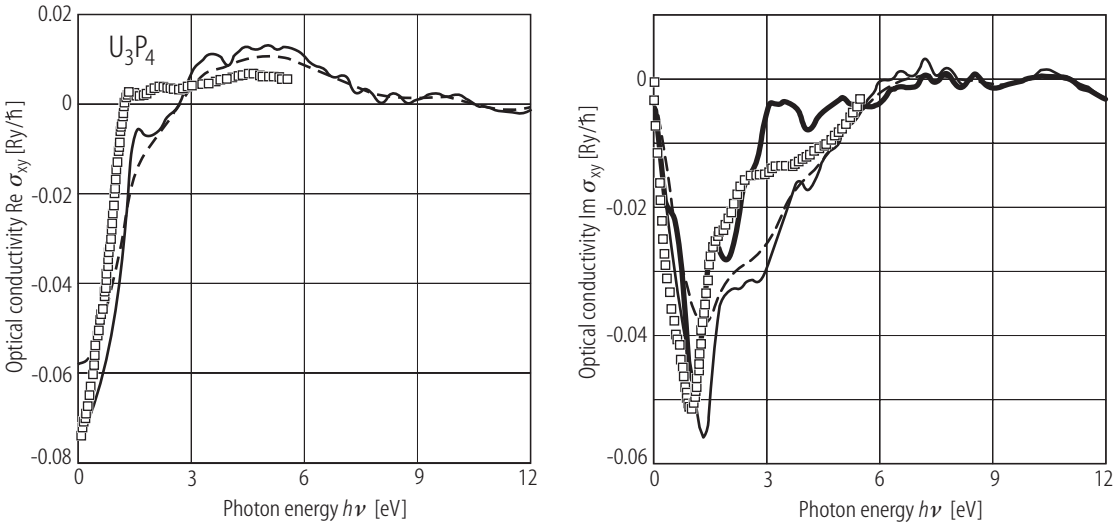

Fig. 52. U_3P_4. Real and imaginary parts of the off-diagonal optical conductivity, Re σ_{xy} (left panel) and Im σ_{xy} (right panel), vs. photon energy, $h\nu$, up to 12 eV, calculated as in Fig. 51 [98KSK]. For comparison the experimental data taken from [86R] (see Fig. 58**)** are shown, represented by the squares. The bold solid curve stands for Im σ_{xy} calculated neglecting orbital polarization enhancement OPE. The agreement between the experimental and theoretical results is quite good, especially in the low-energy region. Note that the calculation performed without the OPE term yields a better description of the experimental data.

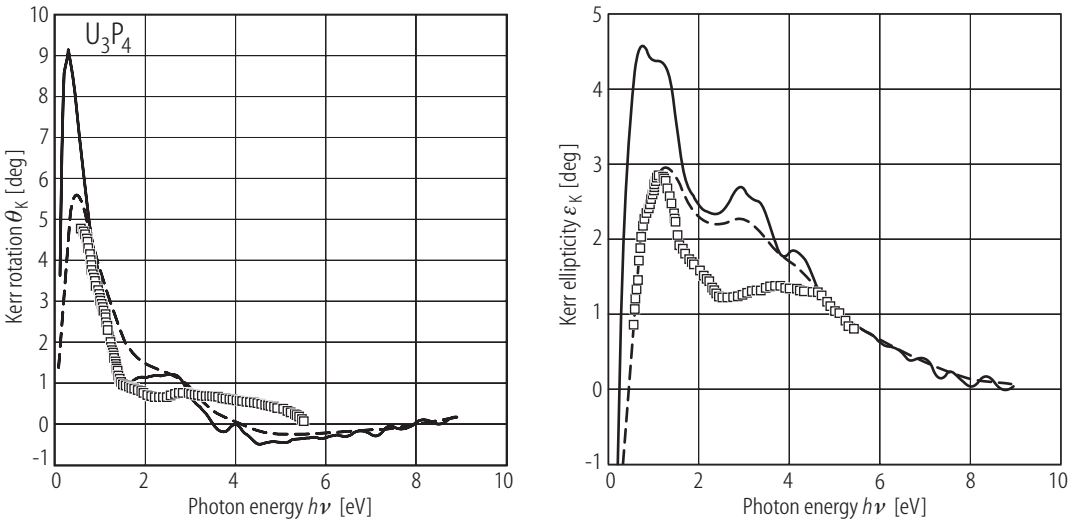

Fig. 53. U_3P_4. Kerr ellipticity, ε_K (right panel), and Kerr rotation, θ_K (left panel), vs. photon energy, $h\nu$, up to 9 eV, calculated as in Fig. 51 [98KSK]. For comparison the experimental data taken from [86R] (see Fig. 60**)** are shown, represented by the squares. The agreement between the experimental and theoretical results is fairly good, especially for θ_K ($h\nu$) where the prominent peak at about 1 eV is well reproduced with the lifetime broadening parameter δ = 0.03 Ry. This finding supports a picture of itinerant 5f electrons in U_3P_4.

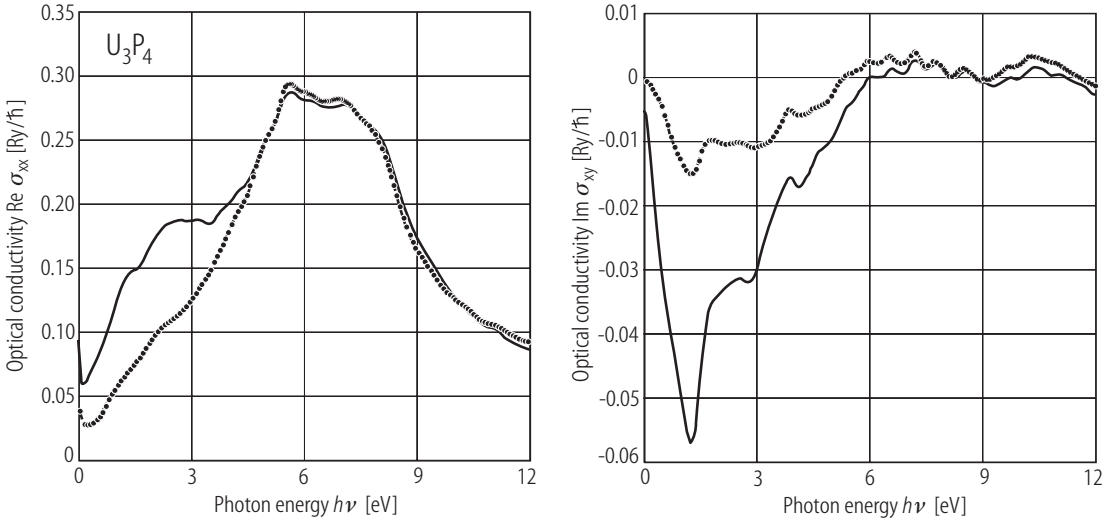

Fig. 54. U_3P_4. Real part of the diagonal optical conductivity, Re σ_{xx} (left panel), and imaginary part of the off-diagonal conductivity, Im σ_{xy} (right panel), vs. photon energy, $h\nu$, up to 12 eV, calculated as in Fig. 51 with (solid curves) and without (dotted curves) the U 5f-electrons contribution [98KSK]. The large differences seen below 5 eV emphasize the role of the U 5f states in determining the optical properties in this energy region.

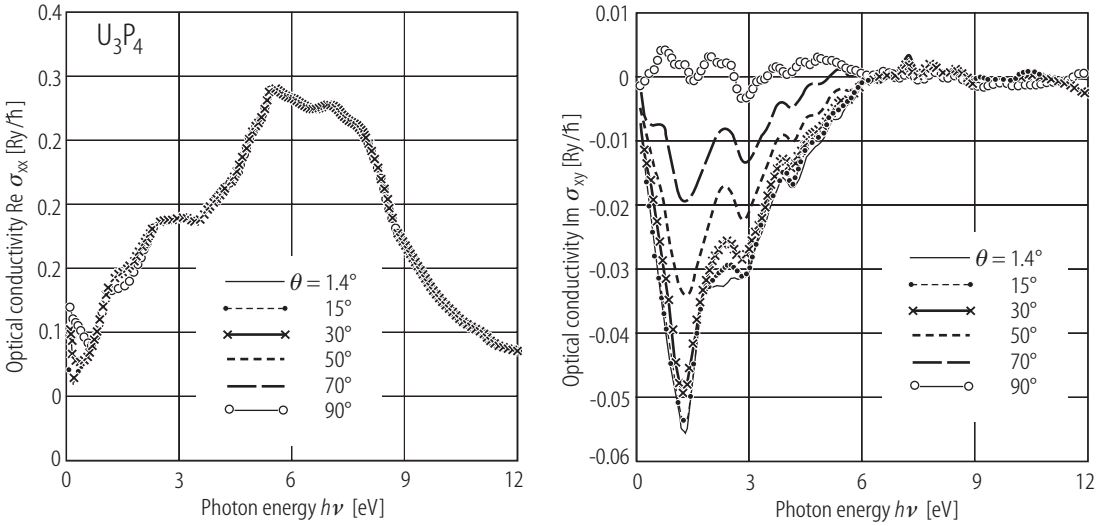

Fig. 55. U_3P_4. Real part of the diagonal optical conductivity, Re σ_{xx} (left panel), and imaginary part of the off-diagonal conductivity, Im σ_{xy} (right panel), vs. photon energy, $h\nu$, up to 12 eV, calculated as in Fig. 51 for several values of the canting angle, θ, of the magnetic moments in the noncollinear magnetic structure [98KSK]. The diagonal conductivity is almost independent of the noncollinearity but the off-diagonal conductivity monotonically decreases with increasing θ. This finding is considered to be an indication of the formation in U_3P_4 of well-defined magnetic moments formed by itinerant 5f electrons. For detailed discussion see the original paper and [97KSK2].

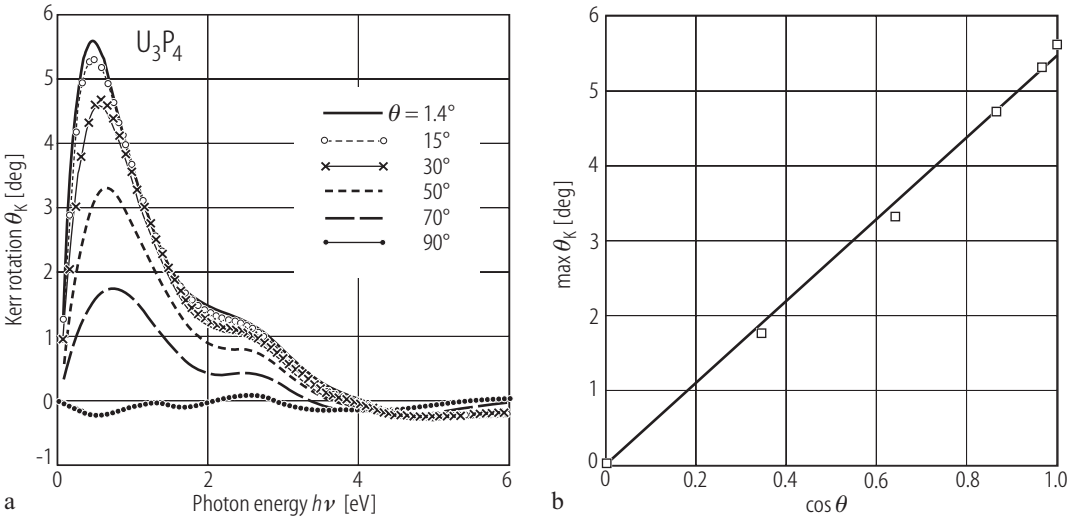

Fig. 56. U_3P_4. **(a)** Kerr rotation, θ_K, vs. photon energy, $h\nu$, calculated as in Fig. 51 for several values of the canting angle, θ, of the magnetic moments in the noncollinear magnetic structure [98KSK]. **(b)** Peak value of the theoretical Kerr angle, max θ_K, vs. cosinus of the non-collinearity angle, cos θ [98KSK]. The Kerr rotation perfectly scales with the cos θ law of the macroscopic magnetization (projection of the magnetic moment onto the [111] axis). Any change of the optical response with angle is so small (negligible) so that it is not possible to determine the actual canting angle from the theoretical approach.

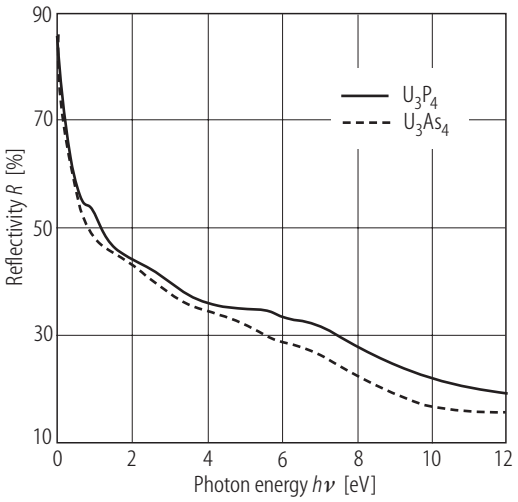

Fig. 57. U_3X_4, X = P, As, sc. Near normal incidence reflectivity, R, vs. photon energy, $h\nu$, from 0.03 to 12 eV taken at room temperature on polished samples [83SKHH]. Solid curve: U_3P_4; dashed curve: U_3As_4. In contrast to Th_3X_4 (compare Fig. 18**)** both compounds exhibit a metallic behavior.

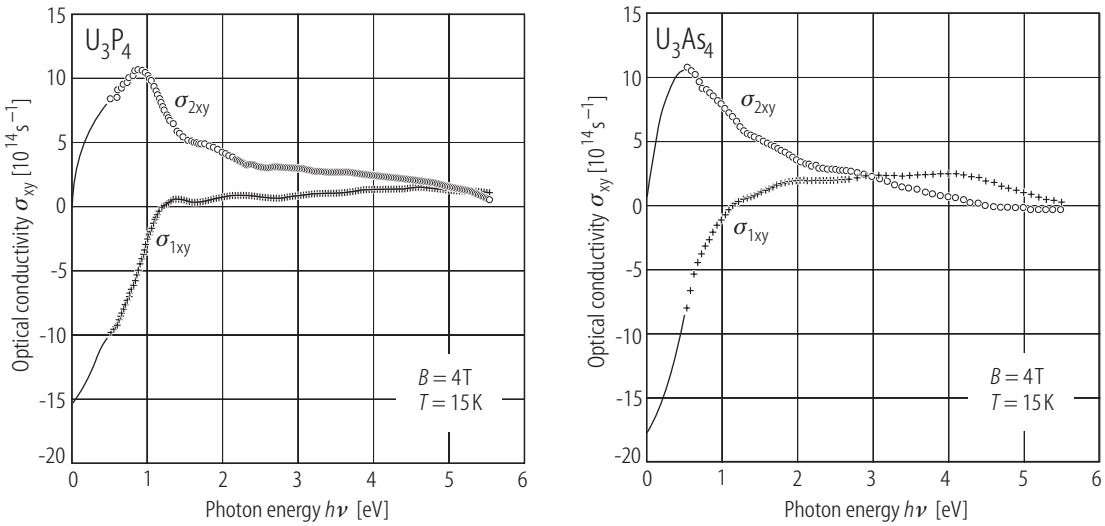

Fig. 58. U_3X_4, X = P, As, sc. Off-diagonal conductivity, σ_{1xy} (crosses) and σ_{2xy} (circles), vs. photon energy, $h\nu$, at magnetic saturation (B = 4 T, T = 15 K), calculated from the polar Kerr rotation data (see Fig. 60**)** and the optical data (see Fig. 22**)** [86R]. The low-energy extrapolation (solid curves) were derived by Kramers-Kronig inversion. The absorptive part of the off-diagonal conductivity decreases for both compounds as ω^{-1} indicating a dominant conduction band contribution. The extrapolation to $h\nu = 0$ gives values $\sigma_{1xy}(0)$ of the order of $-15 \cdot 10^{14}$ s^{-1} and of $-18 \cdot 10^{14}$ s^{-1} for U_3P_4 and U_3As_4, respectively, while the ratio $\sigma_{1xy}(0)/\sigma_{1xx}(0)$ is 1/2.9 and 1/1.8, respectively. These results agree well with the Hall effect data by [72H] and therefore it is concluded that the magnetooptical spectrum for the two compounds is determined only by intraband contribution. The sign of $\sigma_{1xy}(0)$ implies a negative charge carrier spin polarization (almost –100%) in respect to the 5f-moment. The unscreened plasma frequencies correspond to 4.7 and 4 eV for U_3P_4 and U_3As_4, respectively, which correspond to 0.75 and 0.6 charge carriers per U atom, respectively.

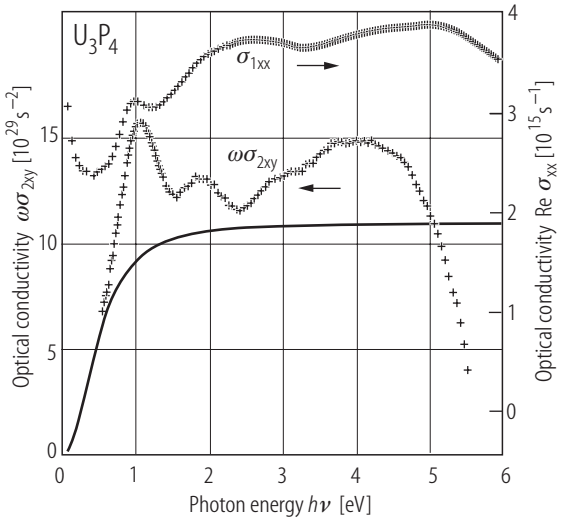

Fig. 59. U_3P_4, sc. Off-diagonal conductivity in the representation $\omega\sigma_{2xy}$ (left-hand side scale), and the absorptive diagonal conductivity, σ_{1xx} (right-hand side scale), vs. photon energy, $h\nu$, at magnetic saturation (B = 4 T, T = 15 K) [86R]. The solid line represents the pure intraband contribution as derived from the experimental $\sigma_{2xy}(h\nu)$ data (see Fig. 58**)**. The structures in $\omega\sigma_{2xy}$ above this line are due to interband contribution. Note that each of them has its counterpart in σ_{1xx} and thus they are assigned to p excitations into the crystal field split U 6d band (compare Fig. 22**)**. No f→d transitions are observed unless they are energetically degenerated with the p→d transitions.

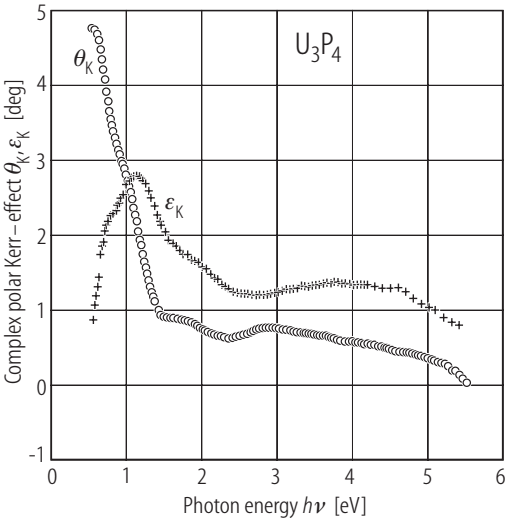

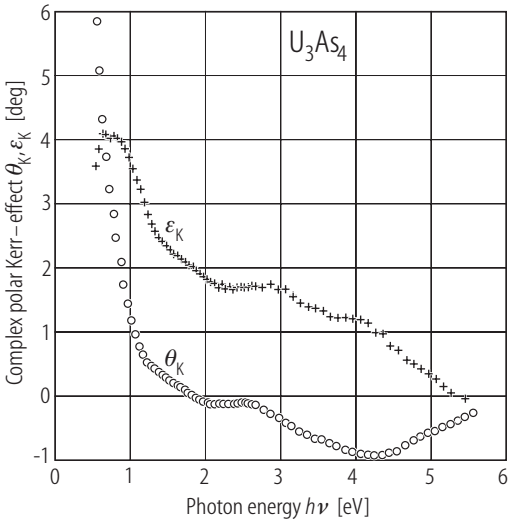

Fig. 60. U_3X_4, X = P, As, sc. Polar Kerr rotation, θ_K (circles), and ellipticity, ε_K (crosses), vs. photon energy, $h\nu$, in the range 0.5…5.5 eV measured for (112) polished samples at magnetic saturation (B = 4 T, T = 15 K) [86R]. Note a very large gradient of θ_K at low energies, yielding a large θ_K value of about 5° and 6° for U_3P_4 (left-hand side panel) and U_3As_4 (right-hand side panel), respectively. Above ca. 1.5 eV, for both compounds $\theta_K(h\nu)$ shows a rather flat behaviour. See Fig. 53 for comparison with the theoretical results for U_3P_4.

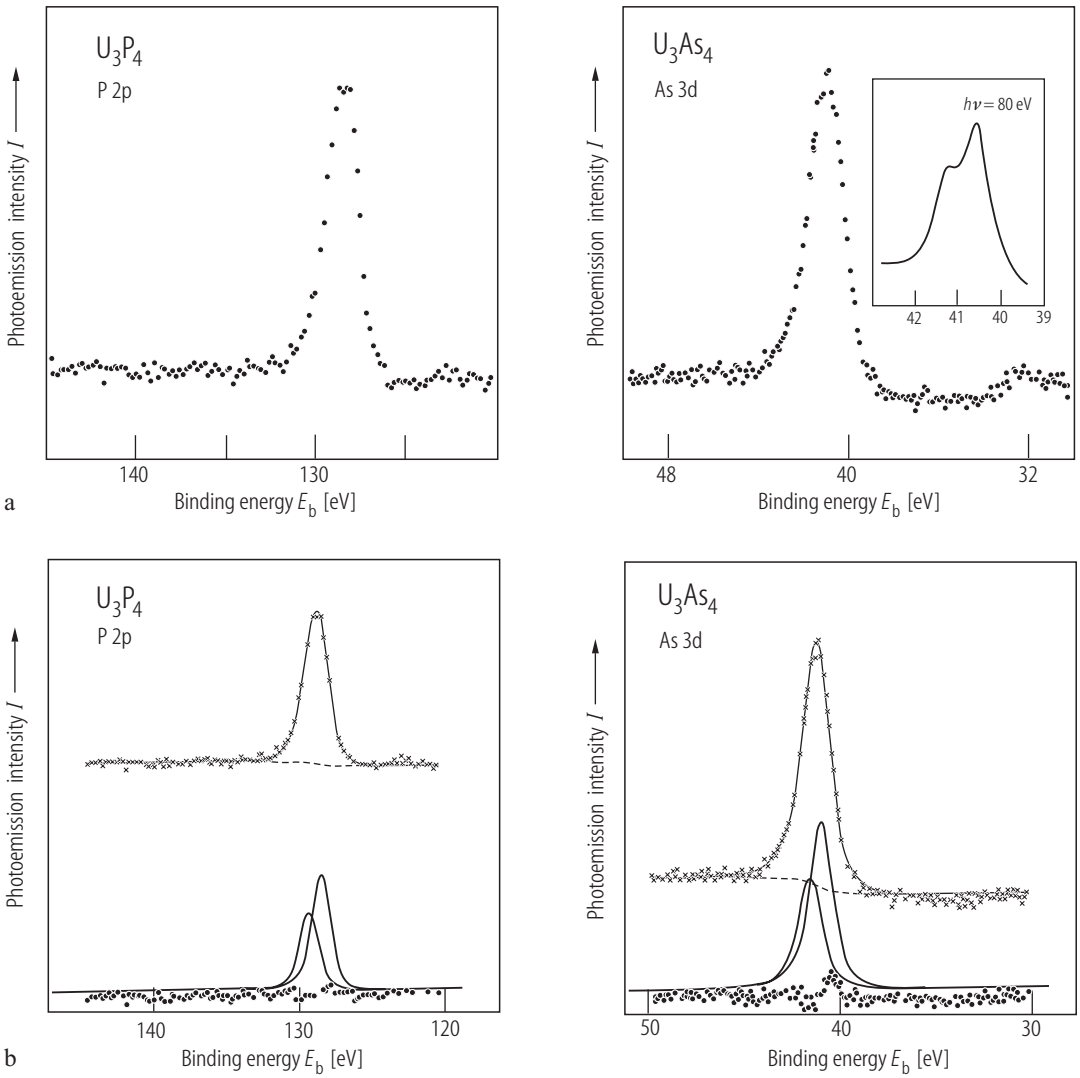

Fig. 61. U_3X_4, X = P, As, sc. **(a)** XPS spectra of P 2p (left panel) and As 3d (right panel) states [97SHMS]. Inset: UPS As 3d spectrum of U_3As_4 measured at $h\nu = 80$ eV, showing the spin-orbit splitting into $3d_{5/2}$ and $3d_{3/2}$ components. In contrast to the U-derived core level spectra (see Figs. 62 and 64), both pnictogen core spectra are rather symmetric thus confirming that the peak asymmetry is unique to the U states. **(b)** Deconvolution of the P 2p XPS spectrum of U_3P_4 (left panel) and the As 3d XPS spectrum of U_3As_4 (right panel) [97SHMS]. The two Lorenzian curves at the bottom represent the $3d_{3/2}$ and $3d_{5/2}$ components, with the intensity ratio 2:3. The spin-orbit splitting is estimated to be about 0.85 and 0.7 eV in U_3P_4 and U_3As_4, respectively. The dashed lines denote the integral background. The curves through the data points are the sum of the spin-orbit components and the background.

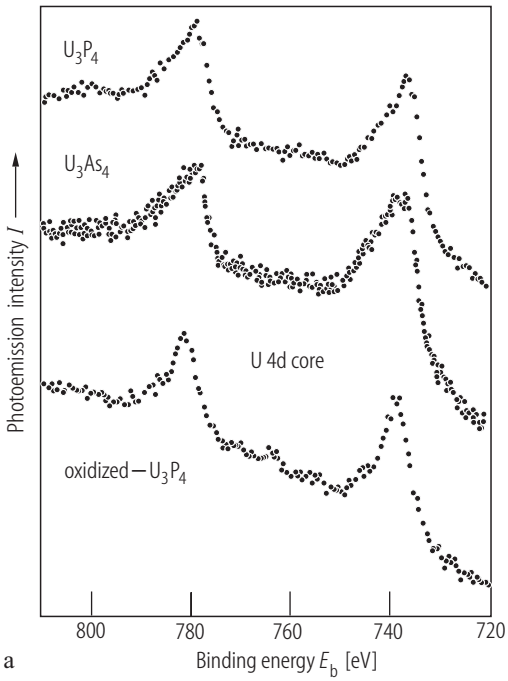

a

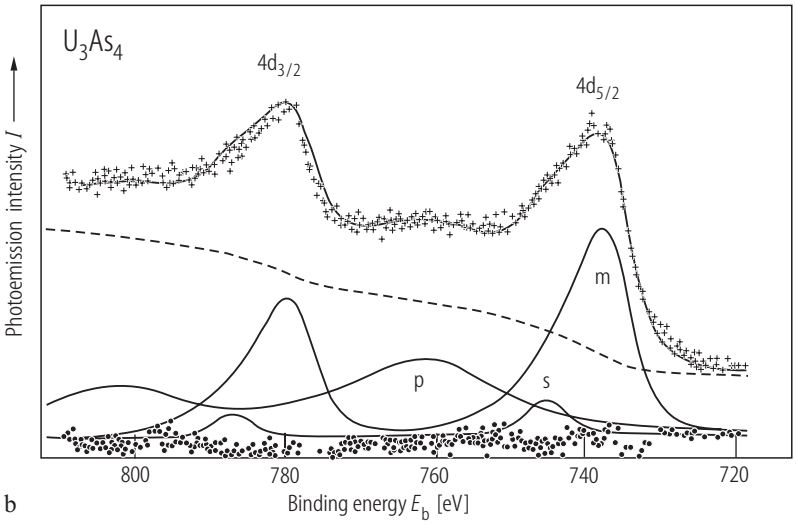

b

Fig. 62. U_3X_4, X = P, As, sc. **(a)** XPS spectra of U 4d core states [97SHMS]. For comparison the U 4d spectrum of oxidized U_3P_4 is shown. Note that the $4d_{5/2}$ and $4d_{3/2}$ main peaks at the binding energies E_b of 737 and 778 eV, respectively, for the clean samples show rather broad lineshapes with appreciable asymmetry, in contrast to narrower and symmetric main peaks at E_b of 740 and 780 eV, respectively, observed for the oxidized sample. Because of extended character of the U 5f wave functions the multiplet structures were found to be negligible for both the $4d_{5/2}$ and $4d_{3/2}$ core photoemission structures. Any clear U 5f-X p antibonding peak is also not expected in the 4d XPS spectrum owing to the small effective correlation energy $U_{5f,5f}$ of 1.2 eV established in the UPS studies (see Fig. 66**)**. Hence, the effect observed was attributed to the presence of a satellite resulting from the U 6d-X p antibonding state (see panel **(b)**). A part of the asymmetry may also be due to the orthogonality catastrophe caused by the high density of U 6d states near E_F (see Fig. 68**)**. In line with this interpretation the U 4d spectrum in oxidized U_3P_4 does not show peak asymmetry as in this case the U 6d band does not cross E_F. **(b)** Deconvolution of the U 4d core XPS spectrum of U_3As_4 [97SHMS]. The three curves at the bottom represent the components of the main peak (m), satellite (s) and energy loss peak (p). The monotonously rising curve in the middle of the panel is the integral background. The curve through the data points is the sum of the three components and the background. For the details see the original paper.

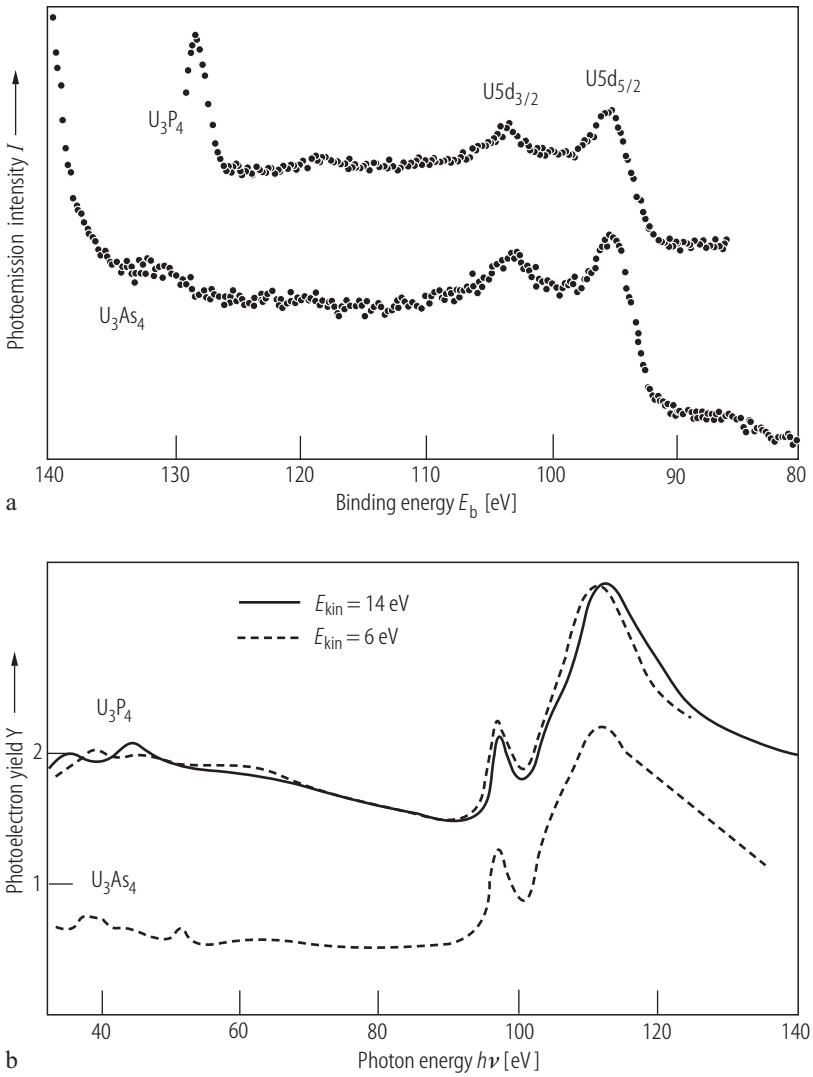

Fig. 63. U_3X_4, X = P, As, sc. **(a)** XPS spectra of U 5d states [97SHMS]. The structures near 94 and 103 eV binding energy are assigned to the $5d_{5/2}$ and $5d_{3/2}$ states. **(b)** Constant final state (CFS) spectra taken for the electron kinetic energy E_{kin} of 6 eV (dashed line) and 14 eV (solid line) [97SHMS]. The structures in the 90…135 eV region represent the core absorption spectra (XAS). In the region 30…80 eV some direct excitation of photoelectrons into the detector window at E_{kin} was observed. The XAS peaks at $h\nu = 97.4$ and 112.5 eV as well as the hump at $h\nu = 104.5$ eV are due to the U 5d core states. Note that their energy positions are slightly larger than E_b of the corresponding XPS peaks (compare panel **(a)**).

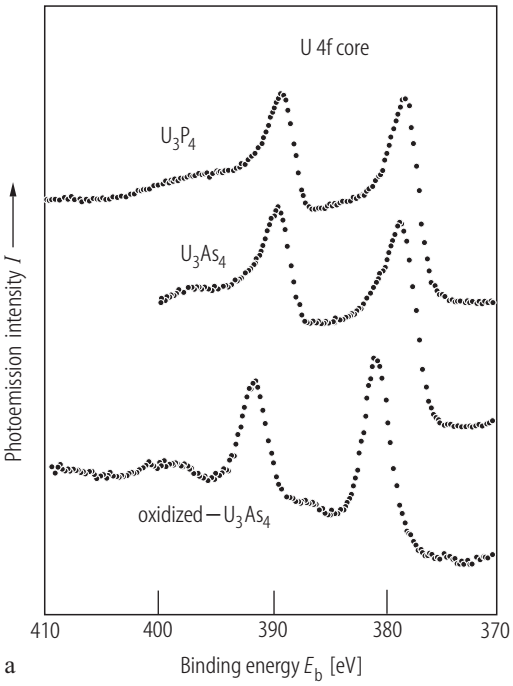

a

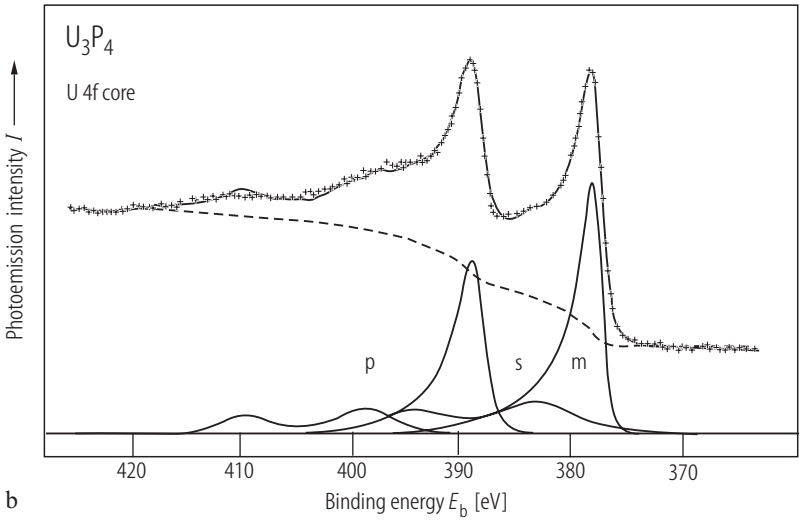

b

Fig. 64. U_3X_4, X = P, As, sc. **(a)** XPS spectra of U 4f core states [95SMIO]. For comparison the U 4f spectrum of oxidized U_3As_4 is also shown. The sharp peaks at the binding energies E_b of 378 and 389 eV are ascribed to the U $4f_{5/2}$ and $4f_{7/2}$ states. The two broad humps around 397 and 410 eV (hardly seen) are attributed to intrinsic energy loss (plasmon) satellites. Note that the main peaks for the clean samples are rather broad and asymmetric, as clearly recognized when compared with the oxidized sample, for which the relatively narrow and symmetric main peaks are shifted to larger E_b by 2.5 eV and the 7 eV satellites emerge at the higher binding energy side. **(b)** Deconvolution of the U 4f core XPS spectrum of U_3P_4 [95SMIO]. The three curves at the bottom represent the components of the main peak (m), satellite (s) and energy loss peak (p). The rising curve in the middle of the panel is the integral background. The curve through the data points is the sum of the three components and the background. The satellites arise due to the p-d antibonding state induced by the U 4f-U 6d Coulomb interactions and U 6d-X p hybridization. The intensity ratio of this satellite to the main peak is about 30%. For further details see the original paper.

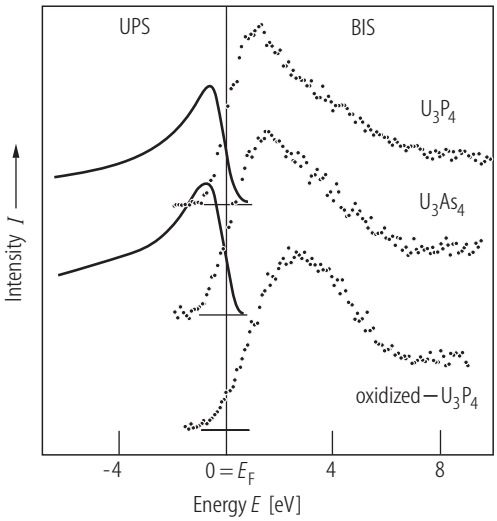

Fig. 65. U_3X_4, X = P, As, sc. BIS spectra taken at 130 K (points) and UPS spectra measured at room temperature with the excitation photon energy $h\nu$ = 104 eV (solid curves) [95SMIO]. For comparison the BIS spectrum of oxidized U_3P_4 is shown. For clean surfaces, a prominent, anomalously broad peak occurs around 1.8 eV above E_F and large intensity is seen at E_F. For the oxidized sample, the BIS peak is less symmetric and located around 3 eV above E_F with the intensity at E_F being strongly reduced. The main contribution to the BIS peak originates from the U 4f electrons in the j = 7/2 state. The broad line shape of the BIS feature is supposed to be caused by dynamical relaxation of the conduction electrons, responding to the introduced BIS electron. The energy separation of the BIS peak and the U 5f UPS peak is 2.5 eV for both compounds, which is much larger than the established effective correlation energy $U_{5f,5f}$ of 1.2 eV (see Fig. 66**)**. Hence, a large part of this energy difference (2.5 – 1.2 = 1.3 eV) can be accounted for by the spin-orbit splitting energy of about 0.8 eV (see Fig. 61**)**.

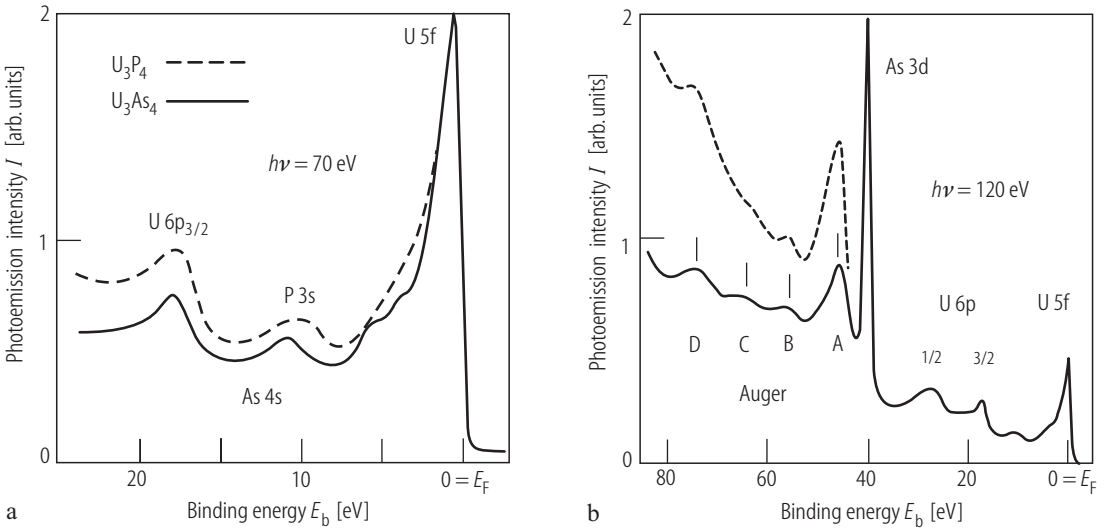

Fig. 66. U_3X_4, X = P, As, sc. Synchrotron radiation UPS spectra taken at room temperature on clean surfaces cleaved in ultrahigh vacuum at the excitation photon energy $h\nu$ = 70 eV **(a)** and 120 eV **(b)**, with the total resolution better than 0.8 eV [85SYSM]. Dashed curves: U_3P_4; solid curves: U_3As_4. The structures occurring in the low binding energy region (see **(a)**) are ascribable to U 5f, P 3s or As 4s and U $6p_{3/2}$ states. On further increasing E_b, U $6p_{1/2}$, As 3d and Auger emission structures are observed (see **(b)**). The features A, B, C, and D are ascribed to $5d_{5/2}5f6p_{3/2}$, $5d_{5/2}5f6d_{1/2}$, $5d_{5/2}6p_{3/2}6p_{3/2}$ and $5d_{5/2}6p_{3/2}6p_{1/2}$ Auger transitions associated with the U 5d core hole state, respectively, with the effective hole-hole correlation energies of 2.7, 3.8, 3.5 and 4.7 eV, respectively. The effective correlation energy $U_{5f,5f}$ is evaluated as 1.2 eV. Such a small value of $U_{5f,5f}$ is consistent with the extended character of the U 5f state and the effective screening effect by the U 6d electrons.

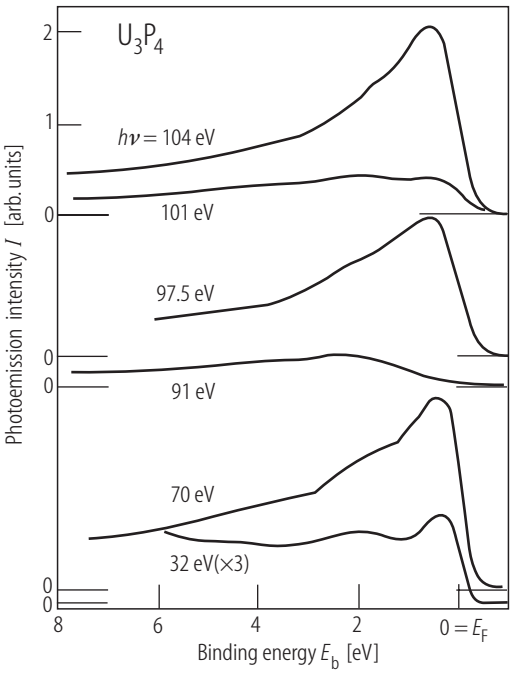

Fig. 67. U_3P_4, sc. UPS spectra taken at various excitation photon energies $h\nu$ at room temperature on clean surfaces cleaved in ultrahigh vacuum [85SYSM]. Note an oscillatory behaviour of the photoemission intensity of the prominent peak as $h\nu$ crosses the threshold energies of the U 6d→5f excitation, indicating its clear 5f character. The structure at E_b = 2 eV is due to the P 3p states hybridized with U 5f states.

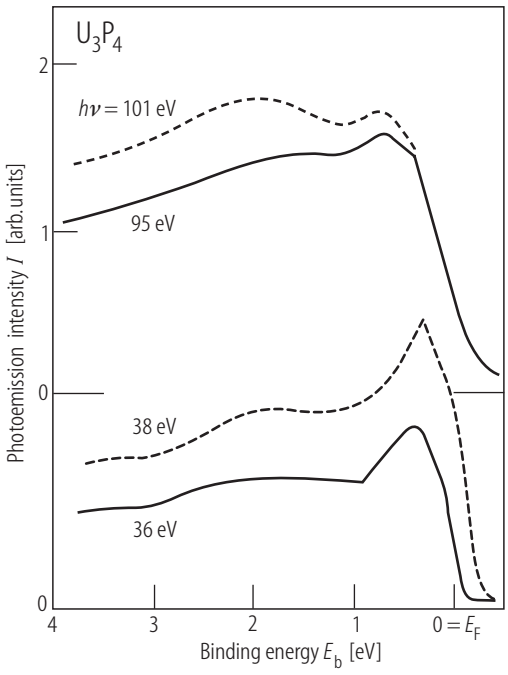

Fig. 68. U_3P_4, sc. High resolution UPS spectra taken at various excitation photon energies $h\nu$ [85SYSM]. The broad structure around 2 eV is a p-f hybridized state (see also Fig. 67**)**. The sharp peak seen at E_b = 0.3…0.4 eV in the spectra measured at $h\nu$ = 36 and 38 eV, and observed at E_b = 0.71 eV in the $h\nu$ = 95 and 101 eV spectra is mainly due to the 6d conduction band, which is expected to start from the energy about 1 eV below E_F (see Fig. 23**)**. This 6d band is mixed with the U 5f states (compare Fig. 65**)** resulting in a strong 5f character of the high density of states at E_F.

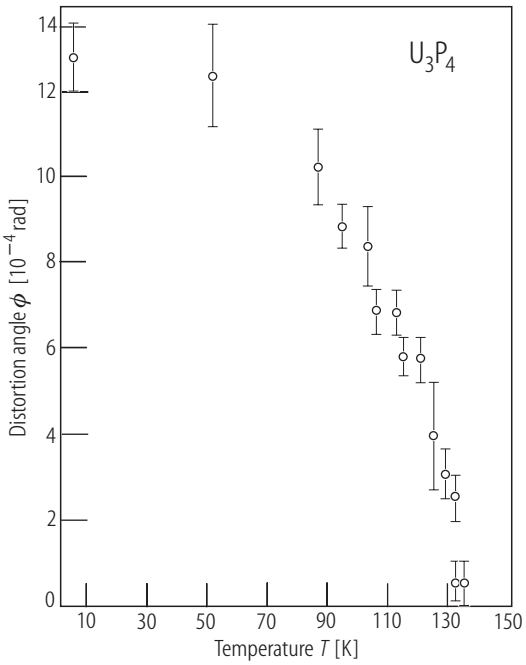

Fig. 69. U_3P_4, sc. Rhombohedral distortion angle, ϕ, vs. temperature, T, in the ferromagnetic region [75SWS]. ϕ is the difference between the rhombohedral angle α and the cubic angle 90°. The compound is cubic (Th_3P_4-type) above the Curie temperature of T_C = 138 K and undergoes a very small rhombohedral distortion at T_C yielding at 4.2 K an angle between cell edges of 89.92°.

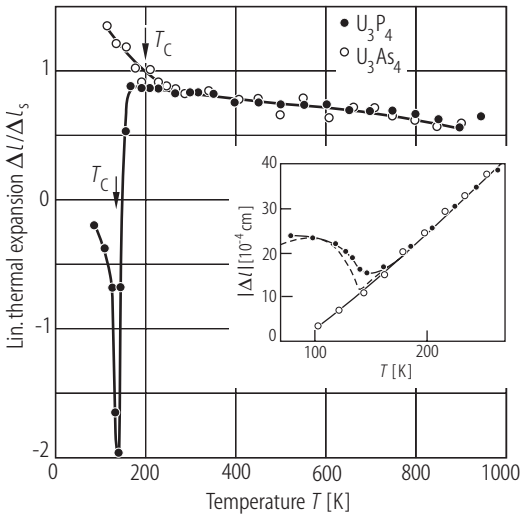

Fig. 70. U_3X_4, X = P, As. Relative linear thermal expansion, $\Delta l/\Delta l_s$, vs. temperature in the range 77…900 K [71HB]. Full circles: U_3P_4; open circles: U_3As_4. Δl_s is the linear thermal expansion of the standard. The arrows mark the Curie temperatures. In the paramagnetic state the linear expansion coefficient is nearly the same for both compounds but in the ordered region it goes through a sharp negative minimum at T_C in U_3P_4 and is positive at all temperatures in U_3As_4. The difference in the behavior of the two compounds is caused by the presence of strong exchange striction in U_3P_4. Inset: linear thermal expansion Δl vs. T, compared to the equation $\Delta l \sim A\,[\sigma(T)/\sigma(0)]^2$, where σ is the magnetization in U_3P_4 (dashed line).

→

Fig. 71. U_3P_4. Crystal field energy levels scheme calculated in the Russell-Saunders coupling scheme within: **(a)** the point charge model for the cases U^{3+} and U^{4+} (see some correspondence in the wavefunctions marked in panel **(b)**) [80Z]; **(b)** the nearest-neighbours approximation for U^{4+} and several different values of the Sternheimer shielding factor σ_2 (σ_4 and σ_6 are close to zero) [86ABHM]. The crystal field parameters are listed in Table S. Full horizontal bars: singlets; dash-dotted horizontal bars: doublets: The small letters denote the following wavefunctions:

a - $\left|\Gamma_{t1}^{(1)}\right\rangle = \varepsilon\left(|4\rangle + \varepsilon\left|\bar{4}\right\rangle\right) + \gamma|0\rangle$,

b - $\left|\Gamma_{t1}^{(2)}\right\rangle = \frac{\gamma}{\sqrt{2}}\left(|4\rangle + \frac{\gamma}{\sqrt{2}}\left|\bar{4}\right\rangle\right) - \sqrt{2}\varepsilon|0\rangle$,

c - $\left|\Gamma_{t2}\right\rangle = \frac{1}{\sqrt{2}}|4\rangle - \frac{1}{\sqrt{2}}\left|\bar{4}\right\rangle$,

d - $\left|\Gamma_{t3}\right\rangle = \frac{1}{\sqrt{2}}|2\rangle + \frac{1}{\sqrt{2}}\left|\bar{2}\right\rangle$,

e - $\left|\Gamma_{t4}\right\rangle = \frac{1}{\sqrt{2}}|2\rangle - \frac{1}{\sqrt{2}}\left|\bar{2}\right\rangle$,

f - $\left|\Gamma_{t5}^{(1)}\right\rangle = \alpha|\pm 3\rangle + \beta|\mp 1\rangle$,

g - $\left|\Gamma_{t5}^{(2)}\right\rangle = \beta|\pm 3\rangle - \alpha|\mp 1\rangle$.

The arrow marks the CF level scheme calculated by [71TMS] for D_{2d} symmetry. For σ_2 being close to 0.9 (as also given earlier in [79ER]) the CF level scheme is suitable for the interpretation of the specific heat and the ordered moment value. For details see the original paper.

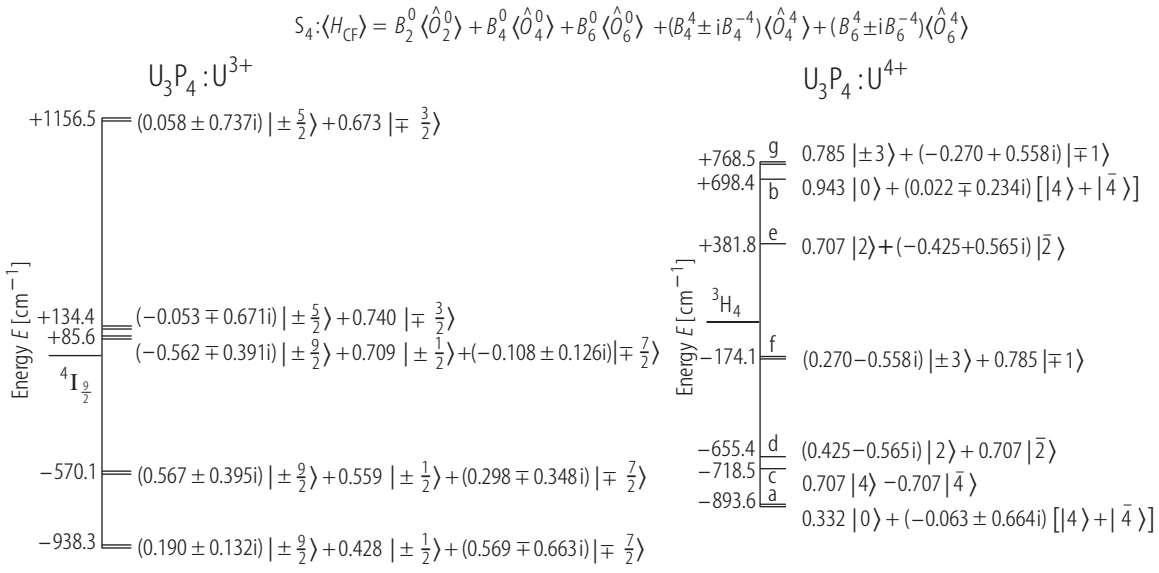

a

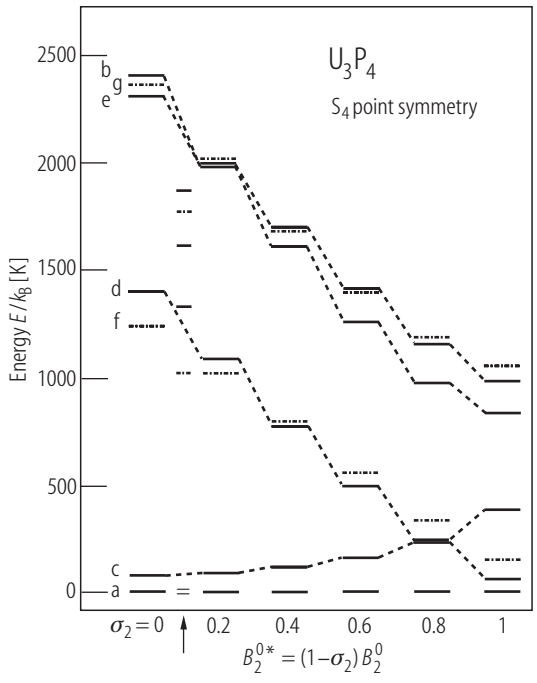

b

Fig. 71. For caption see previous page.

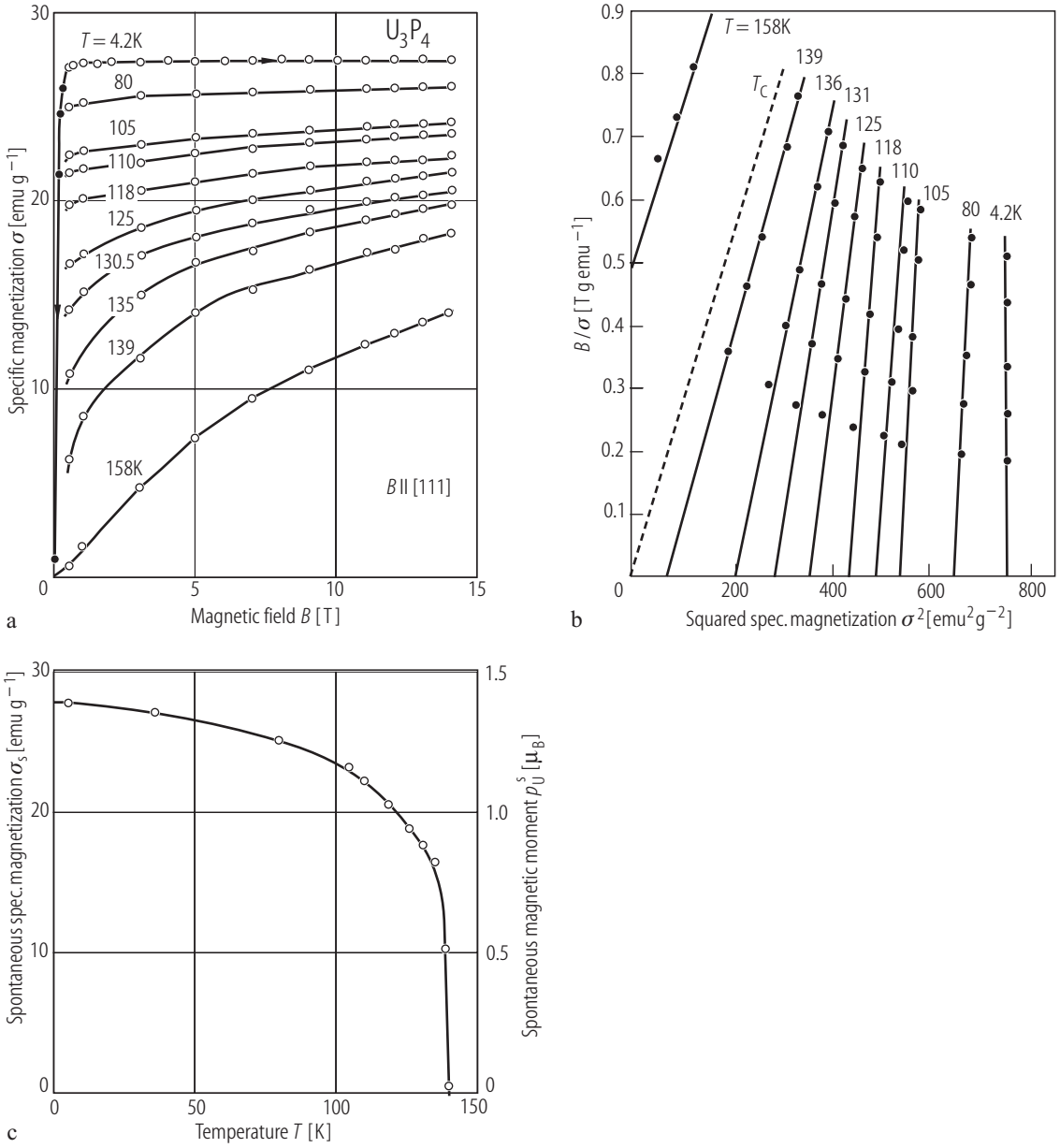

Fig. 72. U_3P_4, sc. **(a)** Specific magnetization, σ, vs. magnetic field, B, up to 14 T applied along the [111] axis, measured at different temperatures specified [81TM]. **(b)** Magnetization isotherms in the form of the Arrott's plot B/σ vs. σ^2 [81TM]. The measurement temperatures are specified in the figure, the magnetic field was applied along the [111] axis. The solid lines are linear extrapolations to $B/\sigma = 0$. The dashed line schematically represents a magnetization isotherm corresponding to T_C. **(c)** Spontaneous magnetization, σ_s, along the [111] easy axis, obtained by the extrapolations as in panel **(b)**, vs. temperature, T [81BRTH]. The symbols represent the experimental data derived by the Arrott's method. The solid curve serves as a guide for the eye. The spontaneous magnetic moment at 4.2 K is 1.39 μ_B.

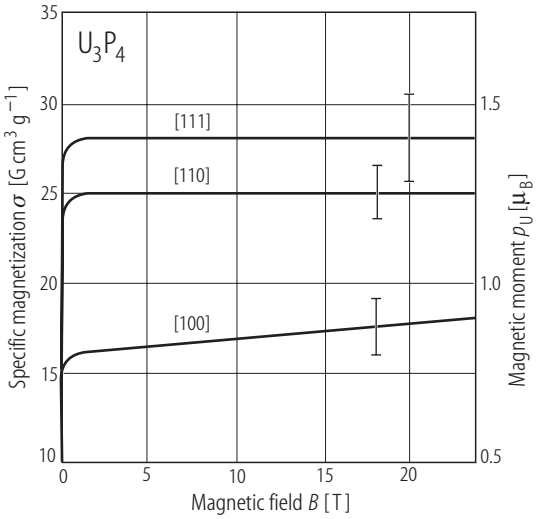

Fig. 73. U_3P_4, sc. Specific magnetization, σ, vs. pulsed magnetic field, B, up to 24 T taken at T = 78 K with B ∥ [111], B ∥ [110] and B ∥ [100] [71THBD]. The anisotropy field is of the order of 100 T.

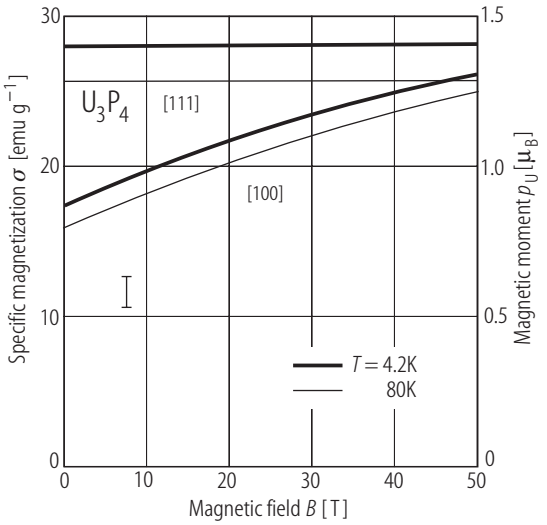

Fig. 74. U_3P_4, sc. Specific magnetization, σ, vs. magnetic field, B, up to 50 T taken at T = 4.2 K (thick lines) and 80 K (thin lines) with B ∥ [100] and B ∥ [111] [82GLLO]. The vertical bar represents the accuracy of measurement. The magnetization taken along the hard direction [100] monotonically increases with field and at 50 T reaches about 90% of the saturation value along the easy direction. Thus no jump of the magnetic moment is observed, in contrast to the behaviour of U_3As_4 (see Fig. 136) and U_3Sb_4 (see Fig. 193).

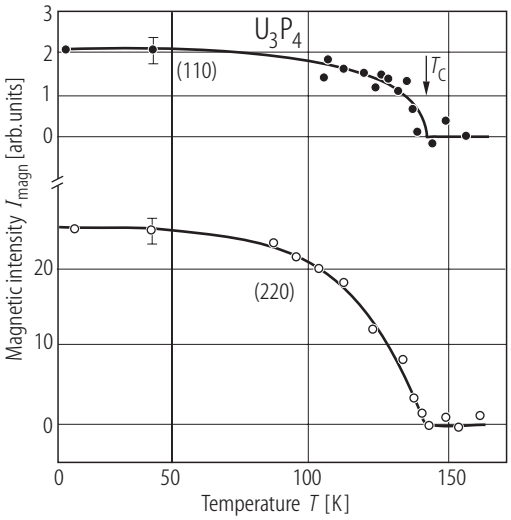

Fig. 75. U_3P_4, sc. Neutron diffraction intensity, I_{magn}, of a magnetic Bragg peak (220) and a superlattice peak (110) vs. temperature, T [81BRTH]. The ferromagnetic phase transition takes place at about 140 K into a non collinear three-axial structure (see Fig. 188). At 4.2 K the ordered moment amounts to 1.42(2) μ_B being in good agreement with the magnetization data (see Fig. 72**)**.

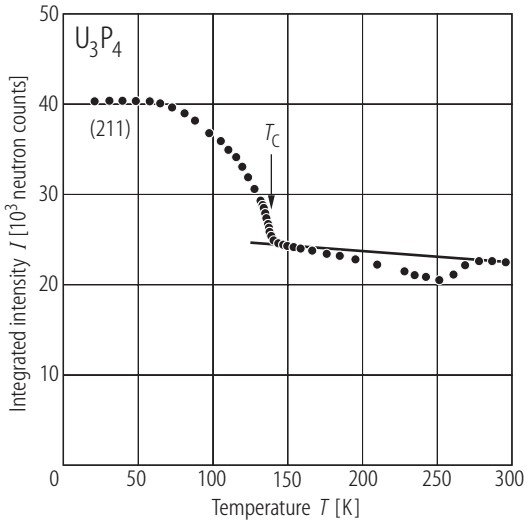

Fig. 76. U_3P_4, sc. Total (211) nuclear and magnetic integrated neutron diffraction intensity, I, vs. temperature, T [93SDKT]. The data, taken in a heating run, were corrected for diffuse background scattering. The solid line marks the nuclear contribution extrapolated from the regions 140…150 K and 280…300 K. A clear dip in $I(T)$ with a minimum at 250 K being fully repeatable in a number of runs is not explained. The arrow marks $T_C \approx 138$ K.

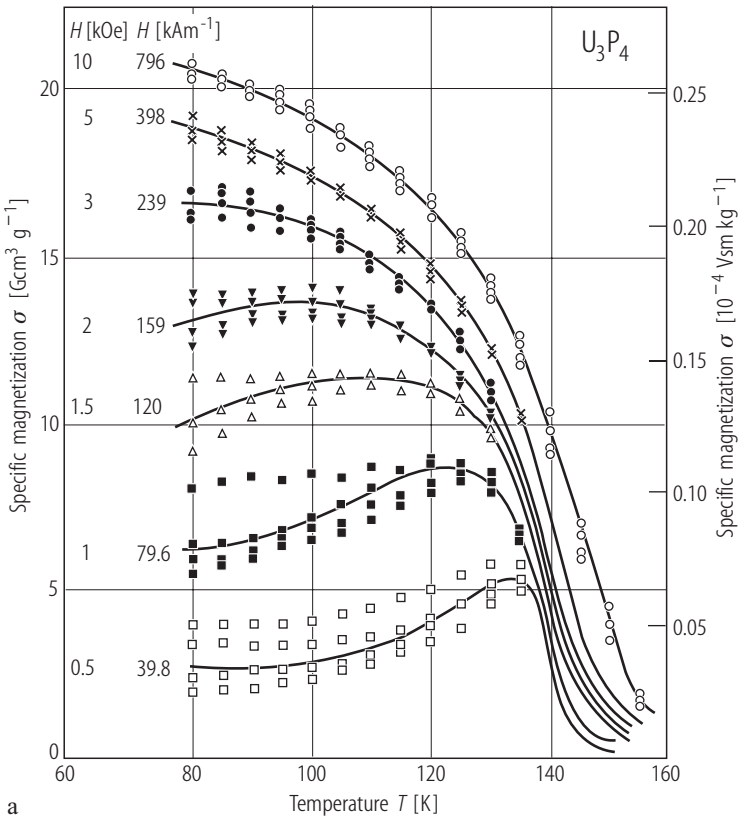

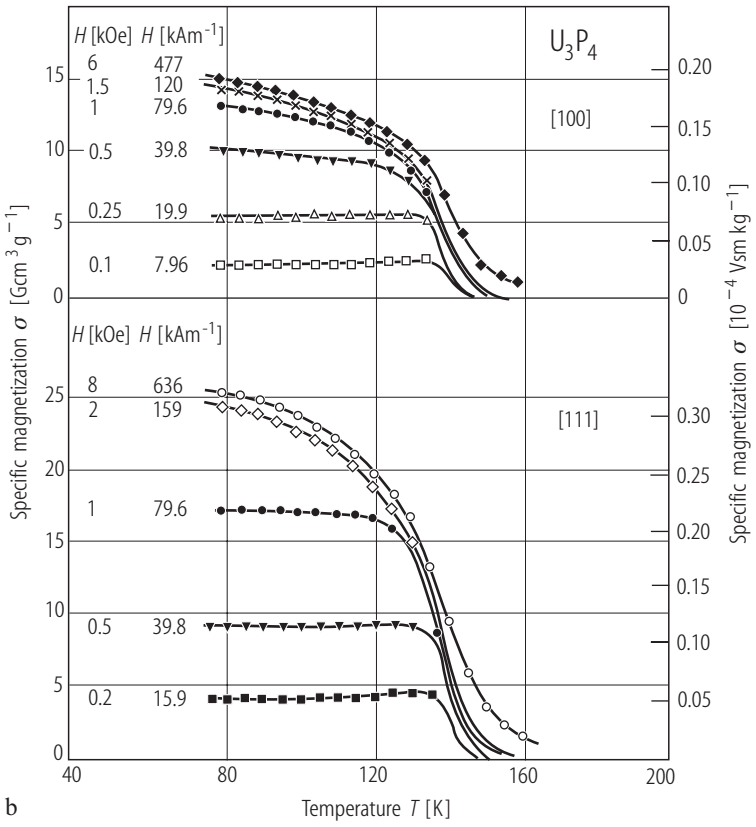

Fig. 77. U_3P_4. **(a)** Specific magnetization, σ, vs. temperature, T, in the range 80…150 K measured on four different powder samples in various magnetic fields upon cooling to 80 K in zero field [76SSSS]. Open squares: 0.05 T; full squares: 0.1 T; open triangles: 0.15 T; full triangles: 0.2 T; full circles: 0.3 T; crosses: 0.5 T; open circles: 1 T. Note the occurrence of maxima in $\sigma(T)$ taken in weak fields, which result from rotation processes of the spontaneous magnetization in single-domain grains of strongly anisotropic compound. **(b)** Specific magnetization, σ, vs. temperature, T, in the range 80…160 K measured in various magnetic fields oriented along the [100] hard direction (upper panel) and along the [111] easy direction (lower panel) [76SSSS]. The samples were cooled to 80 K without magnetic field. Open squares: 0.01 T; full squares: 0.02 T; open triangles: 0.025 T; full triangles: 0.05 T; full circles: 0.1 T; crosses: 0.15 T: open diamonds: 0.2 T; full diamonds: 0.6 T; open circles: 0.8 T. Note that σ is almost independent of T in fields lower than 0.1 T and there are no maxima in $\sigma(T)$, characteristic of powders (compare Fig. 77**(a)**). The observed behaviour may be attributed to the motion of Bloch walls in multi-domain sample of the strongly anisotropic system.

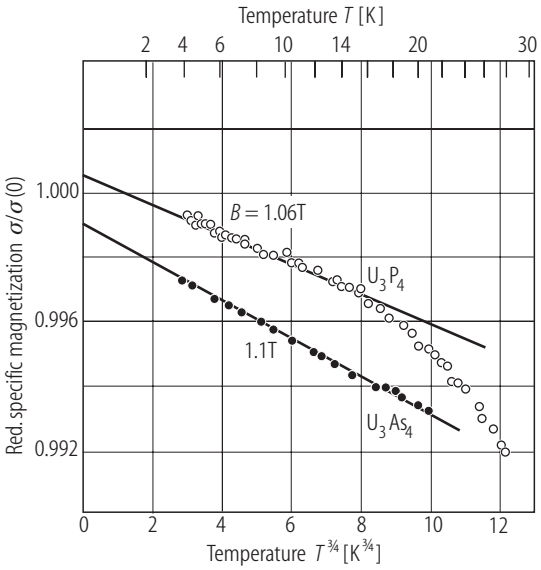

Fig. 78. U_3X_4, X = P, As, sc. Reduced specific magnetization, $\sigma/\sigma(0)$, vs. temperature, $T^{3/4}$, below 30 K, taken with magnetic field applied along the [111] axis [82MKTS]. Open circles: U_3P_4 in B = 1.06 T; full circles: U_3As_4 in B = 1.1 T. The solid straight lines mark a $T^{3/4}$ behaviour being predicted by no theory.

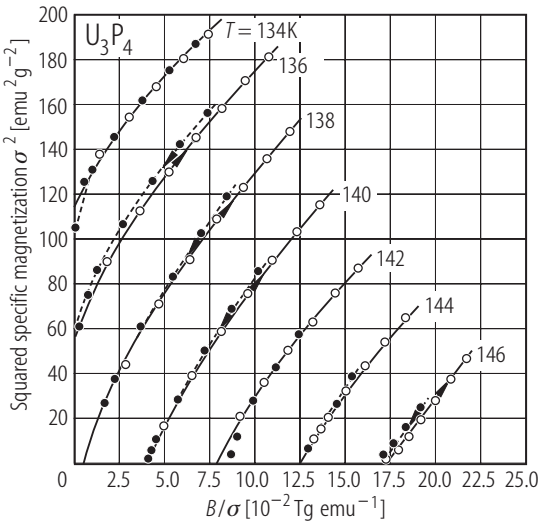

Fig. 80. U_3P_4, sc. Magnetization isotherms, σ^2, vs. B/σ measured at various temperatures near the Curie point with increasing (open circles) and decreasing (full circles) magnetic field, on samples freely placed in a sample holder [83TA]. Note that the isotherms deviate from a straight-line behaviour in low fields but in high fields they become straight lines with nearly the same slope. See the analysis of these data shown in Fig. 81.

For Fig. 79 see next page

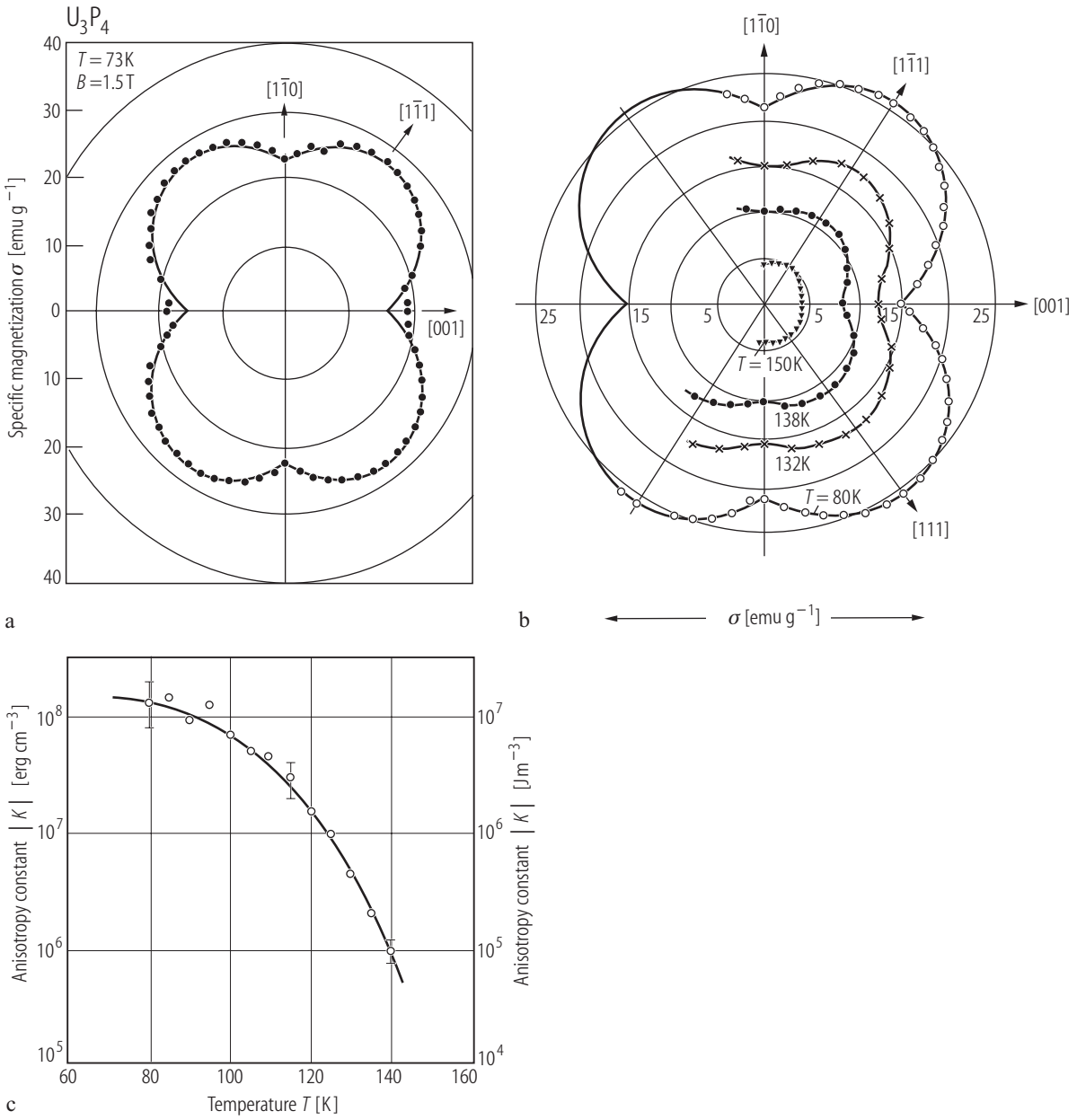

Fig. 79. U_3P_4, sc. **(a)** Angular variation of the specific magnetization, σ, measured within the (110) plane in a field of 1.5 T at T = 73 K [69B]. The uranium ordered magnetic moment along the easy direction [111] amounts to 1.41 μ_B. **(b)** Angular dependence of σ taken at T = 80, 132, 138 and 150 K [75SSSS]. **(c)** Anisotropy constant, K, (logarithmic scale) vs. temperature, T, in the range 78…140 K, derived from the magnetization data obtained in a field of 1.2 T applied along the [111] and [100] directions [75SSSS]. K is defined as $|K| = \dfrac{H\sigma_{[111]}d}{\dfrac{\sigma_{[100]}}{\sigma_{[111]}}\left[3\left(\dfrac{\sigma_{[100]}}{\sigma_{[111]}}\right)^2 - 1\right]}$ where d is the sample density. Note that due to the closeness of $\dfrac{\sigma_{[100]}}{\sigma_{[111]}}$ to $1/\sqrt{3}$ relatively large uncertainty in determining K is expected, especially at the lowest temperatures.

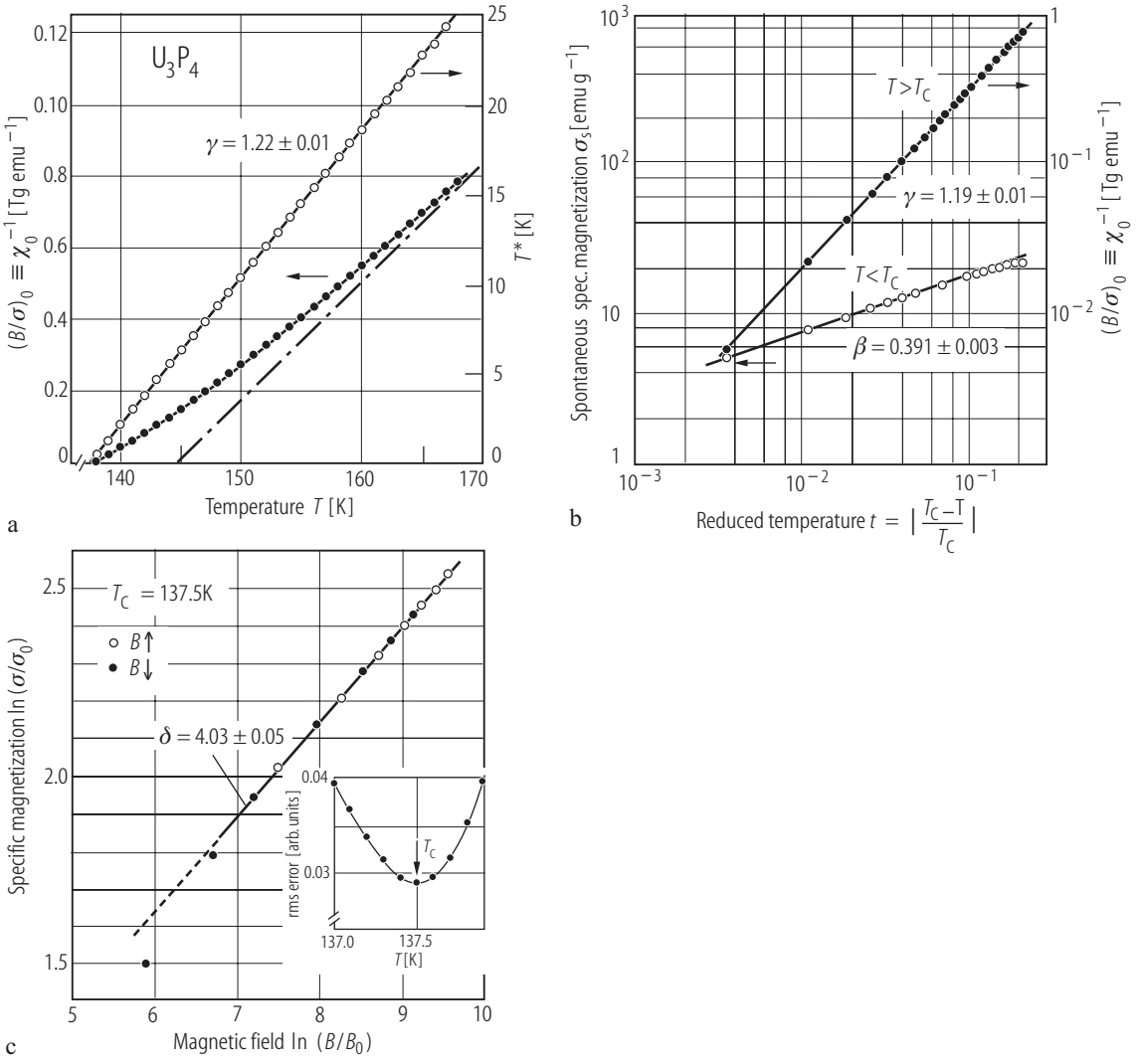

Fig. 81. U_3P_4, sc. **(a)** Inverse initial susceptibility, χ_0^{-1} (filled circles; left-hand side scale), and the Kouvel-Fisher function, $T^* = \chi_0^{-1}(d\chi_0^{-1}/dT)^{-1}$ (open circles; right-hand side scale), vs. temperature, T, near the Curie point [83TA]. The values of χ_0^{-1} were derived from the data presented in Fig. 80 as the intersections of the σ^2 vs. B/σ curves with the B/σ-axis. Note a strong curvature of $\chi_0^{-1}(T)$ in the temperature range up to 35 K above T_C. At higher temperatures the susceptibility follows a Curie-Weiss law (marked by the dash-dotted line) with the parameters: p_{eff} = 2.60(1) μ_B/U atom and Θ_p = 144.8 K. The intersection of the Kouvel-Fisher function with the T-axis defines the Curie temperature T_C = 137.5 K, and its slope yields the critical exponent γ = 1.22(1). **(b)** Spontaneous magnetization, σ_s (open circles; left-hand side scale), and inverse initial susceptibility, χ_0^{-1} (filled circles; right-hand side scale), vs. reduced temperature, $t = \left|\frac{T_C - T}{T_C}\right|$, on a double logarithmic scale [83TA]. The values of σ_s were derived from the data presented in Fig. 80 as the intersections of the σ^2 vs. B/σ curves with the σ^2-axis. The solid lines mark a straight line behaviour of both quantities, and their slopes yield the critical exponents β = 0.391(3) and γ = 1.19(1). **(c)** Critical magnetization isotherm, $\ln(\sigma/\sigma_0)$ vs. $\ln(B/B_0)$, taken at $T = T_C$ = 137.5 K with increasing (open circles) and decreasing (full circles) magnetic field, on samples freely placed in a sample holder [83TA]. ($B_0 = 10^{-4}$ T, σ_0 = 1 emu/g). The solid line is a least-squares fit that yields the critical exponent δ of 4.03(5). Note that this value is exactly the same as that calculated from the scaling relation $\delta = 1 + \gamma/\beta$, with the exponents γ and β derived in panel **(a)** and **(b)**. Inset: determination of T_C by the minimum value of the rms error (for the details see the original paper).

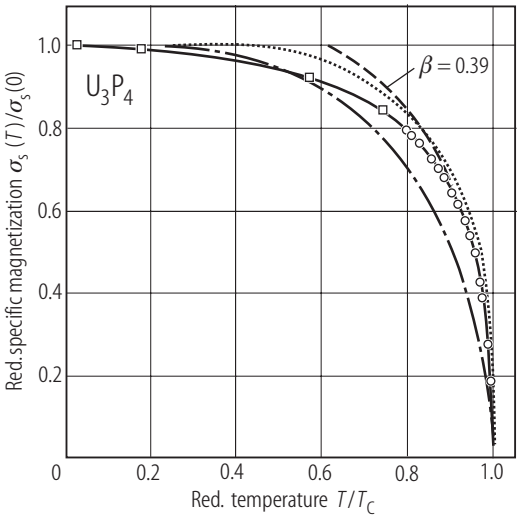

Fig. 82. U_3P_4, sc. Reduced spontaneous specific magnetization, $\sigma_s(T)/\sigma_s(0)$, vs. reduced temperature, T/T_C [83TA]. Open circles: the values derived from the data presented in Fig. 80 as the intersections of the σ^2 vs. B/σ curves with the σ^2-axis; open squares: the experimental data from [81BRTH] (see Fig. 72**)**. The solid line serves as a guide for the eye. The other lines are the theoretical results: the classical Brillouin $J = ½$ function (dash-dotted line), the 3d-Ising $S = ½$ model (dotted line), the power law function $\sigma_s(T)/\sigma_s(0) = 1.6 \cdot t^{\beta}$ with the exponent $\beta = 0.39$ (dashed line). Note that in the vicinity of T_C the experimental data fall in between the Brillouin and Ising behaviours, while at low temperatures they rather follow the classical function. Note also that the power law is fulfilled only for $T > 0.9T_C$.

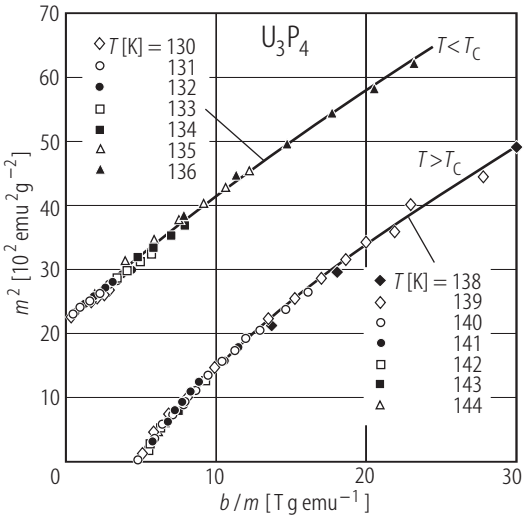

Fig. 83. U_3P_4, sc. Homogeneous equation of state, m^2 vs. b/m; $m^2 = \sigma^2(T) \mid t \mid^{-2\beta}$, $b/m = (B/\sigma) \mid t \mid^{-\gamma}$ where $t = \left|\frac{T - T_C}{T_C}\right|$ [83TA]. The experimental data were taken from Fig. 80**,** and the values of T_C (= 137.5 K) and the critical exponents β (= 0.391(3)) and γ (= 1.19(1)) were assumed as derived in Fig. 81. Note that all the experimental results form two isotherms: one for the data above T_C and one for the data below T_C. The intersections of these isotherms with the corresponding axes yield the parameters $m_0/\sigma_s(0) = 1.69$ and $\mu_s b_0/k_B T = 1.47$ that are close to the values calculated for 3d-Ising systems (1.49 and 1.52, respectively).

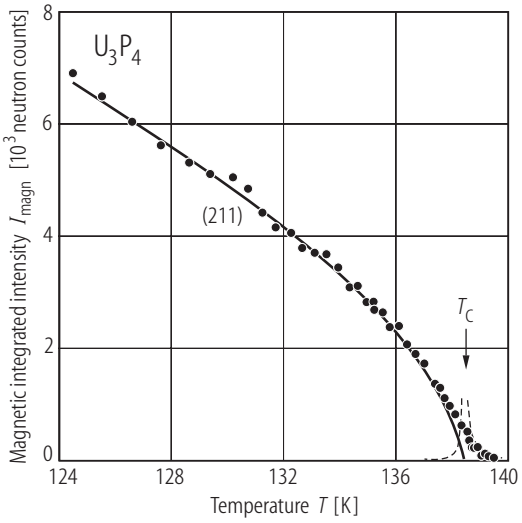

Fig. 84. U_3P_4, sc. Magnetic (211) integrated neutron diffraction intensity, I_{magn}, vs. T in the range 124…140 K as derived from $I(T)$ given in Fig. 76 by extrapolating the nuclear scattering contribution below T_C [93SDKT]. The solid line represents the square of the spontaneous magnetization and the dashed lines show schematically contributions due to the critical scattering obtained by a least squares fit of the experimental data to the formula: $I_{magn} = At_-^{2\beta} + C_-t_-^{-\gamma} + C_+t_+^{-\gamma}$ where the first term accounts for the spontaneous magnetization and the other two for critical scattering below and above the magnetic phase transition (second and third term, respectively), in terms of the reduced temperature $t_- = (T–T_C)/T_C$ and $t_+ = (T_C–T)/T_C$. The best fit parameters are: T_C = 138.46±0.01 K, β = 0.315±0.015, γ = 1.25±0.02, A = 28740±50, C_+ = 0.20±0.02, C_- = 0.04±0.02. Note that the experimental critical exponents β and γ are very close to the theoretical expectations of the 3d-Ising model, i.e. $\beta = 0.312$ and γ = 1.25 (from the series expansion analysis) and are somewhat different than those obtained from the magnetization studies: 0.39 and 1.19, respectively (see Fig. 81b).

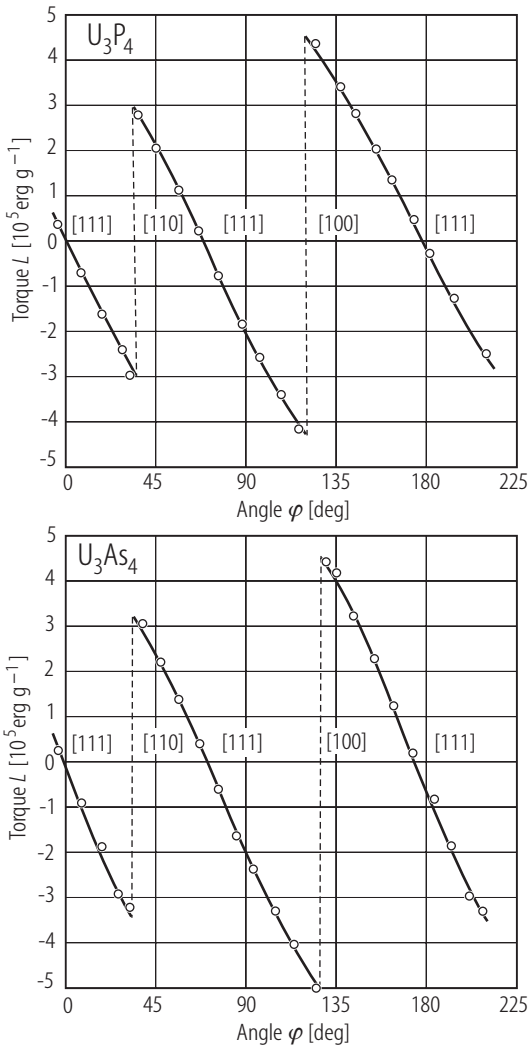

Fig. 85. U_3X_4, X = P, As, sc. Torque curves $L(\varphi)$ measured at T = 78 K in a field of 1.95 T applied in the (110) plane [73BHDL]. The angle φ is between the field direction and the [111] axis. The solid lines are the curves calculated from the formula $L(\varphi) = \sigma^{[111]}B\sin\varphi$. The dashed lines serve as a guide for the eye.

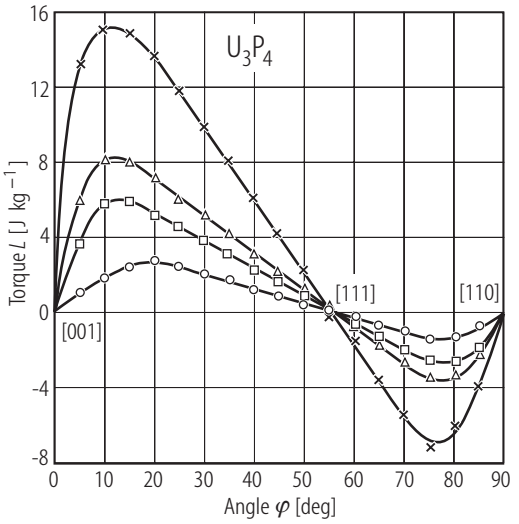

Fig. 86. U_3P_4, sc. Torque curves, $L(\varphi)$, measured at T = 118 K in a magnetic field of 0.34 (circles), 0.65 (squares) and 0.91 T (triangles) on a spherical sample in the (110) plane [78Z]. The crosses mark the values of $L(\varphi,\infty)$ obtained by extrapolation of $L(\varphi)$ to infinite magnetic field. The anisotropy constant K_1 derived from the torque measurements at 118 K amounts to about –40 J/kg.

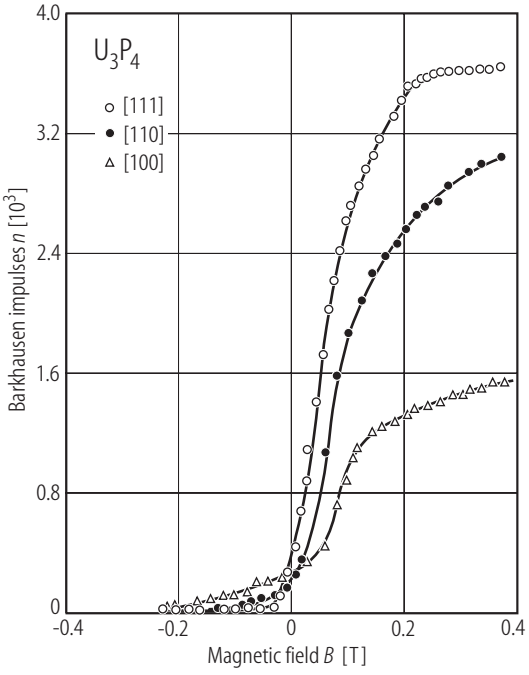

→

Fig. 87. U_3P_4, sc. Number of Barkhausen impulses, n, vs. magnetic field, B, recorded at T = 77 K with $B \parallel$ [111] (open circles), $B \parallel$ [110] (full circles) and $B \parallel$ [100] (open triangles) [77FSMZ]. n is related to the irreversible part of the magnetization change and increases most rapidly for the [111] orientation (easy axis) and most slowly for the [100] orientation (hard axis).

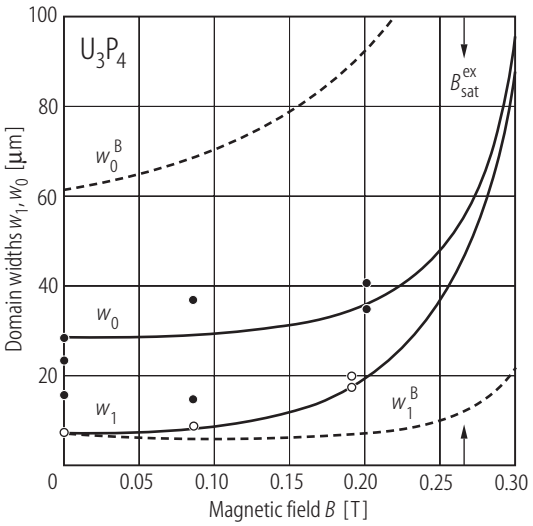

Fig. 88. U_3P_4, sc. Domain width, w_i, vs. magnetic field, B, applied perpendicular to the thin plate surface cut perpendicular to the [111] direction [92S]. Open circles: w_1 – width of the surface domains; full circles: w_0 – width of the inner domains. The solid lines are the domain width changes calculated assuming the energy density of 180°-walls j = 11 erg/cm^2. The dashed lines represent the model calculations for j = 15 erg/cm^2. B^{ex}_{sat} is the experimentally derived value of the external magnetic field above which the sample becomes saturated and the domain structure disappears. See the original paper for the details on the theoretical models applied.

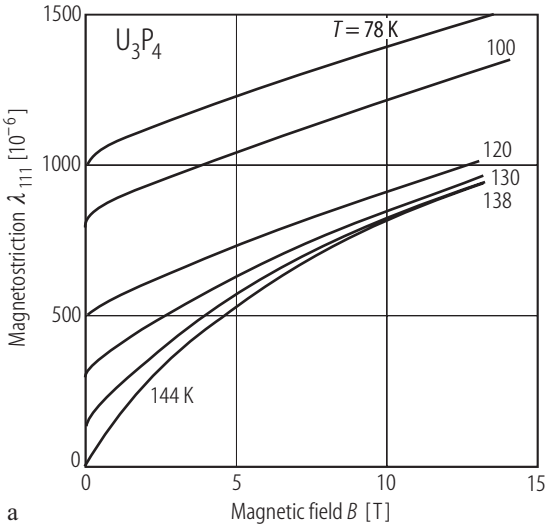

a

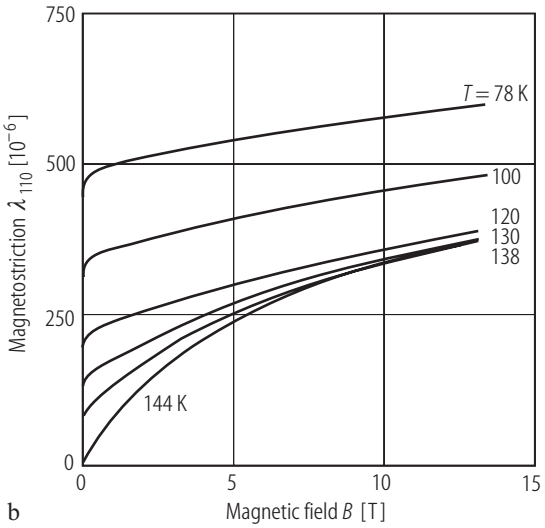

b

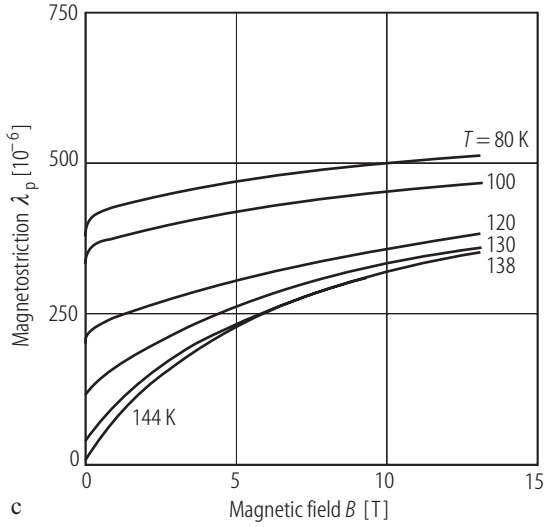

c

Fig. 89. U_3P_4, sc. Magnetostriction, λ, vs. magnetic field, B, taken at various temperatures in the range 78…144 K (specified in the figures), measured in pulsed magnetic fields up to 15 T with **(a)** $B \parallel [111]$, **(b)** $B \parallel [110]$ and **(c)** polycrystal [71THBD]. Note a very large magnetostriction along the [111] direction while that along [100] is equal to zero (not shown).

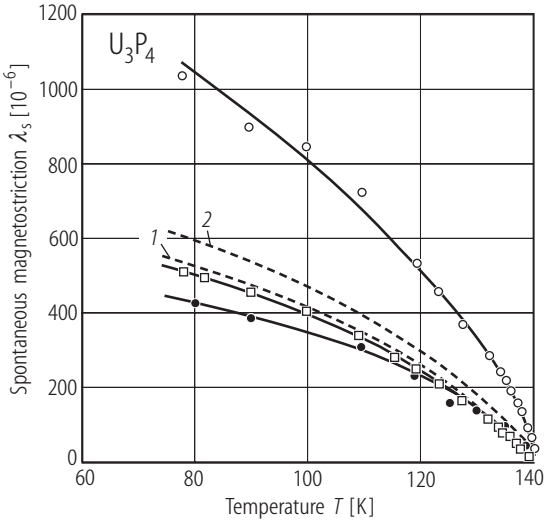

Fig. 90. U_3P_4, sc. Spontaneous magnetostriction, λ_s, vs. temperature, T, in the range 78…140 K taken with $B \parallel [111]$ (open circles) and $B \parallel [110]$ (open squares) [71THBD]. The full circles represent the data for a polycrystal. The experimental points were derived from the data presented in Fig. 89 by extrapolation of $\lambda(B)$ to zero field. The solid lines serve as a guide for the eye. The dashed line No.1 is a calculated $\lambda_s(T)$ variation for the [110] direction: $\lambda_s^{110}(T) = ½\,\lambda_s^{111}(T)$. The dashed line No.2 is a calculated $\lambda_{poly}(T)$ variation, where $\lambda_{poly} = \lambda_s^{111}(1+8\pi)/2\pi$. Note a fairly good agreement between the experimental and calculated results.

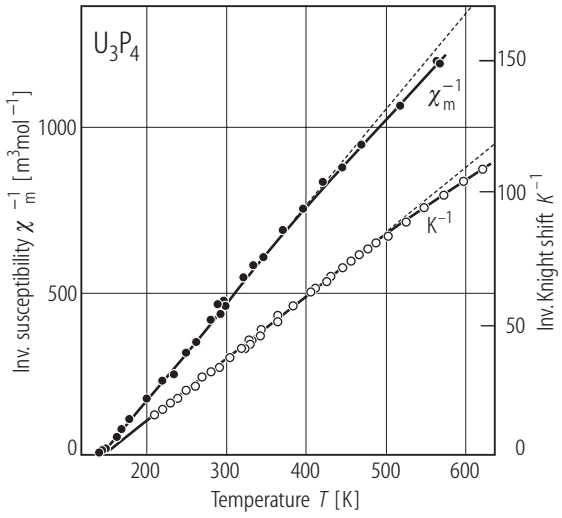

Fig. 91. U_3P_4. Inverse molar magnetic susceptibility, χ_m^{-1}, (full circles) and inverse ^{31}P Knight shift, K^{-1}, (open circles) vs. temperature, T, in the ranges 140…570 K and 210…620 K, respectively [77KSM]. The dashed lines represent a Curie-Weiss law with Θ_p = 140 K and p_{eff} = 2.72 μ_B/U atom. The deviations from a straight-line behaviour at higher temperatures are probably due to the contribution of conduction electrons. The solid lines are fits of the relevant experimental data to the formulas: $\chi_m^{-1} = \left(\frac{A}{T} + B\right)^{-1} - \lambda$ and $K = K_0 + \alpha\chi_m$ with the parameters: $A = 3.43 \cdot 10^{-5}$ m^3 K/mol, $B = 1.42 \cdot 10^{-9}$ m^3/mol, $\lambda = 4.06 \cdot 10^6$ mol/m^3, $K_0 = -6 \cdot 10^{-5}$ and $\alpha = 1.255 \cdot 10^5$ mol/m^3. The s-f coupling $\Gamma = -2.4$ eV is in good agreement with that reported in [67J] (compare Fig. 92).

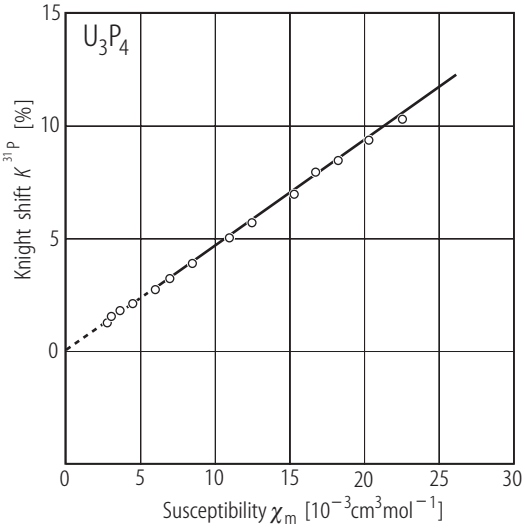

Fig. 92. U_3P_4. ^{31}P Knight shift, K, vs. molar magnetic susceptibility, χ_m, measured in the temperature range 175…550 K [67J]. The susceptibility data were taken from [63TT]. The dashed line is an extrapolation of a linear relation between K and χ_m up to $\chi_m = 0$. B_{hf} = 2.59 T/μ_B. From the slope of this straight line the s-f exchange integral is calculated to be $\Gamma_{sf} = -2.4$ eV.

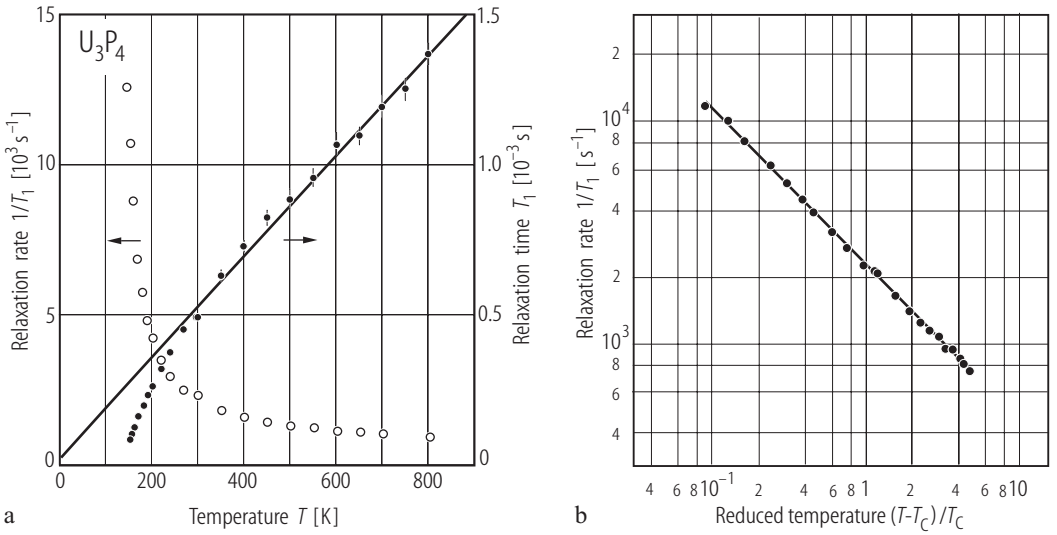

Fig. 93. U_3P_4. **(a)** Nuclear longitudinal relaxation rate of ^{31}P, $1/T_1$ (open circles; left-hand side scale), and its inverse, T_1 (full circles; right-hand side scale), vs. temperature, T, in the range 150…800 K [85TNSK]. The solid line represents the function: $T_1 = 3.69 \cdot 10^{-5} + 1.54 \cdot 10^{-6}\ T$. The linear increase of T_1 above 300 K indicates that U_3P_4 is a localized-moment system and that the correlation time of the uranium moments is dominated by the scattering due to conduction electrons. **(b)** $1/T_1$ vs. reduced temperature, $t = (T–T_C)/T_C$, in the form of double logarithmic plot [85TNSK]. The solid line marks the critical-like divergence $1/T_1 \sim [(T–T_C)/T_C]^{-0.68}$. The observed behaviour evidences the development of short-range magnetic ordering at temperatures well above $T_C = 137.8$ K.

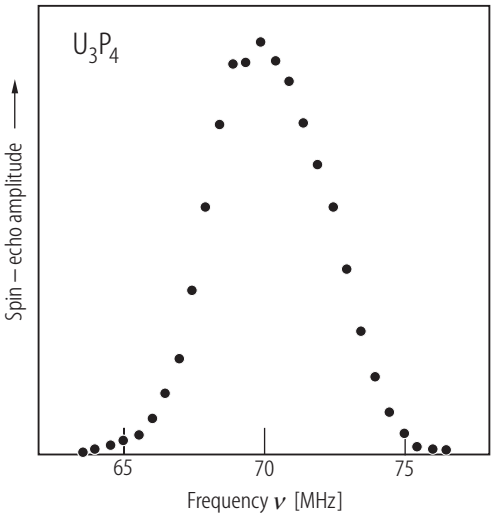

Fig. 94. U_3P_4. Spin-echo NMR spectrum of ^{31}P taken at $T =$ 4.2 K in zero external magnetic field [85TNSK]. The signal does not change in an applied field, which means that it originates mostly from ferromagnetic domains. The hyperfine field derived from the position of the centre of the spectrum corresponds well with the value of the hyperfine coupling constant $B_{hf} = 2.71$ T/μ_B, found in the paramagnetic region (see the original paper). This value of B_{hf} is close to that found by [67J] (see Fig. 92**)**.

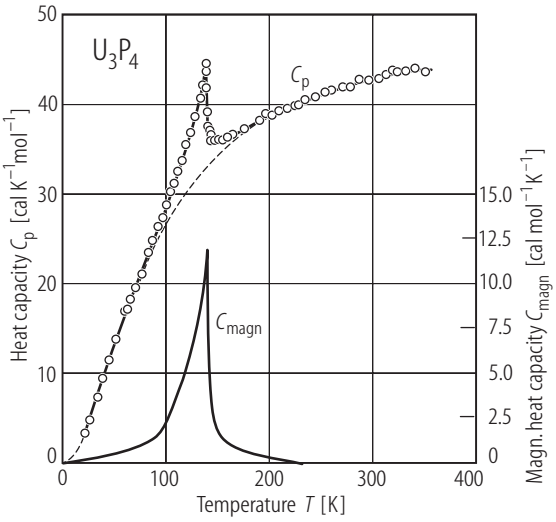

Fig. 95. U_3P_4. Heat capacity, C_p, vs. temperature, T, in the range 22.5…349.0 K [66SBT]. A sharp λ-shaped peak manifests a second-order ferromagnetic phase transition at T_C = 138.3 K. The dashed line represents the lattice contribution, C_L, calculated using a combination of two Debye functions with the Debye temperatures of 175 and 450 K, respectively (for details see the original paper). The solid-line curve on the bottom is the magnetic contribution to the specific heat, C_{magn}, obtained by subtracting C_L from C_p and adding the magnetic specific heat term calculated for the temperatures T < 70 K in the framework of general theory of ferromagnetic spin wave excitations.

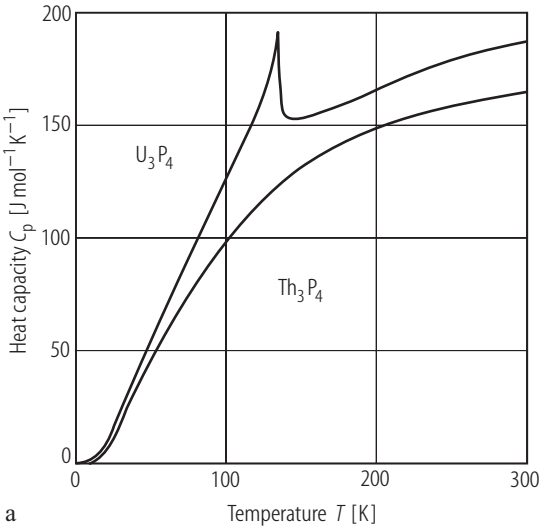

a

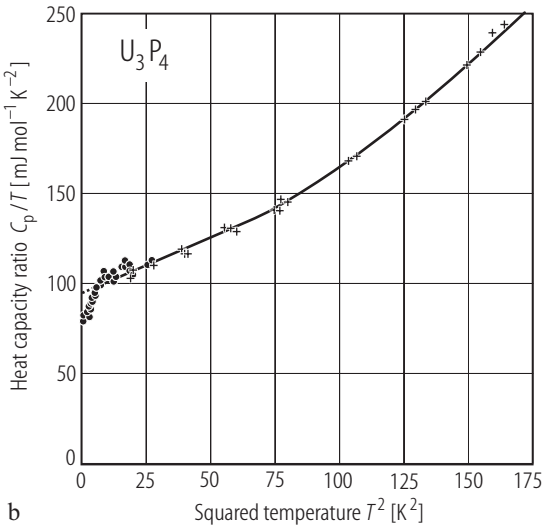

b

Fig. 96. U_3P_4, Th_3P_4. **(a)** Heat capacity, C_p, vs. temperature, T [86ABHM]. The λ-shaped peak in U_3P_4 occurs at the Curie temperature of ≈ 137 K. **(b)** Low-temperature capacity heat in the form of C_p/T vs. T^2 plot [86ABHM]. Points and crosses correspond to the measurements done using two different techniques. The kink at 2.64 K has unknown origin but a similar one was reported in [01IWMA] to occur at 2.8 K. The extrapolation $C/T \rightarrow 0$ from temperatures above the kink yields: $\gamma(0)$ = 32 mJ/(K^2 mol U), $\Theta_D(0)$ = 279 K. These values differ from those derived in [67CDJM]: $\gamma(0)$ = 25.5 mJ/(K^2 mol U), $\Theta_D(0)$ = 245 K, and in [77AFWG]: $\gamma(0)$ = 12.3 mJ/(K^2 mol U).

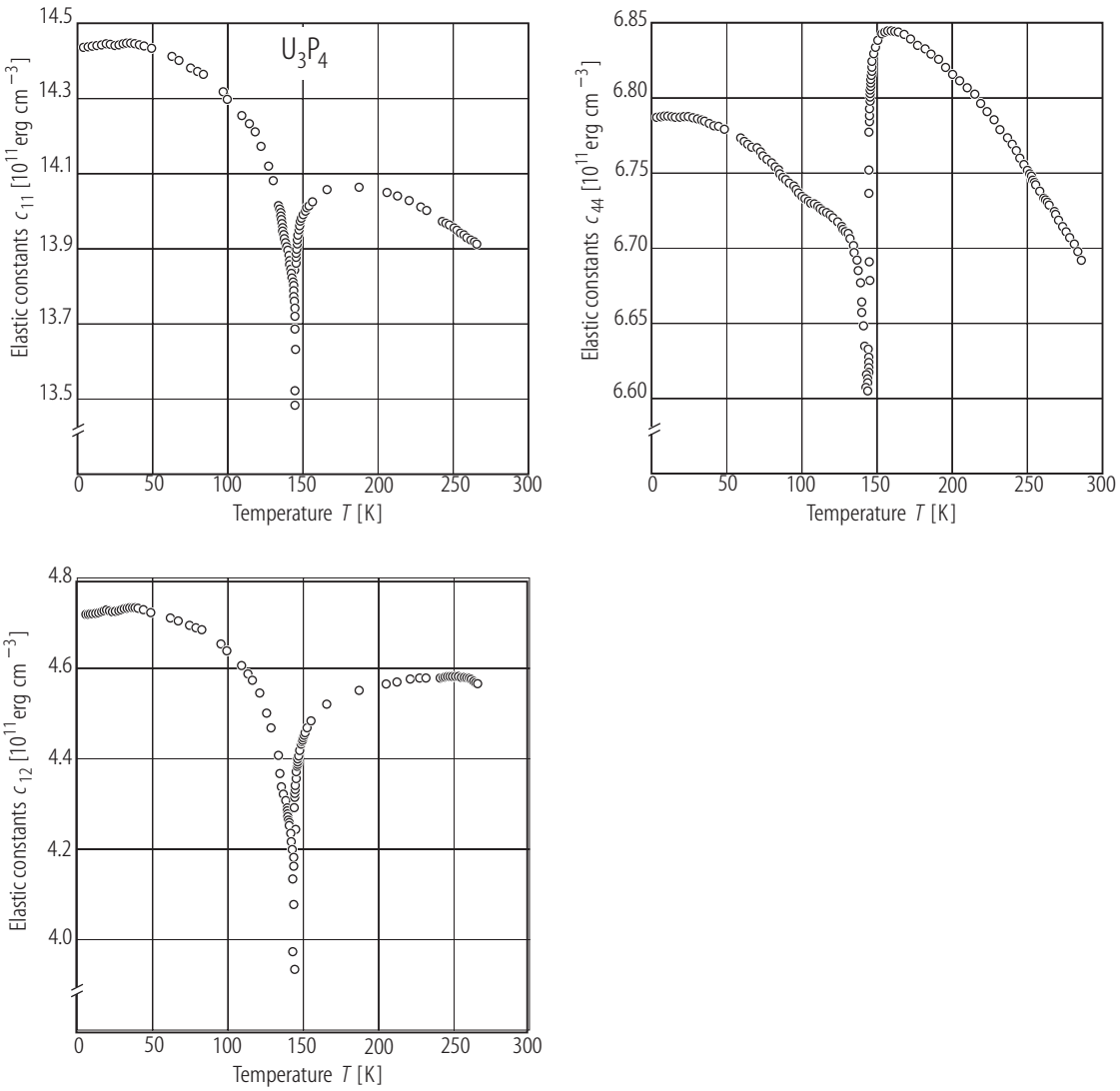

Fig. 97. U_3P_4, sc. Elastic constants, c_{11}, c_{12} and c_{44}, vs. temperature, T, determined by means of ultrasound propagation studies along the [110] direction [93KFL]. All the constants rapidly soften at the Curie temperature of 138 K. For the shear constant c_{12} the effect is as large as ~13 %. The elastic behaviour below T_C is governed mainly by exchange striction and resonant interaction of phonons and spin waves, both driven by domain wall movement and increasing cubic-to-rhombohedral distortion (see Fig. 69**)**. The ultrasound velocity measured at 4.2 K along the [110] axis is 4.3, 2.6 and 2.2 · 10^3 m/s for the ion displacements along [110], [001] and [1 $\bar{1}$ 0], respectively.

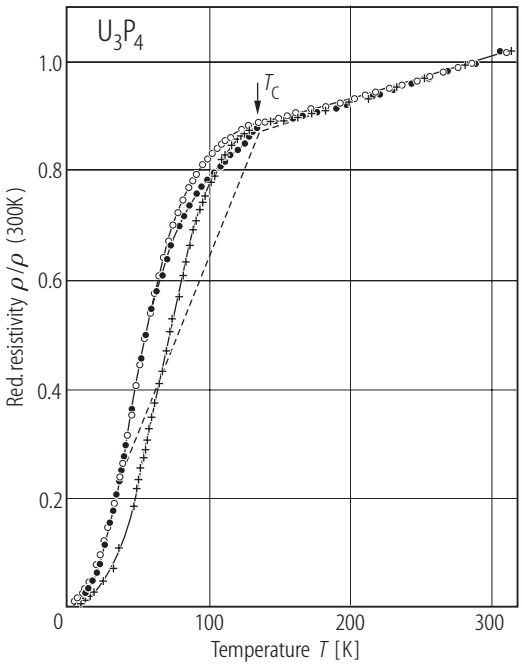

Fig. 98. U_3P_4, sc. Normalized electrical resistivity, ρ/ρ(300K), vs. temperature, T, measured along the [100] (open circles), [110] (full circles) and [111] (crosses) directions [71HB]. At 300 K the resistivity was equal to 284, 240 and 296 μΩcm, for the [100], [110] and [111] directions, respectively. Note a strongly anisotropic behaviour of $\rho(T)$ in the ordered state. T_C = 138.2 K. The resistivity measured along the [100] and [110] directions shows in the ferromagnetic region a significant dependence on magnetic and thermal history of the sample (not shown) because of magnetic domain effect. The dashed line approximates the relation $\rho(T) = \rho_0^{\infty} \frac{T}{T_C} + BT$ for $T < T_C$ and $\rho(T) = \rho_0^{\infty} + BT$ for $T > T_C$, where ρ_0^{∞} is the spin disorder resistivity and the term BT describes the phonon contribution to the total resistivity.

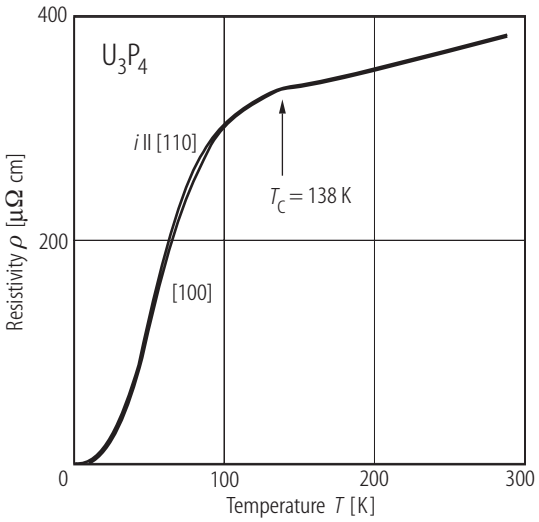

Fig. 99. U_3P_4, sc. Electrical resistivity, ρ, vs. temperature, T, down to 0.4 K measured with the current flowing along the [100] (lower curve) and [110] (upper curve) directions [01IWMA]. RRR is 1590 and the residual resistivity ρ_0 is 0.24 μΩcm along [100] and 2180 and 0.17 μΩcm, respectively, along [110]. These values indicate a superior quality of the samples measured. In the paramagnetic region the resistivity is isotropic, as expected for a cubic crystal structure. The arrow marks the ferromagnetic phase transition at T_C = 138 K. Below 10 K the resistivity follows an AT^2-dependence with A = 0.030 and 0.037 μΩcm/K^2 along [100] and [110], respectively.

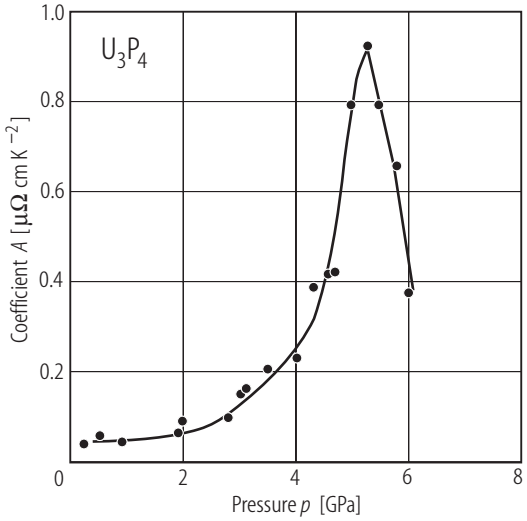

Fig. 100. U_3P_4, sc. Coefficient in the quadratic thermal dependence of the electrical resistivity, A, vs. pressure, p [02TTKA]. A sharp maximum is found for p_{cr} = 5.3 GPa.

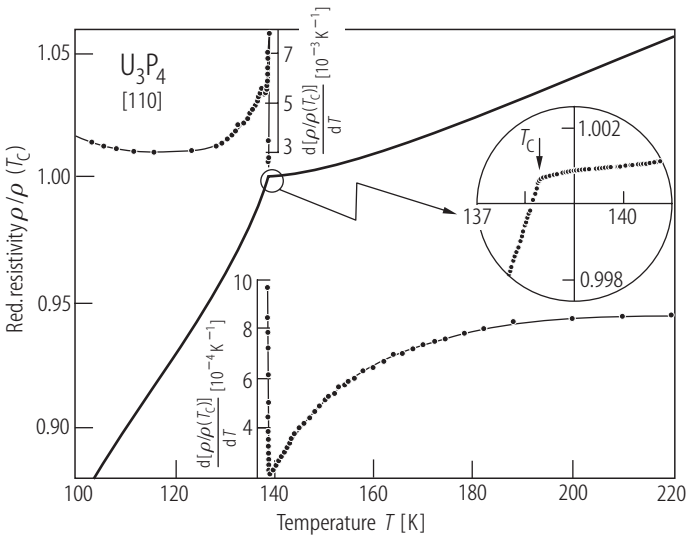

Fig. 101. U_3P_4, sc. Normalized electrical resistivity, $\rho/\rho(T_C)$, measured along the [110] direction (solid curve) and its temperature derivative, $d[\rho/\rho(T_C)]/dT$ (lines with full circles), vs. temperature, T, in the range 105…220 K [80H3]. T_C = 138.26(3) K. In the vicinity of T_C (inset) the resistivity behaves in manner characteristic of ferromagnetic semimetals. Note a splitting of $d[\rho/\rho(T_C)]/dT$ into two separate maxima just below T_C.

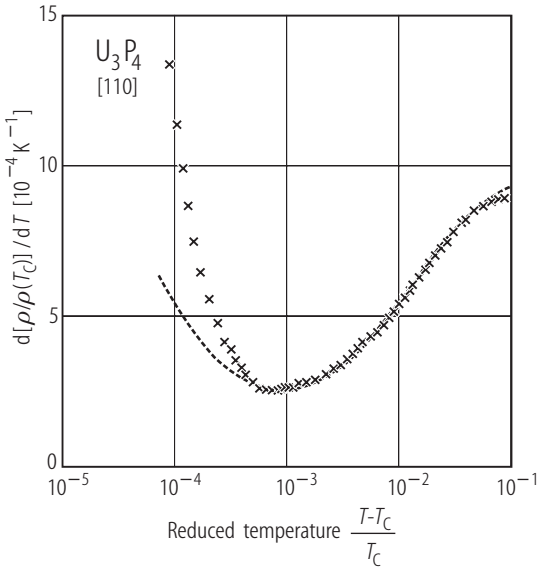

Fig. 102. U_3P_4, sc. Temperature derivative of the normalized electrical resistivity, $d[\rho/\rho(T_C)]/dT$, vs. normalized temperature, $(T–T_C)/T_C$ (note a logarithmic scale), in the paramagnetic region [80H3]. The resistivity was measured along the [110] axis. The dashed line is the least-squares fit to the formula comprising the residual, phonon and magnetic contributions to the resistivity, calculated using the critical exponent $\upsilon = 0.6$ (for details see the original paper). The universal behaviour is well seen for temperatures about 2 K higher than T_C.

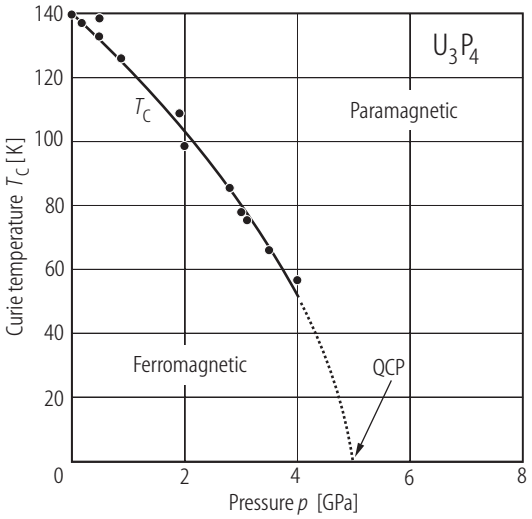

Fig. 104. U_3P_4, sc. Pressure – Curie temperature (p-T_C) phase diagram [02TTKA]. $T_C(p=0)$ = 138 K; p_{cr} = 5 GPa. The Curie temperature under pressure was defined as a minimum in the temperature derivative of the electrical resistivity. Compare results given by [80H2] up to 0.82 GPa (see Fig. 103). QCP: quantum critical point.

For Fig. 103 see next page

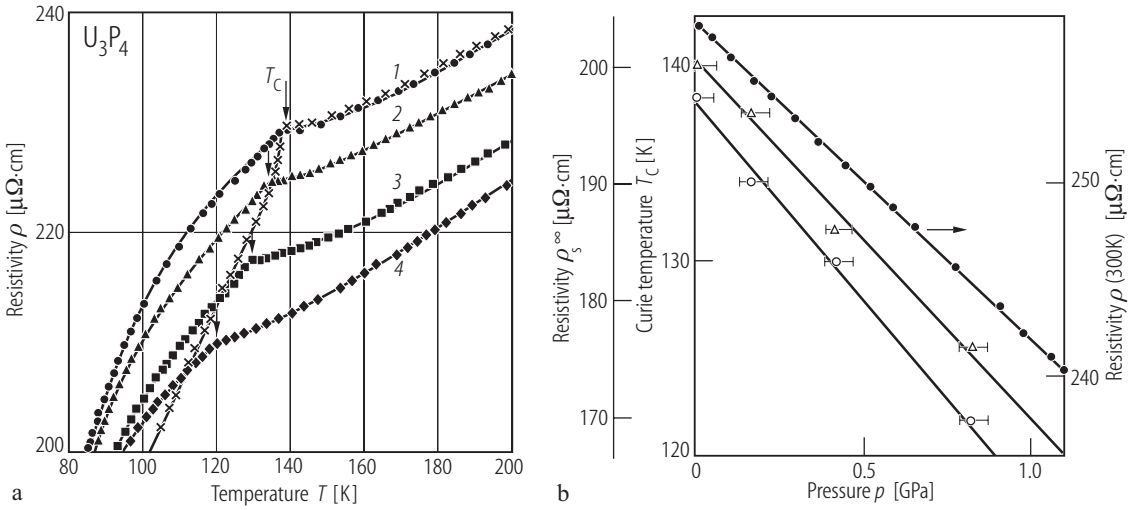

Fig. 103. U_3P_4, sc. **(a)** Electrical resistivity, ρ, vs. temperature, T, in the range 85…200 K, measured along the [110] axis under various hydrostatic pressures: Curve *1*) p = 0 (circles and crosses), *2*) 1.6 (triangles), *3*) 4.1 (squares) and *4*) 8.2 kbar (diamonds) [80H2]. The difference for two runs at p = 0 in the ordered state is due to domain effect. The arrows mark the respective Curie temperatures. **(b)** Electrical resistivity at 300 K, ρ(300K), (full circles; right-hand scale), high-temperature limit of the spin disorder resistivity, ρ_s^∞, (open triangles; separate left-hand scale) and Curie temperature, T_C, (open circles; left hand scale) vs. pressure, p [80H2]. The values of ρ_s^∞ were determined by extracting from the total resistivity [presented in panel **(a)**] the phonon contribution taken as a slope of $\rho(T)$ at 180 K. Both ρ(300K) and ρ_s^∞ decrease linearly with pressure at a rate of 0.62 and 1.5 %/kbar, respectively. The rate of decrease in T_C under pressure is 2 K/kbar. The pressure dependence of the resistivity reflects changes in the conduction band due to the decrease in U-U spacings.

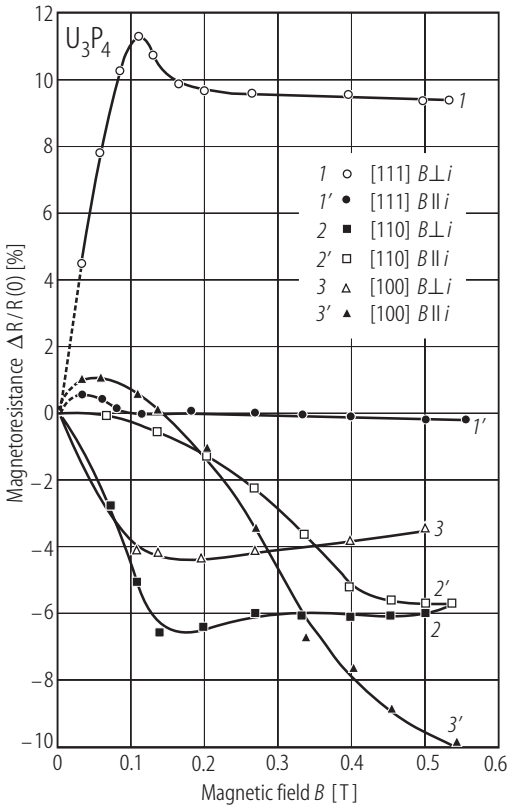

Fig. 105. U_3P_4, sc. Transverse and longitudinal magnetoresistance, $\Delta R/R(0)$, vs. magnetic field, B, up to 0.53 T, measured at T = 77 K in various configurations of the current and the magnetic field with respect to the crystallographic axes [71HB]. The trend in the curves is unusual for a simple collinear ferromagnet (see the original paper).

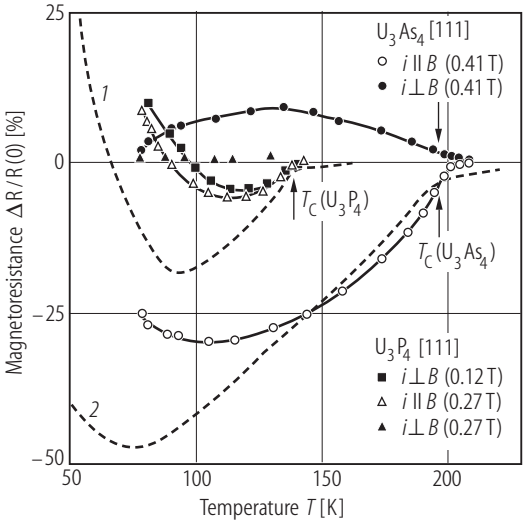

Fig. 106. U_3X_4, X = P, As, sc. Transverse and longitudinal magnetoresistance, $\Delta R/R(0)$, vs. temperature in the range 77…220 K, measured with the current flowing along the [111] direction and the magnetic field applied either parallel to the current (open symbols) or perpendicular to it (full symbols) [71HB]. Full squares: U_3P_4, B = 0.12 T; full and open triangles: U_3P_4, B = 0.27 T; full and open circles: U_3As_4, B = 0.41 T. The arrows mark the Curie temperatures. The dashed lines 1 and 2 represent the corresponding difference between the experimental $R(T)$ dependencies along the [111] direction and the assumed linear dependence for a simple ferromagnet (see Fig. 98 and Fig. 154). Note a similarity between these curves and the $\Delta R/R(0)$ vs. T data.

For Fig. 107 see next page

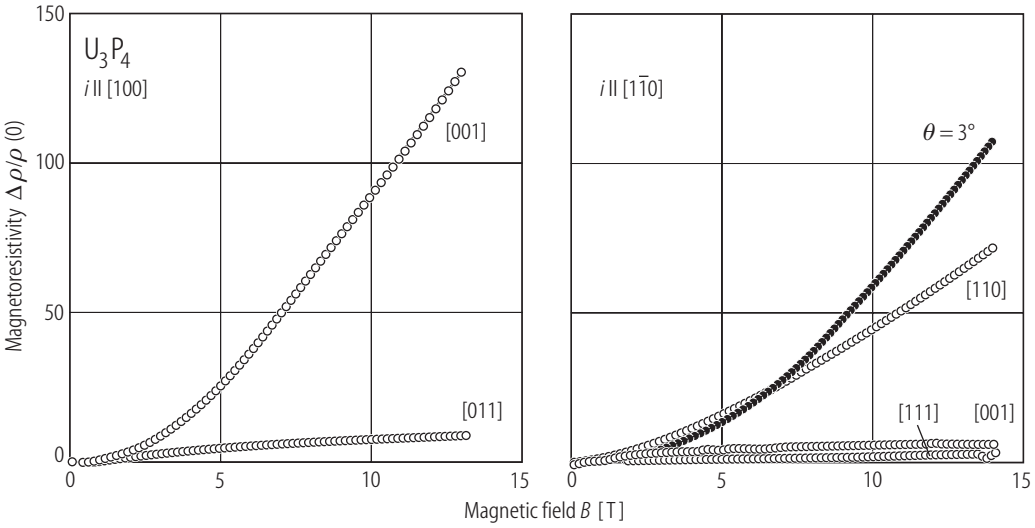

Fig. 108. U_3P_4, sc. Magnetoresistivity, $\Delta\rho/\rho(0)$, vs. magnetic field, B, measured at T = 0.45 K with the electrical current flowing along the [100] direction and magnetic fields applied along the [001] axis (upper curve) and the [011] axis (lower curve) (left-hand side panel), and with the current flowing along the $[1\,\bar{1}\,0]$ direction and magnetic fields applied along the [110] axis (upper curve), the [001] axis (middle curve) and the [111] axis (lower curve) (right-hand side panel) [01IWMA]. The full circles denote the data taken with the current flowing along the $[1\,\bar{1}\,0]$ direction for the field tilted by 3° from [001] towards [110] in the $(1\,\bar{1}\,0)$ plane. Note that in contrast to the behaviour found for U_3As_4 (compare Fig. 167), $\Delta\rho/\rho(0)$ saturates at high fields for the configurations ($i \parallel$ [100], $B \parallel$ [011]) and ($i \parallel [1\,\bar{1}\,0]$, $B \parallel$ [001] and $B \parallel$ [111]). For the other configurations of i and B, $\Delta\rho/\rho(0)$ is proportional to B^2. The observed behaviour indicates that the compound is a compensated metal with the presence of some open orbits (see Fig. 109).

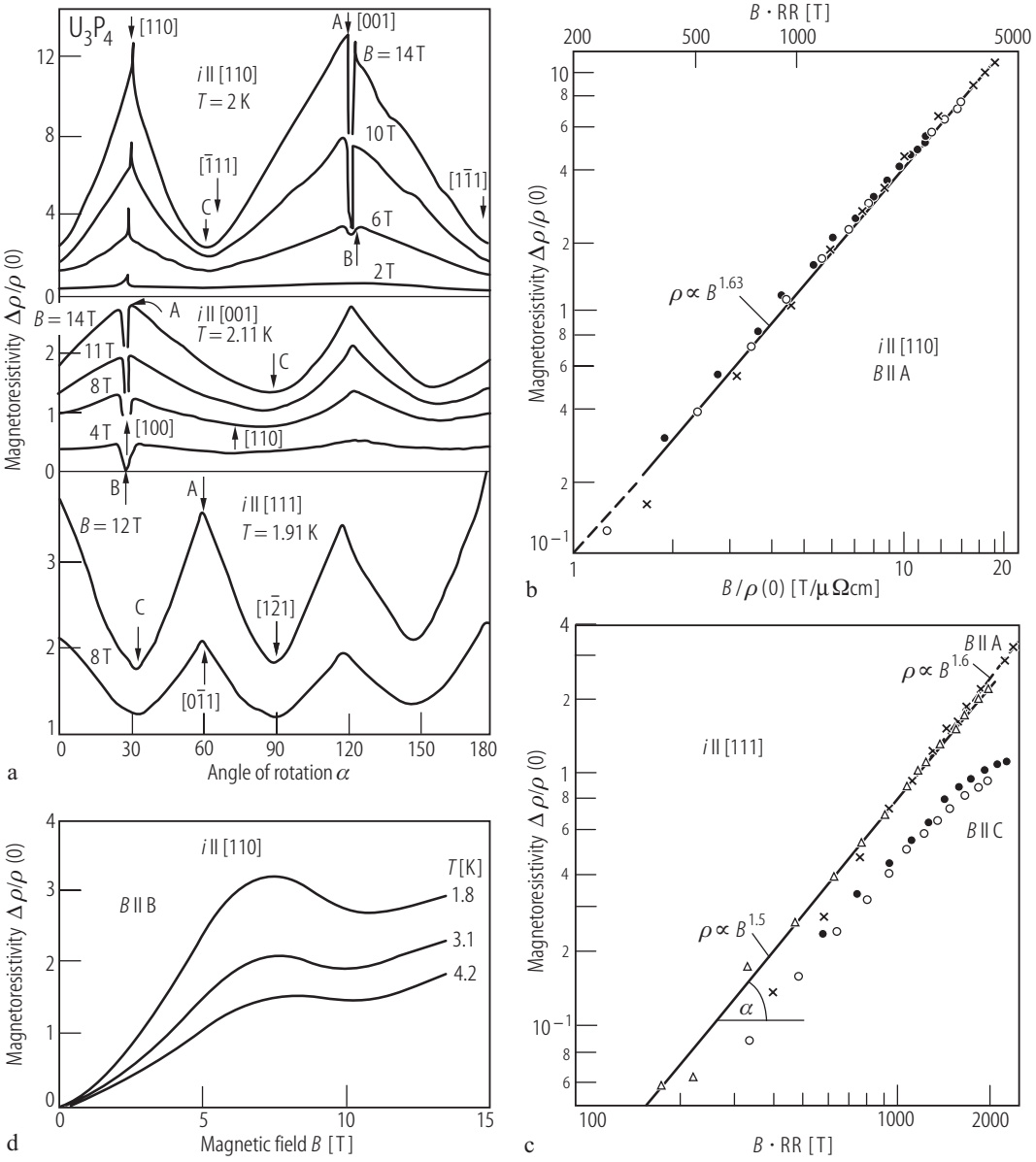

Fig. 107. U_3P_4, sc. **(a)** Magnetoresistivity, $\Delta\rho/\rho(0)$, vs. angle between magnetic field and electrical current, $\alpha(\boldsymbol{B},\boldsymbol{i})$, measured around 2 K in the magnetic field of various magnitudes [77BHP]. Top panel: T = 2 K, i ∥ [110], B = 2, 6, 10 and 14 T (curves from the bottom to the top); middle panel: T = 2.11 K, i ∥ [001], B = 4, 8, 11 and 14 T (curves from the bottom to the top); bottom panel: T = 1.91 K, i ∥ [111], B = 8 and 12 T (lower and upper curve, respectively). The arrows A, B and C mark the directions for which $\Delta\rho/\rho(0)$ was measured as a function of the magnetic field strength (see below). Note a strongly anisotropic behaviour. Unusual narrow deep minima located exactly at the [100] direction are attributed to a magnetic breakdown effect. **(b)** Reduced Kohler's plot, $\Delta\rho/\rho(0)$ vs. $B/\rho(0)$, measured at T = 1.8 K (crosses), 3.1 K (open circles) and 4.2 K (full circles) with the current flowing along the [110] axis and the magnetic field applied along the A direction (see panel **(a)**) [77BHP]. Note a double logarithmic scale. The solid line shows a straight-line behaviour with $\rho \sim B^{1.63}$. **(c)** Reduced Kohler's plot, $\Delta\rho/\rho(0)$ vs. B·RR, measured at T = 1.85 K (crosses), 2.06 K (full circles) and 4.2 K (open circles) with the current flowing along the [111] axis and the magnetic field applied along the A and C-directions (upper and lower results respectively) [77BHP]. RR is the resistivity ratio $\rho(300)/\rho(T)$ in zero field. Note a double logarithmic scale. The solid line shows a straight-line behaviour with $\rho \sim B^{1.5}$, and the dashed line marks a $\rho \sim B^{1.6}$ behaviour. **(d)** Magnetoresistivity, $\Delta\rho/\rho(0)$, vs. magnetic field, B, measured at T = 1.8, 3.1 and 4.2 K with the current flowing along the [110] axis and the magnetic field applied along the B-direction (see panel **(a)**) [77BHP]. For this orientation of $\boldsymbol{B}$ and $\boldsymbol{i}$ the Kohler's rule is not followed.

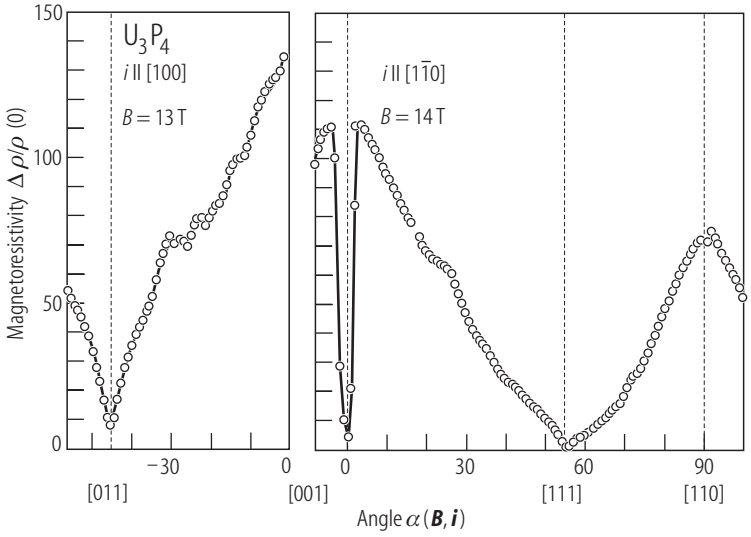

Fig. 109. U_3P_4, sc. Magnetoresistivity, $\Delta\rho/\rho(0)$, vs. angle between magnetic field and electrical current, $\alpha(\boldsymbol{B},\boldsymbol{i})$, measured at T = 0.45 K in the magnetic field of 13 T with the current flowing along the [100] axis (left-hand side panel) and in the magnetic field of 14 T with the current flowing along the [1 $\bar{1}$ 0] axis (right-hand side panel) [01IWMA]. Sharp dips at B ∥ [001] and B ∥ [111], found for i ∥ [1 $\bar{1}$ 0], and at B ∥ [011], found for i ∥ [100], indicate the existence of open orbits along [110], [1 1 $\bar{2}$] and [0 1 $\bar{1}$]. For all these directions $\Delta\rho/\rho(0)$ saturates at high fields (see Fig. 108).

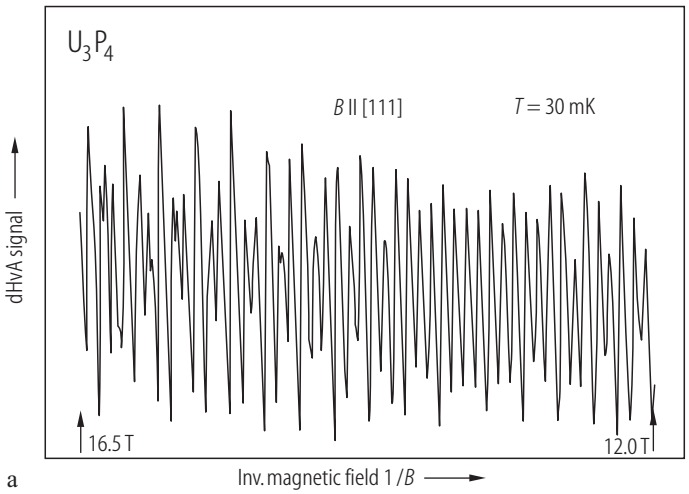

a

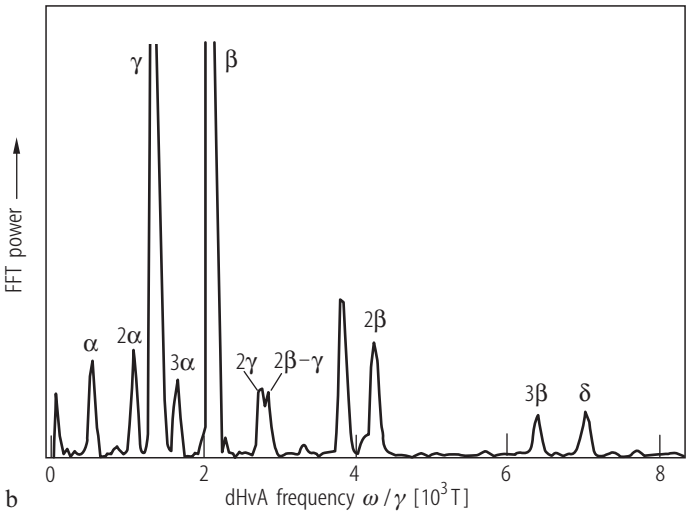

b

Fig. 110. U_3P_4, sc. **(a)** dHvA oscillations measured at T = 30 mK in magnetic fields ranging from 12 to 16.5 T applied along the [111] axis [01IWMA]. **(b)** Fast Fourier transform spectrum corresponding to the data from panel **(a)** [01IWMA]. Note the presence of four fundamental branches labeled α, β, γ and δ in the frequency range from $2.2 \cdot 10^2$ to $7.0 \cdot 10^3$ T. The other features are higher harmonics, sum and difference components of the fundamental branches. For the angular dependence of the dHvA frequencies see Fig. 111.

→

Fig. 112. U_3X_4, X = P, As. Thermoelectric power, S, vs. temperature, T, in the range 100…800 K [72H]. Full circles: U_3P_4; open circles: U_3As_4. Note for U_3As_4 a change in the sign of S from negative above ca. 370 K to positive at lower temperatures (compare Fig. 171) and for both compounds the anomalies at their Curie temperatures (marked by the thin arrows). The values of the Fermi energy, concentration of free carrier and their effective mass estimated from $S(T)$: E_F = 1 eV, n = 1.4 per U atom and m^* = 3.3 m_0. The bold arrow marks the change of the sign of S in U_3As_4.

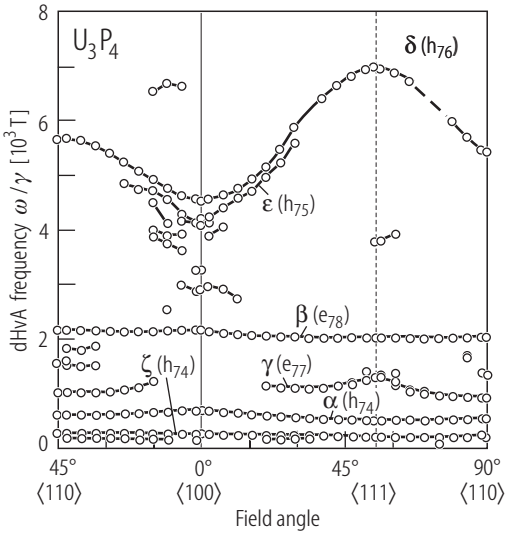

Fig. 111. U_3P_4, sc. Angular dependence of the dHvA frequencies measured as in Fig. 110 [01IWMA]. The branches α, β, δ and ζ, observed in the whole angular region, imply closed Fermi surfaces. The branches γ and ε were not observed in the whole angular range, probably because of the curvature factor of the Fermi surface or very large cyclotron mass. The branches α, β and γ were detected also in earlier dHvA studies [93IATS]. The effective cyclotron mass is 7.8 m_0, 8.1 m_0, 8.7 m_0 and 30 m_0 for the branch α, β, γ and δ, respectively. The mean free path for these branches ranges from 81 to 140 nm, indicating high quality of the single crystal studied (see also Fig. 99). The Dingle temperature ranges from 0.16 to 0.31 K. For Brillouin zone and cross sections of the theoretical Fermi surfaces calculated by [99AHYP] see Fig. 29. The origin of each dHvA branch is as follows: branch α – h_{74} (a band 74-hole surface); branch β – e_{78} (a band 78-electron surface centered at Γ); branch γ – e_{77} (an inner orbit of the band 77-electron surface centered at P); branch δ – h_{76} (a band 76-hole surface centered at H); branch ε – h_{75} (a band 75-hole surface centered at H); branch ζ – e_{79} (a band 79-electron surface centered at Γ). The open orbits observed in the magnetoresistance measurements (see Fig. 109) are probably related to a multiply-connected band 77-electron Fermi surface, denoted as e_{77}.

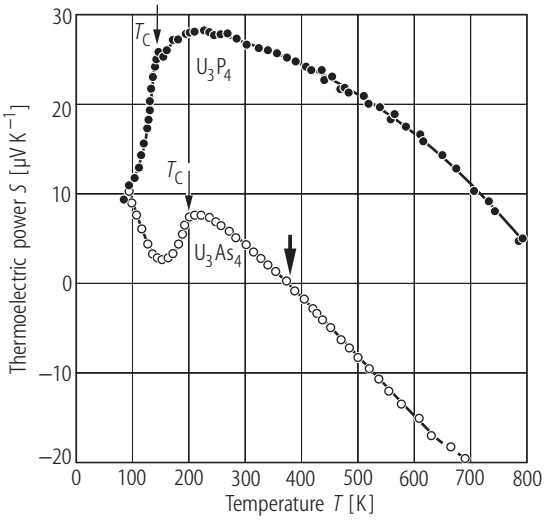

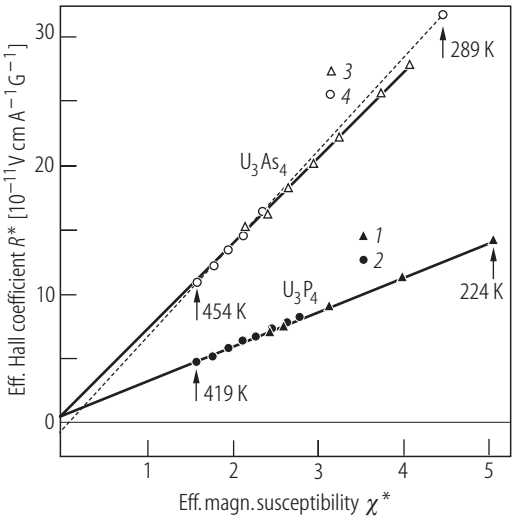

Fig. 113. U_3X_4, X = P, As. Effective Hall coefficient, R^*, measured in the temperature range 224…454 K, vs. effective magnetic susceptibility, $\chi^* = \dfrac{\chi}{1+4\pi\chi\Theta_p}$, where χ is the volume powder susceptibility [72H]. For each compound two different samples were studied (different symbols). The straight lines are fits to the function: $R^* = R_o + 4\pi R_s\chi^*$. For U_3P_4 the parameters are: $R_o = 5 \cdot 10^{-12}$ Vcm/AG and $R_s = 2.76 \cdot 10^{-8}$ Vcm/AG. For U_3As_4 the parameter R_o ranges from $-5 \cdot 10^{-12}$ to $5 \cdot 10^{-12}$ Vcm/AG and the parameter R_s ranges from $6.6 \cdot 10^{-8}$ to $7.2 \cdot 10^{-8}$ Vcm/AG (note the difference in the slope of solid and dashed lines). For both compounds the anomalous Hall coefficient, R_s, is positive and about three orders of magnitude higher than R_o.

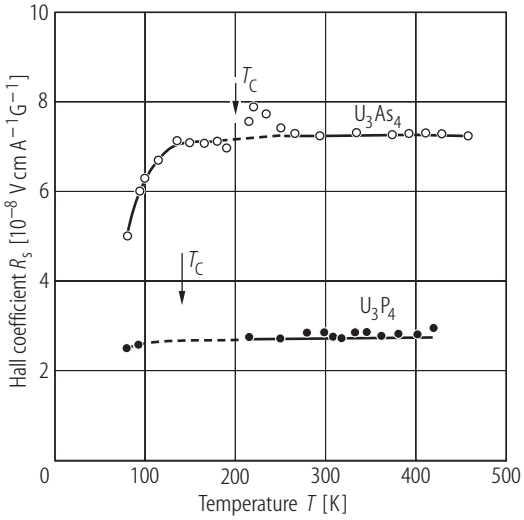

Fig. 114. U_3X_4, X = P, As. Anomalous Hall coefficient, R_s, vs. temperature, T, in the range 80…450 K [72H]. Full circles: U_3P_4; open circles: U_3As_4. The arrows mark the respective Curie temperatures.

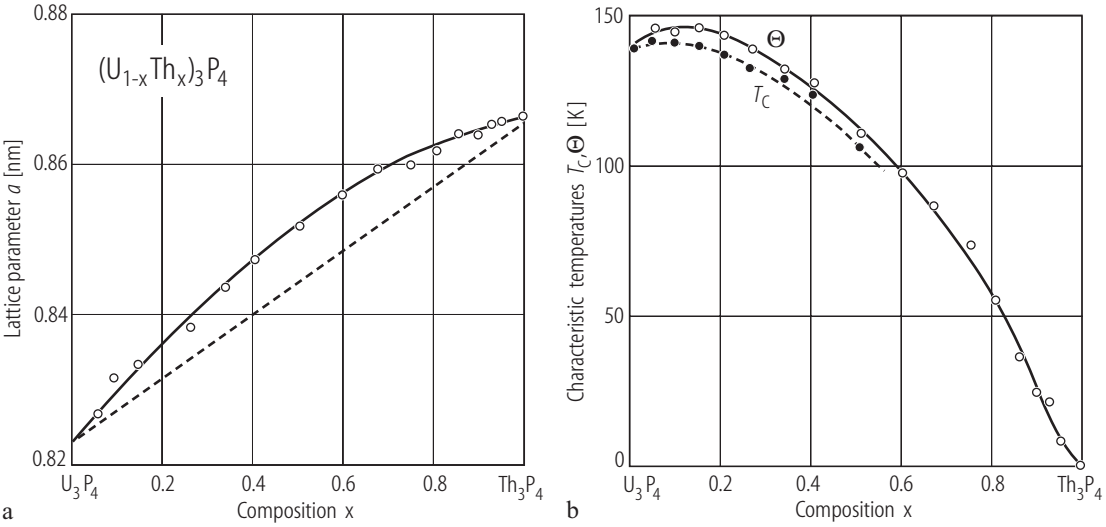

Fig. 115. $(U_{1-x}Th_x)_3P_4$. **(a)** Lattice parameter, a, vs. composition, x [67TPST]. Note the deviation from Vegard's law. **(b)** Paramagnetic, Θ, and Curie, T_C, temperatures vs. composition, x [67TPST]. Both these quantities go through a flat maximum for x ≈ 0.1.

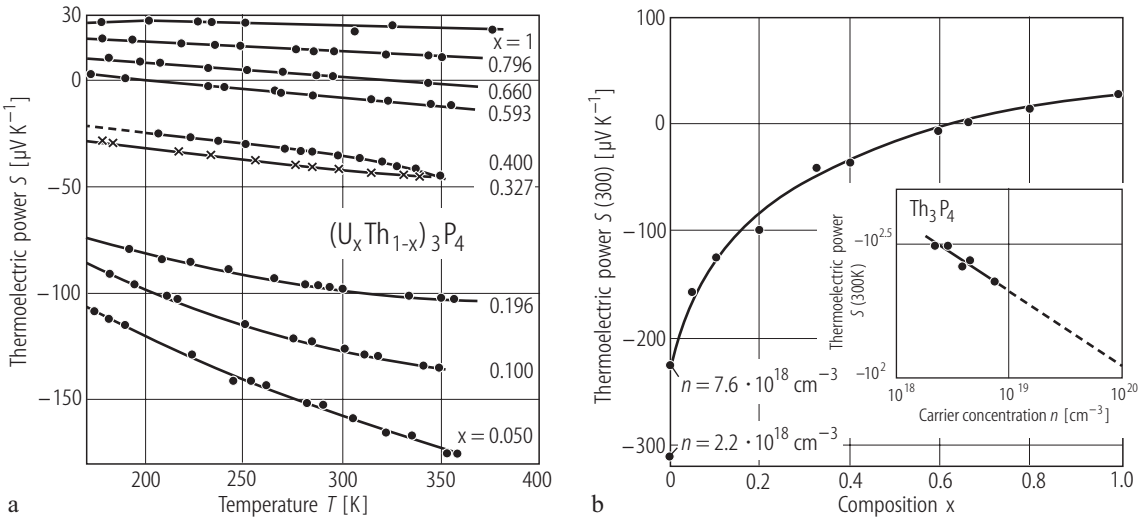

Fig. 116. $(U_xTh_{1-x})_3P_4$. **(a)** Thermoelectric power, S, vs. temperature, T, in the range 170…360 K for several solid solutions with the compositions specified in the figure [72THM]. Note that dS/dT is negative for all the samples and increases with decreasing content of Th_3P_4. **(b)** Thermoelectric power, S(300), measured at T = 300 K, vs. U content, x [72THM]. Note a gradual decrease of S(300) from +26.7 μV/K in U_3P_4 down to –300 μV/K in Th_3P_4 with the change of sign at x = 0.65. Inset: S(300 K) vs. carrier concentration, n, for Th_3P_4 presented in a log-log plot.

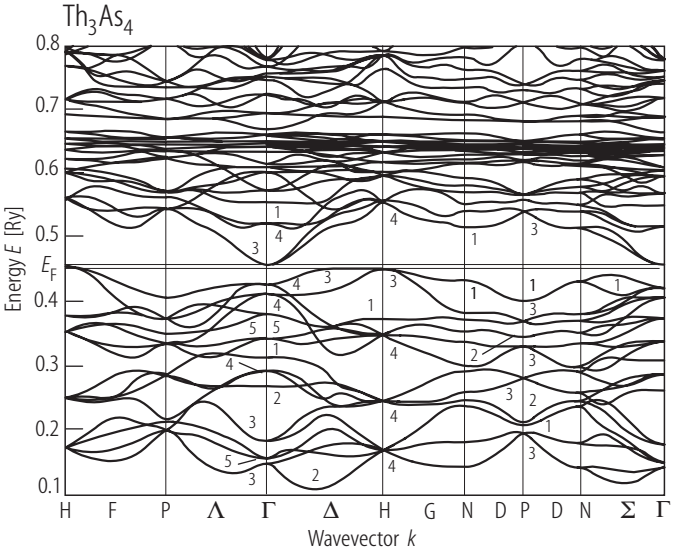

Fig. 117. Th_3As_4. Energy band structure calculated by the self-consistent APW method with LDA [90TKK]. For the details on the method used and comprehensive description of the results refer to the original paper. See also Fig. 118.

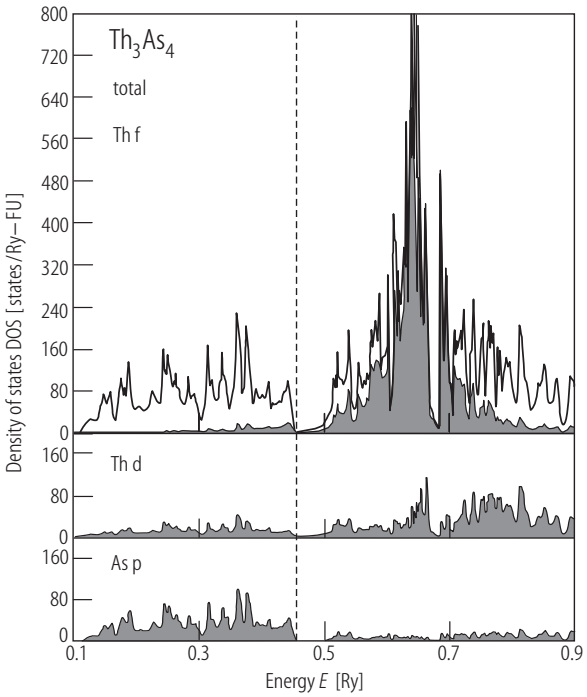

Fig. 118. Th_3As_4. Total and partial density of states calculated by the self-consistent APW method with LDA [90TKK]. The compound is a narrow band semiconductor. The valence band is derived from the As 4p states and the conduction band comes from the Th 6d states. The calculated energy gap of 0.05 eV, however, is much smaller than the experimental value (see Fig. 121), probably because of inadequate treatment of the exchange-correlation potential in LDA. For further details see the original paper.

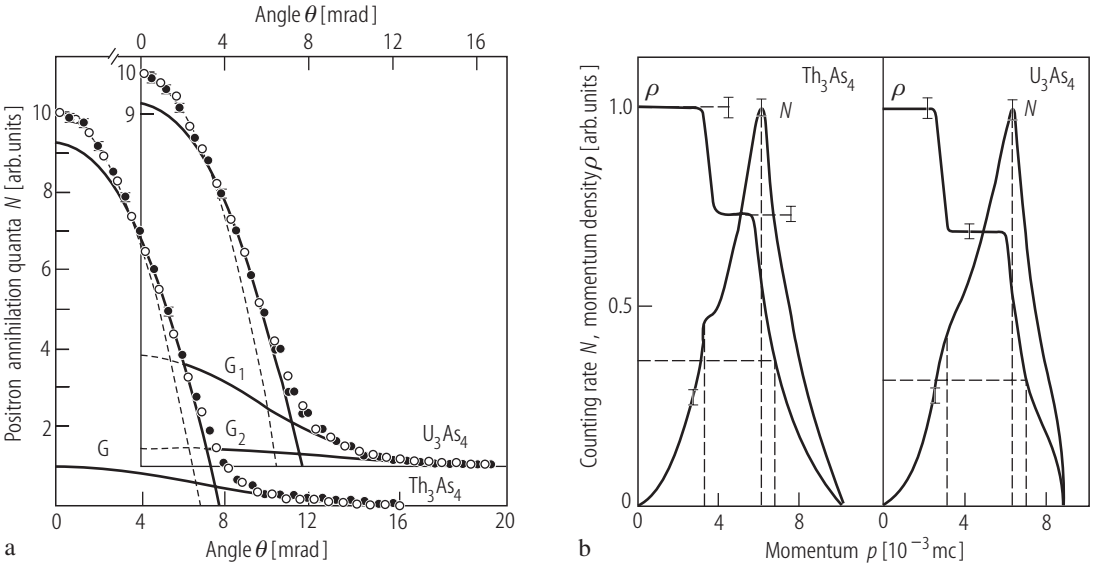

Fig. 119. Th_3As_4, U_3As_4. **(a)** Angular distribution of annihilating positrons, $N(\theta)$ [76RDH]. $\theta = p_z/mc$, where p_z is the zth momentum component of the annihilating electron. Solid and open circles represent the data obtained for positive and negative angles, respectively. The dashed and solid lines are two reversed parabolas used to fit the experimental results at small and medium θ, respectively. The other solid lines labelled G are gaussian curves approximating the high-angle part of $N(\theta)$. In the case of U_3As_4 two different fits are shown (G_1 and G_2), which correspond to two different ranges of θ. Note that the "tail" component, representing annihilation with core electrons, is markedly higher in U_3As_4 compared to Th_3As_4 and this feature suggests a localized character of 5f electrons. **(b)** Distribution of the momentum absolute value, $N(p)$, and the momentum density, $\rho(p)$, obtained from the data shown in panel **(a)** after subtracting a core annihilation part. The number of valence electrons per molecule calculated in the free-electron model approximation equals 31.7(1.4) for Th_3As_4 and 32.7(1.4) for U_3As_4. The electrons are divided into two groups. The first one contains 8.0(4) and 6.4(4) electrons in Th_3As_4 and U_3As_4, respectively. The remaining electrons contribute to the covalent bonding. See [65C] for the discussion of the electrostatic energy and the valence band in isostructural Th_3P_4.

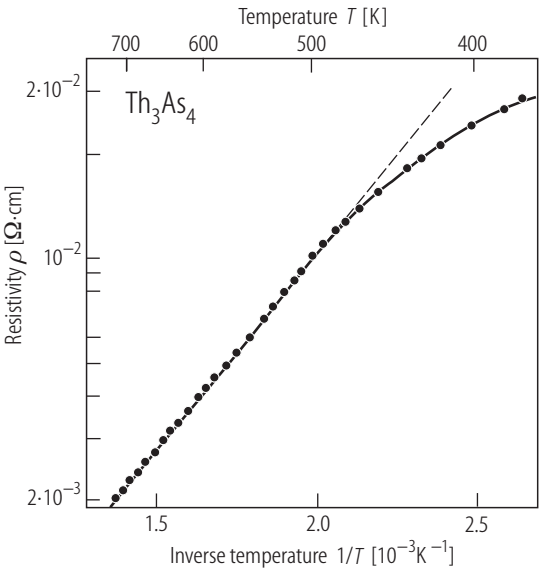

Fig. 120. Th_3As_4. Electrical resistivity, ρ, vs. inverse temperature, $1/T$, in the range 350…700 K for nominally pure sample [79MHW2]. Note a semilogarithmic scale. The dashed line marks an exponential increase of the resistivity with decreasing temperature yielding the forbidden energy gap E_g of 0.44 eV. This value agrees well with that derived by [78HM] (see Fig. 121).

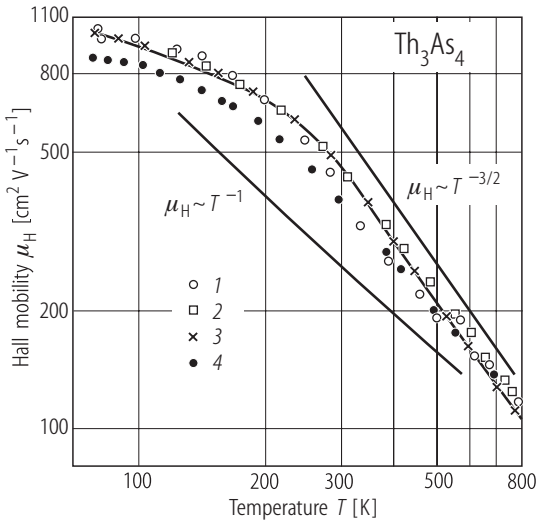

Fig. 122. Th_3As_4. Hall mobility of electrons, μ_H, vs. temperature, T, in the range 78…800 K in a log-log plot [78HM]. Different symbols correspond to four different samples measured. The solid lines mark the behaviour either characteristic of metals above the Debye temperature ($\mu_H \sim T^{-1}$) or characteristic of scattering on phonons ($\mu_H \sim T^{-3/2}$). Note that a $T^{-3/2}$ law is obeyed at high temperatures (above 250 K). A similar behaviour was also found for Th_3P_4 [77HM].

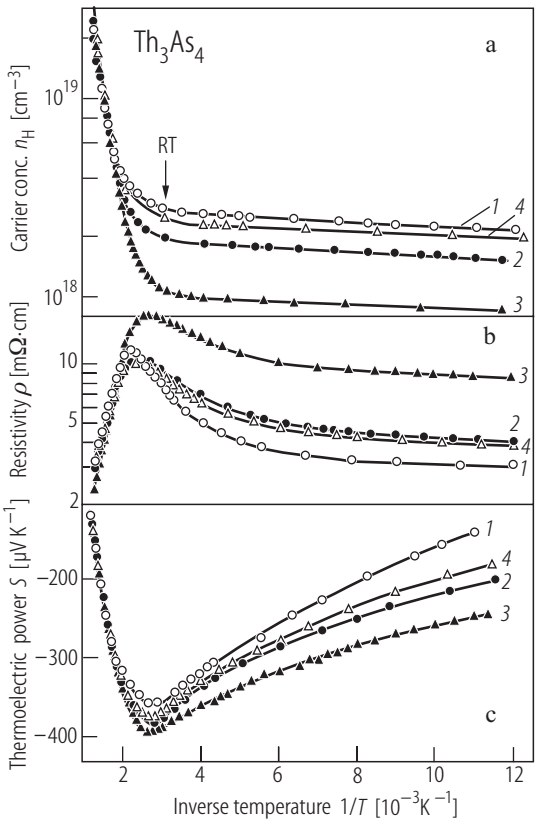

Fig. 121. Th_3As_4. **(a)** Hall carrier concentration, n_H, **(b)** electrical resistivity, ρ, and **(c)** thermoelectric power, S, vs. inverse temperature, $1/T$, in the range 78…830 K [78HM]. Different symbols refer to four different samples measured, which showed different concentrations of free carriers. Note that below room temperature n_H is almost independent of temperature, while ρ and $|S|$ increase with rising temperature as in metals. At higher temperatures n_H strongly increases and ρ and $|S|$ decrease in a manner characteristic of semiconductors in the intrinsic range. Thus Th_3As_4 behaves as a heavily doped semiconductor with impurity states forming a semimetallic band at the bottom or just below the conduction band. From the activation law formulas for the resistivity, Hall constant and thermoelectric power the forbidden energy gap E_g in Th_3As_4 was found by means of extrapolation (see the original paper) to be about 0.43 eV.

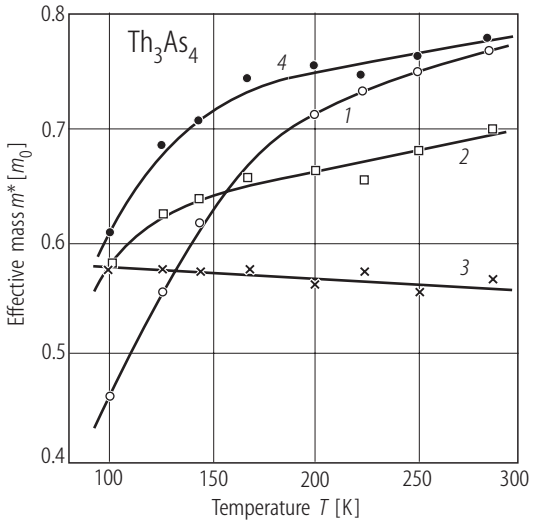

Fig. 123. Th_3As_4. Electron effective mass, m^*/m_0, vs. temperature, T, in the range 100…280 K, calculated on the basis of the Hall constant and thermoelectric power data presented in Fig. 121, assuming a spherical Fermi surface [78HM]. Different symbols refer to four different samples with different electron concentration n_H. Note that in the temperature interval analyzed the carrier concentration for each sample studied is almost constant (see Fig. 121), i.e. the semiconductor is in its extrinsic range. Only for sample 3, exhibiting the lowest electron concentration, m^*/m_0 hardly changes with temperature. For the other samples m^*/m_0 slightly rises with T and this increase is more pronounced for samples having larger carrier concentrations. The effective mass of electrons of the order of 0.55 m_0 is an intermediate value for conduction and impurity bands.

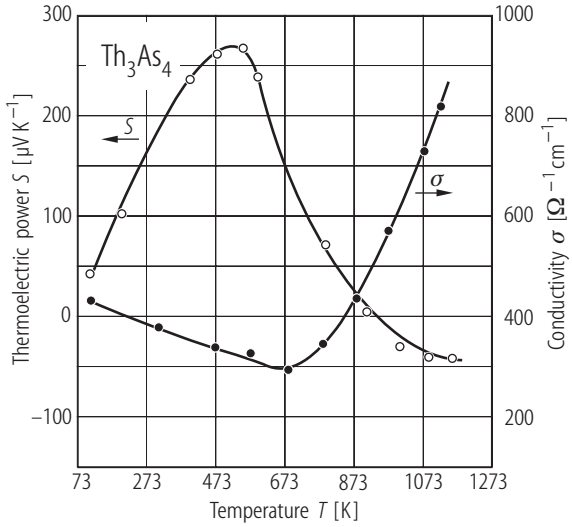

Fig. 124. Th_3As_4. Electrical conductivity, σ, and thermoelectric power, S, vs. temperature, T, in the range 80…1173 K [64WP1]. The compact sample pressed at 1600 °C contained about 10% ThO_2 as an impurity. The p-type conductivity contrasts with the n-type behaviour of nominally pure Th_3As_4 (see Fig. 121) and it is probably caused by some iron impurities.

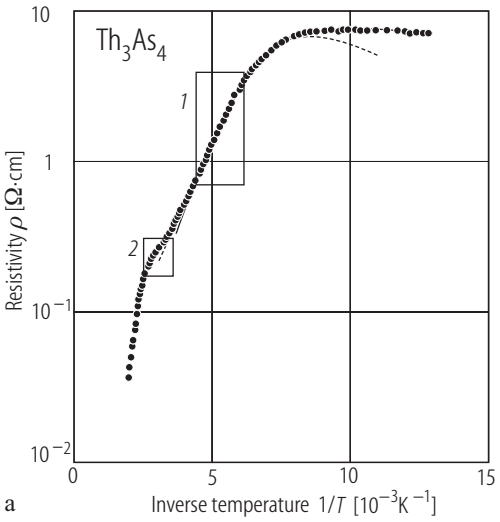

a

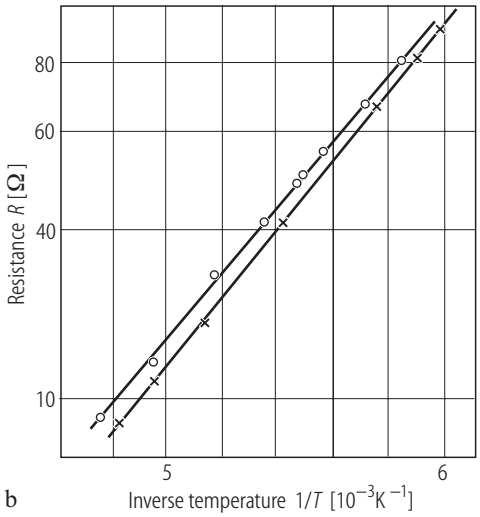

b

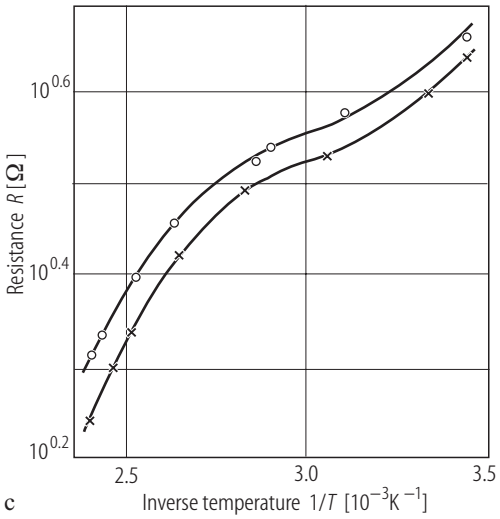

c

Fig. 125. Th_3As_4, sc. **(a)** Electrical resistivity, as log ρ, vs. inverse temperature, $1/T$ [86HMMW]. The solid and dashed lines are fits of the experimental data to the expression $1/\rho = AT^{-\alpha} + BT^{3/2-\alpha}\exp\left(-\frac{E_a}{2k_BT}\right)$ with the assumed values $\alpha = 0.3$ and 1.5, respectively, where the parameter E_a is the activation energy from the valence band into the acceptor impurity band. The fitted values of E_a are 0.156 and 0.170 eV, respectively. The rectangles labeled 1 and 2 mark the temperature regions discussed in panels **(b)** and **(c)**, respecively. **(b)** Electrical resistance, log R, vs. $1/T$ in the range 164…217 K, measured under pressure p = 0.1 MPa (open circles) and 237 MPa (crosses) [86HMMW]. The solid lines mark an excitation behaviour. The fitted E_a is 0.16 eV at normal pressure and it slightly decreases with increasing pressure with a rate of –14 meV/GPa. **(c)** Electrical resistance, log R, vs. $1/T$ in the range 286…425 K, measured under pressure p = 0.1 MPa (open circles) and 237 MPa (crosses) [86HMMW]. Note a tendency towards plateau around 350 K, which is due to exhaustion of unoccupied states in the acceptor impurity band. At these temperatures an increase of pressure gives rise only to a decrease of the absolute resistance. At higher temperatures the resistance is mainly governed by the excitations of electrons from the valence band into the conduction band. The increase of pressure is accompanied by a change in the excitation energy E_g (E_g = 0.39 eV at normal pressure), which decreases with a rate of –17.7 meV/GPa.

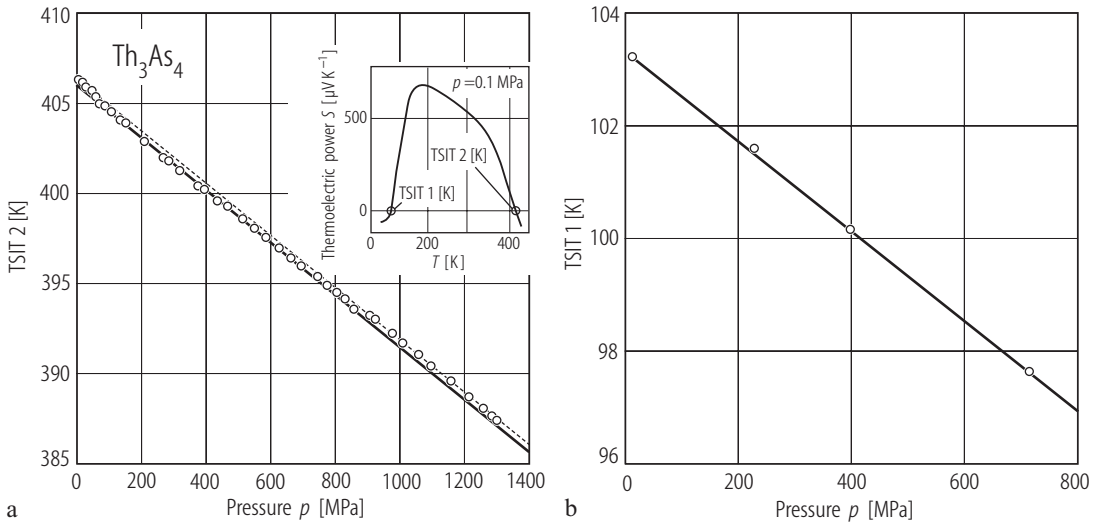

Fig. 126. Th_3As_4, sc. Thermopower sign inversion temperature, TSIT2, vs. pressure, p, up to 1.36 GPa (panel **(a)**) and thermopower sign inversion temperature, TSIT1, vs. pressure, p, up to 0.76 GPa (panel **(b)**) [86HMMW]. For the definition of TSIT1 and TSIT2 see inset in **(a)**, which presents the thermoelectric power, S, vs. temperature, T, measured for a p-type sample at p = 0.1 MPa. The change of sign in $S(T)$ at TSIT1 is a consequence of the compensation between electrons occupying the bottom of the acceptor impurity band and holes occupying the valence band. The reentrant thermopower sign change at TSIT2 is caused by the valence electron excitations to the conduction band. The solid and dashed lines in panel **(a)** mark the experimental error in the determination of TSIT2. The linear decrease with pressure of both TSIT1 and TSIT2 (note the straight lines in panels **(a)** and **(b)**) yields the coefficients $\delta E_a/\delta p$ = –14(1) meV/GPa and $\delta E_g/\delta p$ = –17.7(5) meV/GPa, where E_a and E_g are the excitation energies from the valence band into the acceptor impurity band and the conduction band, respectively.

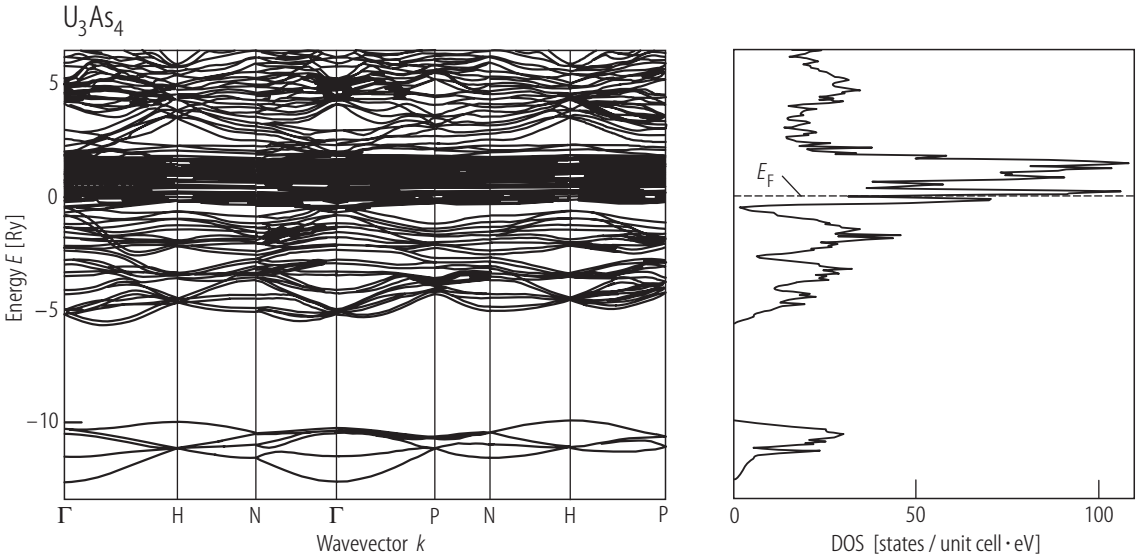

Fig. 127. U_3As_4. Energy band structure and total DOS [in states/(unit cell eV)], calculated by fully relativistic, spin-polarized LMTO method using ASA with combined corrections included [99AHYP]. The LSDA calculations were based on SDFT with von Barth – Hedin parametrization of the exchange potential. For the discussion see Fig. 128.

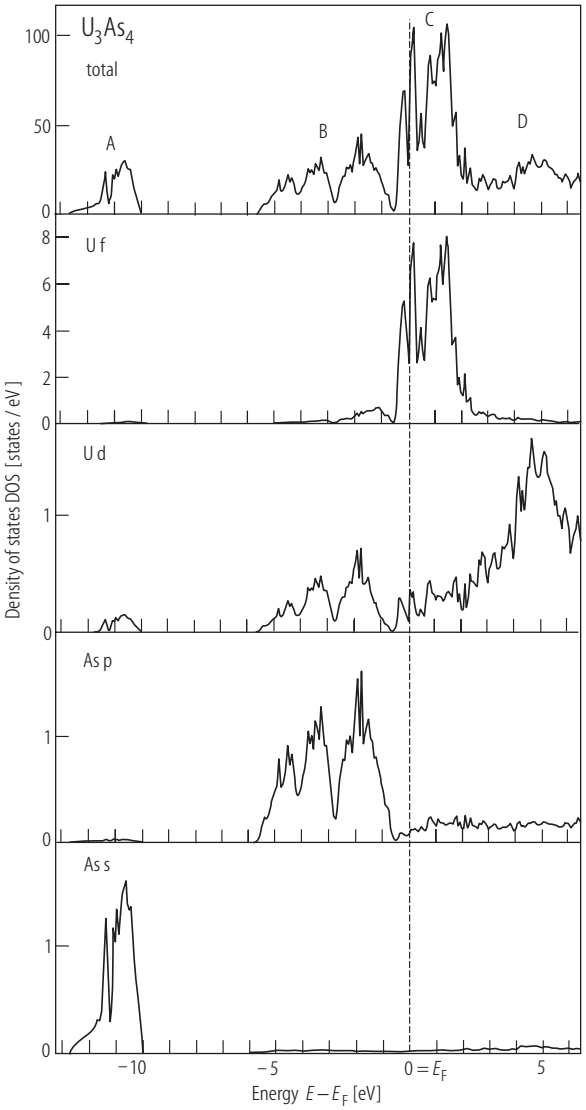

←

Fig. 128. U_3As_4. Fully relativistic, spin-polarized total DOS [in states/(unit cell eV); top panel] and partial DOS [in states/(atom eV)], calculated as in Fig. 127 [99AHYP]. The bands in the lowest energy region A (from –12.7 up to –10 eV relative to E_F = 0) have predominantly As-s character with some admixture of U-spd character. The bands in region B (between –5.7 and –0.5 eV) consist of the P 4p states strongly hybridised with the U 6d states. The uranium 5f bands are located near the Fermi energy in the region C (from –0.5 to 2.0 eV). At still higher energies (region D) there are located antibonding U 6d states.

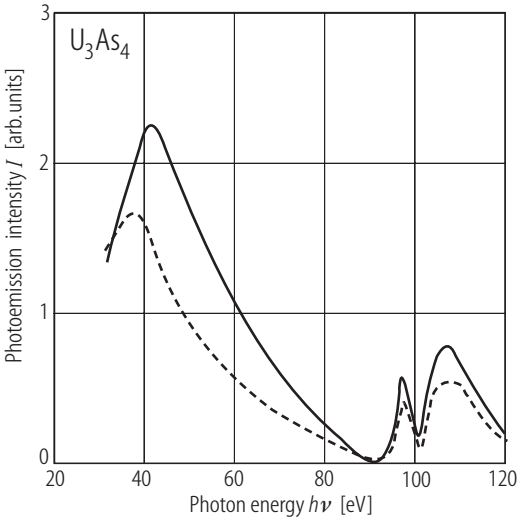

Fig. 129. U_3As_4, sc. Constant initial state (CIS) spectra taken for the binding energy E_b of 0.53 eV (solid line) and 1.89 eV (dashed line) [85SYSM]. The vanishing intensity of the low energy structure with the minimum near $h\nu = 91$ eV indicates that the U5f states prevail in the region of $E_b \approx 0.5$ eV. The CIS maximum around 97.5 eV and the second minimum at 101 eV are related to one body excitation from the $5d_{5/2}$ and $5d_{3/2}$ core levels to the empty 5f states at the Fermi energy.

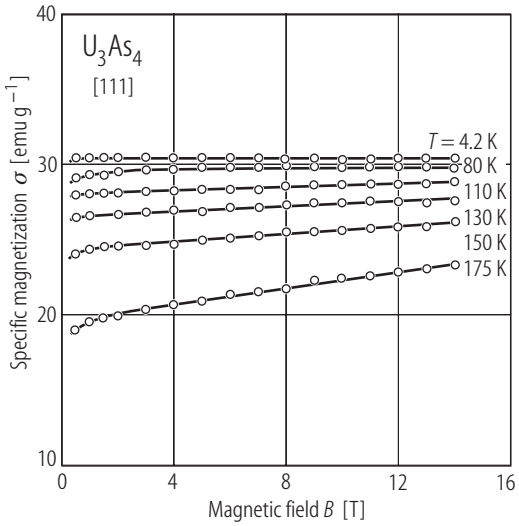

←

Fig. 130. U_3As_4, sc. Specific magnetization, σ, along the [111] axis vs. magnetic field, B, up to 14 T, measured at various temperatures indicated [81TSNM]. The solid lines are guides for the eye. Note that at T = 4.2 K the saturation is easily achieved in rather low magnetic fields and the high-field susceptibility is nearly zero (see Fig. 132 for different result). The saturation magnetic moment p_s equals 1.83 μ_B/U atom being in a good agreement with that found in neutron diffraction studies by [81BRTH] and [99WGH].